Phase Field Simulations of the Coarsening of Complex Microstructures

by

W. Beck Andrews

A dissertation submitted in partial fulfillment
of the requirements for the degree of
Doctor of Philosophy
(Materials Science and Engineering)
in The University of Michigan
2019

Doctoral Committee:

Professor Katsuyo Thornton, Chair
Professor John E. Allison
Professor Selim Esedoglu
Professor Peter W. Voorhees, Northwestern University

W. Beck Andrews

wband@umich.edu

ORCID iD: 0000-0002-8782-4621

To my family.

Acknowledgements

I am thoroughly indebted to all of the people who have made my journey through grad school such a positive experience. First, I would like to thank my advisor, Professor Katsuyo Thornton, for giving me the opportunity to work in her group and for all of her guidance and assistance. I have found this project to be challenging and intellectually engaging, which is what I wanted most out of grad school, and I am grateful to have had an advisor as intelligent and rigorous as she is. I would like to thank Professor Peter Voorhees for his advice and encouragement throughout our collaboration, Professor John Allison for his support as a member of my committee and as the head of the PRISMS Center, and Professor Selim Esedoglu for interesting discussions that helped crystallize my understanding of phase field models. Professor Elizabeth Hildinger has also helped me considerably with writing this last year.

I am grateful to many members of the Thornton group, past and present, for their mentorship, support, and camaraderie. In particular, Chal Park and Larry Aagesen mentored me as I was just starting out in the group, and Susan Gentry provided some useful tools for my work on interfacial energy anisotropy. Alex Chadwick had my back through a particularly challenging series of math and computation courses, and was always the first person in the office I would show an exciting new result. Sam Christie helped me pursue some theoretical leads this last summer. David Montiel provided helpful editing on the paper that is now Chapter 4. Vishwas Goel and especially Golam Mortuza were on hand to do last-minute proofreading of several parts of this dissertation, and they have kept me company over a very stressful couple of months. I have greatly enjoyed working with Stephen DeWitt on apps for PRISMS-PF, and he had some excellent suggestions that improved my oral defense. Thanks as well to Jason, Erik, Min-Ju, Hui-Chia, Raul, Saeed, Doaa, Guanglong, Sicen, Max, Mujan, Martina, Dong-Uk, Roy, Victor, Andrea, and everyone else I have had the

pleasure of working with here.

I have also greatly enjoyed my opportunities for teaching here at the University of Michigan. I must thank Katsuyo again for encouraging my involvement in the Summer School for Integrated Computational Materials Education. I am also very grateful to the lead instructors for my two instructorships, Professor Joanna Millunchick and Dr. Tim Chambers, both for their hard work and for allowing me to experiment with incorporating computational tools into the labs. Of course I must also acknowledge the students themselves, who made all of the work worthwhile.

Finally, my parents have supported essentially my entire education prior to graduate school. They have my love and my gratitude, and their investment has served me well.

This work was supported by U.S. Department of Energy grants DE-FG02-99ER45782 (Coarsening of complex microstructures) and DE-SC0008637 (PRISMS). Computational resources were provided by the Extreme Science and Engineering Discovery Environment (XSEDE), which is supported by National Science Foundation grant number OCI-1053575, under allocation No. TG-DMR110007, as well as the University of Michigan Advanced Research Computing.

Table of Contents

List of Figures

List of Tables

Abstract

Coarsening is a fundamental phenomenon that occurs in a wide range of engineering materials, from polymer blends to cast aluminum alloys to functional nanostructured materials. The physics of coarsening is well understood. Differences in interfacial curvatures provide a driving force for mass transport, and the resulting evolution reduces the overall interfacial energy of the system as the average length scale of microstructural features increases. For simple particulate systems, such as those consisting of spherical precipitates at low volume fractions, analytical descriptions for the evolution are available and provide powerful tools for engineers to predict the microstructure for a given material and processing conditions. However, it is more difficult to predict the evolution of complex, well-connected structures like those present in dendritic solid-liquid systems and nanoporous metals. In these cases, simulations are necessary in order to develop fundamental understanding of coarsening and to gain the ability to predict microstructures that undergo coarsening. This dissertation consists of a series of simulation studies of coarsening of microstructures with complex morphologies. The simulation results and theories obtained here represent a fundamental contribution to the understanding of coarsening in complex microstructures.

Coarsening with phases that have dissimilar mobilities is a condition typical of experimental solid-liquid systems. In a two-dimensional simulation, coarsening with dissimilar mobilities resulted in a morphological transition, as the initially complex, labyrinthine microstructure transforms into a system of high-mobility particles in a low-mobility matrix. In contrast, coarsening in three dimensions with dissimilar mobilities resulted in a stable bicontinuous structure after an initial transient stage. In this transient stage, we observed a theoretically predicted relationship between the coarsening rate constant and the variance of scaled mean curvature.

Another important class of coarsening systems is those evolving by surface diffusion, includ-

ing nanoporous metals. Intermediate volume fractions (between 36% and 50% minority phase) resulted in bicontinuous structures that coarsened self-similarly; that is, their morphologies became time-invariant when scaled by an evolving length scale. Morphologies of structures coarsening via surface diffusion were quantitatively different from those coarsening via bulk diffusion, but the difference was smaller than that of volume fraction. Simulations at a lower volume fraction, 32%, found coexistence of independent particles with well-connected domains.

The effect of regularization in a phase field model with strongly anisotropic interfacial energy was quantified to understand and mitigate the error. An asymptotic analysis was performed to derive the expression for the effective interfacial energy for a given input interfacial energy. Simulated equilibrium shapes confirmed the prediction. The result can be used to parameterize the input anisotropic interfacial energy to implement desired interfacial anisotropy.

To examine the origin of the ubiquity of the coarsening power law (the length scale proportional to the cubed root of time) two-dimensional simulations were conducted with a bimodal particle distribution. Particles with small radii were found to dominate the overall evolution within these simulations. The small particles evolved self-similarly, leading to agreement with the theoretical $t^{1/3}$ power law despite a lack of self-similarity in the overall structure. This set of simulations verified the existence of inactive length scales in coarsening, which was hypothesized in experiments. Additionally, a model was developed to study the role of topological singularities (pinching-off of necks) in bicontinuous structures during coarsening. Preventing topological singularities was found to reduce the coarsening rate, but further analysis of the data is required to fully understand the role of topological singularities.

Chapter 1

Introduction

1.1 Motivation

Interfaces between phases in a physical system disrupt the inter-atomic or inter-molecular interactions that stabilize the phases, increasing the free energy of the system. This interfacial energy provides a thermodynamic driving force for evolution: the system can reduce its total free energy by reducing the total area of interface. The process by which a two-phase system evolves to reduce its total interfacial area is known as coarsening or Ostwald ripening [1].

Coarsening, in a broad sense, is ubiquitous in both our natural environment and in engineered materials. One can observe it, for example, in the foam bubbles that compose the head of a freshly poured pint of beer, or in the water particles that precipitate on one's glasses upon entering a warm, humid building from the cold. In both of these cases, small particles, because of their relatively high surface area in proportion to their volume, disappear from the system, and their material is absorbed into larger particles that increase in size. Figure 1.1 [2] illustrates this process in a solid-liquid system composed of Sn-rich particles in a Pb-rich liquid. As the system evolves in time, the Sn-rich particles (light phase) increase in size and decrease in number, resulting in a decrease of the interfacial area of the system.

Coarsening plays a fundamental role in materials science because it affects the microstructure of materials (the shapes and distributions of phases at small length scales), which in turn affects the properties of materials [3]. Materials properties determine their performance in applications.

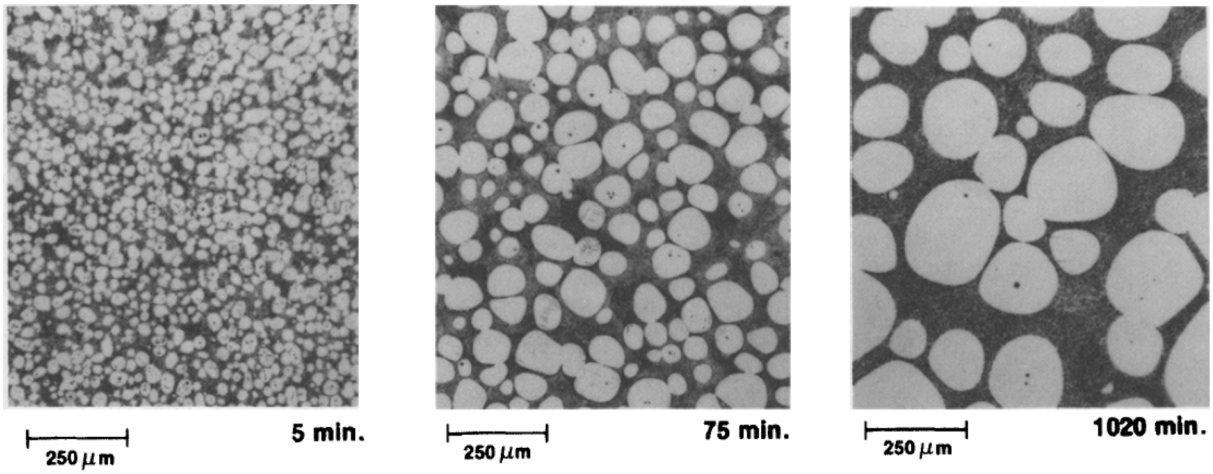

Figure 1.1: Optical micrographs of Pb-Sn alloy microstructure following coarsening at 185 °C, just above the eutectic temperature, for the indicated time. The light phase is primary Sn-rich particles and the dark phase is eutectic Pb-Sn. Adapted from Ref. [2] (not subject to copyright).

For example, nickel-base superalloys are commonly used in applications that require high strength at high temperatures, such as turbine disks in the hot section of jet engines [4]. Their resistance to deformation at high temperatures (creep) is affected by the size and distribution of micro- or nano-scale $Ni_3(Al, Ti)$ (γ'-phase) particles [5]. An example Ni-base alloy microstructure is illustrated in Fig. 1.2 [5]. Small γ'-phase particles initially precipitate into the Ni matrix, then grow until the particle and matrix phases are near equilibrium, and finally they coarsen [6]. Small particles disappear and large particles grow via diffusion through the Ni matrix.

Cast aluminum alloys provide another example. They are widely used for structural components in the aerospace and automotive industries [7], where strength and toughness are required. The mechanical properties of these alloys depend in part on the spacing between arms of the dendritic structure that results from solidification [8, 9]. As shown in Fig. 1.3 [10], coarsening increases this arm spacing, as smaller features (tertiary dendrite arms) are eliminated and the larger features (primary and secondary dendrite arms) increase in size.

The driving force for coarsening is greater when the length scale of the system is smaller, and therefore coarsening is a particularly important process at the nano-scale [11]. Nanoporous metallic structures [11, 12, 13, 14] have been the subject of recent interest for functional applications [15, 16, 17, 18], and as materials with tunable mechanical properties [19, 20]. These applications

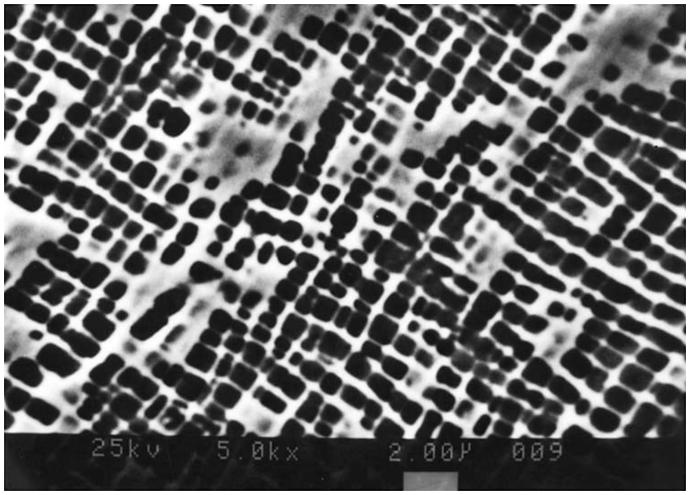

Figure 1.2: SEM micrograph of rounded cuboidal type γ' particles in a nickel-base superalloy (IN-100, as-cast). Reprinted from Ref. [5] with permission.

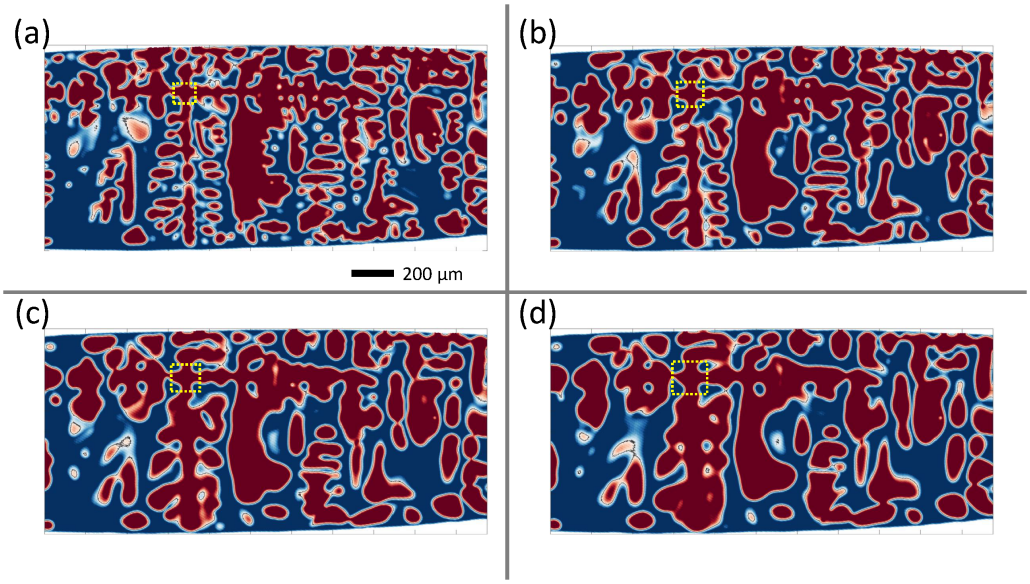

Figure 1.3: Cross-sections of dendritic microstructure during coarsening, showing Al-rich dendrites (red phase) in Cu-rich liquid (blue phase) at four different times: (a) 8.40 min, (b) 25.12 min, (c) 47.62 min, and (d) 78.15 min. Sample was prepared by directional solidification of Al-19wt%Cu and was coarsened at a temperature of 558 °C. Reprinted from Ref. [10].

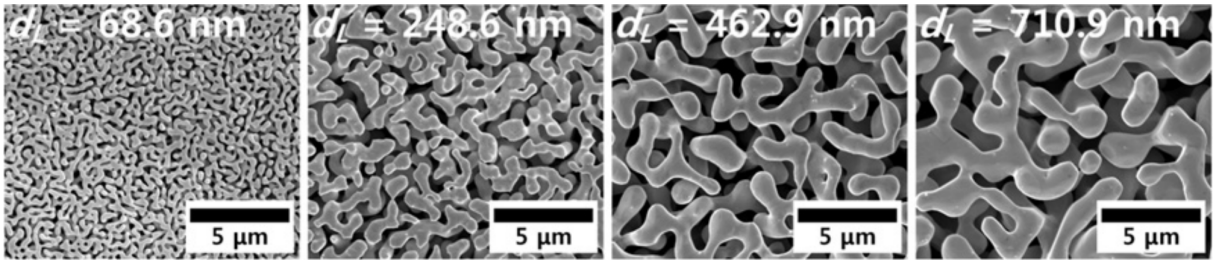

Figure 1.4: SEM images of nanoporous gold. Samples were prepared by dealloying 28at.% Au-72 at.% Ag alloy in 35% nitric acid solution at 80 °C for 72h and coarsening at (from left to right) 300 °C, 400 °C, 500 °C, and 600 °C for 2 h. Adapted from Ref. [19] with permission.

rely on high surface area and small feature sizes, both of which are affected by coarsening. Figure 1.4 shows the evolution of nanoporous gold during coarsening [21]. The mechanism for mass transport in these structures is thought to be diffusion of atoms along the surface (i.e., surface diffusion) [16, 22], as opposed to diffusion through the liquid phase or Ni matrix phase in the previous examples (i.e., bulk diffusion).

Given the fundamental role of coarsening in materials science, it is unsurprising that it has garnered considerable theoretical interest [23, 24, 25, 26, 27, 28, 29, 30, 31, 32]. The seminal theory of coarsening is that of Lifshitz and Slyozov [23] and Wagner [24] (hereafter LSW), which is valid in the limit of low volume fraction of the precipitate phase. This theory predicts how a microstructure that consists of spherical particles evolves in time, specifically how particles grow or shrink based on their size relative to a critical radius. As part of the theory, LSW derived a particle size distribution that was time-invariant when scaled by the critical radius, which evolves in time. This time-invariance after scaling is known as self-similarity [33]. The kinetics of evolution of the critical radius were determined analytically, and it was found to follow a $t^{1/3}$ power law during self-similar evolution. Finally, LSW also predicted that initial particle size distributions different from the self-similar distribution would converge toward it over time.

LSW theory has inspired a considerable body of literature, including direct experimental comparisons [34, 35] and theoretical extensions to higher volume fractions [25, 26, 27, 30]. Elements of LSW theory have also been combined with theories of nucleation and growth to develop more complete descriptions of precipitation kinetics, notably the analytical model of Langer and

Schwartz [6] and the numerical model of Kampmann and Wagner [36]. These models form the basis of commercial tools for predicting precipitation in multicomponent alloys, such as the TC-PRISMA© module developed by Thermo-Calc Software AB [37, 38]. As materials science and engineering continues to move toward a framework of ICME- integrated computational materials engineering [39], fundamental models like LSW theory are becoming essential components of the more complex tools that are being developed for engineering applications.

The present work addresses a limitation common to LSW theory and the related theories discussed in Refs. [28, 29, 31, 32]: they assume that the microstructure consists of particles embedded in a matrix. While this type of morphology is very widely observed, there are also systems with more complex microstructures, where both phases are well-connected or even bicontinuous. In a bicontinuous structure, both phases are fully connected; a path can be found to connect any two points within the same phase without crossing the interface. Dendritic microstructures (e.g., Fig. 1.3) are one family of complex microstructures that are of particular technological importance because of their presence during metal casting [10, 40, 41, 42, 43, 44, 45, 46]. Bicontinuous microstructures include polymer blends [47, 48, 49] and nanoporous metallic structures (e.g., Fig. 1.4), which, as noted before, are being investigated for functional [15, 16, 17, 18] and structural [19, 20] applications. Clearly, coarsening of complex microstructures is of considerable interest to the broader materials science community.

The overall objective of this dissertation is to build a foundation for a theory of the coarsening of complex microstructures, which would enable predictions of microstructural evolution just as coarsening theories do for particle-matrix systems. Such a theory could be employed in computational tools, for example, to predict microstructures resulting from thermal treatment of cast components. A foundation is necessary because of the difficulty of modeling coarsening in complex microstructures. Certain facts about the coarsening dynamics are known, such as the evolution of local curvature [42, 50, 51] and the evolution of global microstructure quantities (area and volume) [52], but additional facts or assumptions are necessary to make analytical predictions.

To gain more insight into the dynamics, we perform phase field simulations of the coarsening

of complex microstructures, similarly to Refs. [53, 54, 55]. We extend the previous work by incorporating conditions that are expected in experimental systems: mobilities that are dissimilar between the phases (expected in solid-liquid systems [44, 45]) and surface diffusion (expected in nanoporous metallic structures [13, 16]). We also begin to examine anisotropic interfacial energy, which is present when one phase or both phases are crystalline. Results from these simulations provide a basis for comparison to experiments.

Furthermore, by manipulating the conditions of our simulations, we can test hypotheses in ways that are difficult (if not impossible) to do experimentally. We can isolate parameters, such as the transport coefficients (i.e., the mobilities) of the phases, while keeping all of the other conditions, such as the initial morphology and interfacial energy, constant. We can isolate morphology itself by specifying the initial geometry, and examine geometric factors in coarsening. We can even manipulate the coarsening dynamics directly, by kinetically inhibiting processes such as topological singularities. The differences and similarities between conditions will help future authors develop and test hypotheses about the dynamics. This dissertation itself contains supporting evidence for two such hypotheses (the first is introduced in Section 2.3.2 and applied in Sections 4.5.4 and 8.1 and the second is described in Chapter 7), which represent contributions to our understanding of the coarsening of complex microstructures.

1.2 Dissertation outline

This dissertation consists of a series of simulation studies using the phase field approach to probe the effects of different conditions on the coarsening process. Chapters 1-3 contain general introductory information and methods, while our principal results are contained in Chapters 4-8.

Chapter 2 contains background regarding the theory of coarsening as it is applied in this work, starting with geometric definitions. The thermodynamic assumptions of the theory are explained, and the equations governing coarsening dynamics are presented from a classical (i.e., sharp interface) perspective. Two theoretical methods for understanding coarsening are introduced: the

power laws for self-similar evolution and the geometrically general theory of DeHoff [52].

Chapter 3 introduces the simulation methods in general terms, since each Chapter has distinct variants of the model or initial conditions. The phase field model and numerical methods are presented. A rescaling procedure is provided that enabled us to compare our results to literature results with different parameters. Finally, the methods used to characterize and quantify the simulated structures are given.

In Chapter 4, coarsening of a two-phase system in which the phases had dissimilar mobilities is studied at $50/50$ (50%) volume fraction. The model for dissimilar mobilities is introduced, and results in two dimensions (2D) and three dimensions (3D) are presented and discussed. In 2D, a morphological transition during coarsening is identified when the mobility is dissimilar that is not observed when the mobility is constant. The 3-D simulations with dissimilar mobilities resulted in bicontinuous morphologies that evolved self-similarly. The transient coarsening kinetics in the three-dimensional simulations are observed to match a theoretical prediction by DeHoff [52] that related the variance in scaled curvature to the instantaneous coarsening rate constant. Based on theory and simulations, The primary difference in the kinetics of coarsening between the dissimilar-mobility and constant mobility is identified.

In Chapter 5, 3-D simulations of coarsening via surface diffusion are presented. Self-similar coarsening via surface diffusion is observed at 50% and $36/64$ (36%) volume fractions. These self-similarly evolving structures had bicontinuous morphologies, similar to those observed during coarsening via bulk diffusion. Quantitative differences were found between these surface- and bulk-diffusion cases, but overall the difference between morphologies due to coarsening mechanism is smaller than the effect of volume fraction. Coarsening via surface and bulk diffusion is also examined at 32% volume fraction, which resulted in structures with both a single well-connected domain (typical of bicontinuous structures) and a number of independent particles. Sensitivity of the structures to volume fraction is confirmed by examining coarsening via bulk diffusion at 30% volume fraction, in which the initial structure is observed to break up rapidly into particles. Finally, the surface-diffusion model is compared to an alternative model that had been used in

previous literature.

Chapter 6 examines a phase field model for evolution with regularized strongly anisotropic interfacial energy. The interfacial energy is found to be affected by the regularization, and a Cahn-Hoffman ξ-vector is derived for the modified interfacial energy. This model is found to converge to the correct coarsening dynamics for the modified interfacial energy by an asymptotic analysis. Excellent agreement is obtained for the particle shapes away from the regularized corners, confirming the analysis, and the simulated corner shapes were found to agree with sharp interface predictions for the Willmore regularization (i.e., mean curvature squared).

In Chapter 7, the existence of inactive length scales in coarsening is demonstrated in a two-dimensional simulation. Particles with small radii were found to dominate the overall evolution of a system with a bimodal particle size distribution. The small particles evolved self-similarly, leading to agreement with the theoretical $t^{1/3}$ power law despite a lack of self-similarity in the overall structure.

Chapter 8 contains two sections of preliminary work. Additional simulation results with constant mobility are provided that support the relationship between the variance in scaled curvature and the instantaneous coarsening rate constant that was derived in Chapter 4. The relationship is confirmed for different volume fractions and initial morphologies. A model is provided for kinetically inhibiting topological singularities in bicontinuous microstructures. Preliminary results with this model indicate that topological singularities are important kinetically, but further analysis of the data is required to fully understand their role in the coarsening process.

Chapter 9 contains conclusions, applications for the presented work, and suggested directions for future work.

Chapter 2

Theoretical background

A rigorous theoretical foundation is necessary to ground our inquiry into coarsening. In this chapter, we present the fundamental physical relationships governing the dynamics of coarsening, and introduce methods to model coarsening analytically based on these relationships. We begin with definitions of the relevant geometric quantities, including curvature, interfacial velocity, and the surface gradient and Laplacian. Then, starting from a standard description of the bulk thermodynamics of materials, we define the thermodynamic framework for our presentation of the dynamics. These provide the necessary background to introduce the Gibbs-Thomson effect, which relates interfacial geometry to chemical potential. Gradients in chemical potential provide the driving force for mass transport, for which two mechanisms are introduced, bulk and surface diffusion. Finally, two theoretical methods for modeling coarsening are introduced: the power law for dynamic scaling and the geometrically general theory of DeHoff [52].

2.1 Surface kinematics

Here, we important concepts regarding the geometry of the interface, such as curvature, interfacial velocity, and the surface gradient and Laplacian. This section is split into two subsections corresponding to different ways of defining coordinates on the interface. First, we consider the classical approach from differential geometry, in which the interface is parametrized by surface coordinates. This is convenient when such a parametrization is available (i.e., for test problems), and when the interface is evolving in time. The second approach does not explicitly parametrize the interface, in-

stead defining quantities in terms of three-dimensional (3-D) Cartesian coordinates. This approach contains definitions and identities that are used in Chapter 6.

2.1.1 Differential geometry

Here, we define the geometric concepts used in subsequent Chapters in terms standard to differential geometry. The information about curvature is primarily drawn from Kreyszig [56], while relations for interfacial evolution are drawn from Refs. [50, 57]. We consider the interface as a surface, S, embedded in a volume, Ω, of a 3-D Euclidean space with Cartesian coordinates. The surface is described mathematically by a function, $\vec{f}(u_1,u_2)$, that maps surface coordinates (u_1,u_2) to the 3-D Cartesian coordinates (x_1,x_2,x_3) of points on the surface. The Monge parametrization is a useful example,

$$\vec{f} = [u_1, u_2, z(u_1,u_2)], \tag{2.1}$$

where the function $z(u_1,u_2)$ gives the 'height' of the surface above the $x_3 = 0$ plane. The partial derivatives of $\vec{f}$ with respect to the surface coordinates u_1 and u_2 are vectors tangent to the surface. Taking the cross product of $\partial\vec{f}/\partial u_1$ and $\partial\vec{f}/\partial u_2$ and normalizing, we obtain the unit normal vector $\vec{n}$,

$$\vec{n} = \pm\frac{\frac{\partial\vec{f}}{\partial u_1}\times\frac{\partial\vec{f}}{\partial u_2}}{\left|\frac{\partial\vec{f}}{\partial u_1}\times\frac{\partial\vec{f}}{\partial u_2}\right|}, \tag{2.2}$$

where the choice of sign represents the orientation of the surface. The surface divides the domain Ω into two subdomains, Ω^+ and Ω^-, which contain the two phases β and α, respectively. To specify the orientation of interfaces in this Chapter, we define that the normal vector points from Ω^- to Ω^+, i.e., from β phase to α phase.

The tangent vectors $\partial\vec{f}/\partial u_1$ and $\partial\vec{f}/\partial u_2$ are also used to obtain the metric tensor of $\vec{f}$, defined as

$$g_{ij} = \frac{\partial\vec{f}}{\partial u_i}\cdot\frac{\partial\vec{f}}{\partial u_j}, \tag{2.3}$$

This tensor is used to relate distances and areas in the surface coordinates to distances and areas on

the surface. For example, g_{ij} is used to express the element of area dA at some point on S in terms of the surface coordinates,

$$dA = \sqrt{\det(g_{ij})} du_1 du_2. \tag{2.4}$$

The quantity $\sqrt{\det(g_{ij})}$ is the area of the parallelogram formed by $\partial \vec{f}/\partial u_1$ and $\partial \vec{f}/\partial u_2$, and it is also the denominator in Eq. 2.2 The contravariant metric tensor g^{ij} is defined as the inverse of g_{ij},

$$g^{ij} = \frac{1}{\sqrt{\det(g_{ij})}} \begin{pmatrix} g_{22} & -g_{12} \\ -g_{12} & g_{11} \end{pmatrix}. \tag{2.5}$$

Now we consider how to calculate curvature. The second fundamental form of $\vec{f}$ can be written as

$$h_{ij} = -\frac{\partial \vec{f}}{\partial u_i} \cdot \frac{\partial \vec{n}}{\partial u_j}. \tag{2.6}$$

The sign of this equation determines the sign of curvature relative to the orientation of the interface (the direction in which the normal is pointing). With the normal vector pointing from β phase to α phase, as defined previously, spherical particles of β phase have positive curvature. Multiplying h_{ij} by the contravariant metric tensor g^{ij} results in the shape operator [58], $h_i^{\ j}$,

$$h_i^{\ j} = \sum_k^2 g^{kj} h_{ik}. \tag{2.7}$$

The principal curvatures κ_1 and κ_2 are the eigenvalues of $h_i^{\ j}$, where in this work $\kappa_2 \geq \kappa_1$ by convention. The mean curvature H and Gaussian curvature K are related to the trace and determinant of $h_i^{\ j}$, respectively:

$$H = \frac{1}{2} \mathrm{tr}\left(h_i^{\ j}\right) = \frac{1}{2}\left(\kappa_1 + \kappa_2\right), \tag{2.8}$$

$$K = \det\left(h_i^{\ j}\right) = \kappa_1 \kappa_2. \tag{2.9}$$

Curvature represents the rate of change of the normal vector along the surface. This can be easily visualized when the interface is a curve in two dimensions (2D), which can be described as a 3-D

surface with cylindrical symmetry. This parametrization can be expressed as $\vec{f} = [x(u_1), y(u_1), u_2]$, and the element of arc ds of the curve is given by

$$ds = \sqrt{\left(\frac{dx}{du_1}\right)^2 + \left(\frac{dy}{du_1}\right)^2} du_1. \tag{2.10}$$

Defining the orientation angle θ as the angle between the normal vector to the surface and a fixed reference vector in the $x_1 - x_2$ plane, the scalar curvature κ of the 2-D curve is simply [59]

$$\kappa = \frac{\partial \theta}{\partial s}. \tag{2.11}$$

Scalar curvature κ is related to the 3-D curvatures by $H = \kappa/2$, $K = 0$, and $\kappa_2 = \kappa$ and $\kappa_1 = 0$ when $\kappa > 0$ ($\kappa_1 = \kappa$ and $\kappa_2 = 0$ otherwise).

Parametric definitions of surfaces are useful for describing evolving interfaces. Evolution can be defined such that while the interface S changes, the domain of surface coordinates U stays constant, and therefore the surface coordinates $(u_1, u_2) \in U$ are unchanging. Accordingly, we define the normal motion of the interface by

$$\frac{\partial \vec{f}}{\partial t} = v_n \vec{n}, \tag{2.12}$$

where v_n is the normal velocity. With the evolution of the surface defined in this way, evolution equations for the quantities defined in Eqs. 2.3-2.9 can be obtained via application of the rules of partial differentiation. For example, the element of area defined in Eq. 2.4 evolves according to

$$\frac{\partial}{\partial t} dA = -2 v_n H dA. \tag{2.13}$$

See Ref. [57] (Lemma 3.2 and Corollary 3.6) for proof in the case $v_n = -2H$. The evolution of

mean curvature itself is given by

$$\frac{\partial H}{\partial t} = v_n \left(2H^2 - K\right) + \frac{1}{2}\nabla_S^2 v_n, \tag{2.14}$$

where $\nabla_S^2 v_n$ denotes the surface Laplacian of v_n,

$$\nabla_S^2 v_n = \sum_i^2 \sum_j^2 \frac{1}{\sqrt{\det(g)}} \frac{\partial}{\partial u_j} \left(g^{ij} \sqrt{\det(g)} \frac{\partial v_n}{\partial u_i} \right). \tag{2.15}$$

Eq. 2.14 is derived in Ref. [50] for general interfacial velocities, and in Ref. [57] (Corollary 3.5) for the case $v_n = -2H$.

2.1.2 Surface derivatives in Cartesian coordinates

Surface derivatives can also be expressed in 3-D Cartesian coordinates without explicit reference to the surface coordinates. This will be convenient for the derivations in Chapter 6. Following Ref. [60], the projection tensor P_{ij} is defined using the normal vector $\vec{n}$,

$$P_{ij} = \delta_{ij} - n_i n_j, \tag{2.16}$$

where δ_{ij} is the Kronecker delta ($\delta_{ij} = 0$ if $i \neq j$, $\delta_{ij} = 1$ if $i = j$). Multiplication of a three-dimensional vector $\vec{w}$ by the projection tensor, i.e., $P\vec{w} = \sum_j P_{ij} w_j$, projects $\vec{w}$ into the tangent plane of the surface. Similarly, $\vec{w}$ is tangent to the surface if it satisfies $P\vec{w} = \vec{w}$. Ref. [60] defines the surface gradient of a scalar ψ as

$$\nabla_S \psi = P \nabla \psi, \tag{2.17}$$

where $\nabla\psi$ is the 3-D gradient of ψ (or, strictly speaking of the extension of ψ to 3D in the vicinity of the interface). Similarly, the surface gradient of a vector $\vec{w}$ is defined as

$$\nabla_S \vec{w} = P \nabla \vec{w}. \tag{2.18}$$

and its surface divergence as

$$\nabla_S \cdot \vec{w} = \mathrm{tr}(P\nabla\vec{w}). \tag{2.19}$$

The surface Laplacian of ψ is then

$$\nabla_S^2\psi = P\nabla\cdot(P\nabla\psi)\,. \tag{2.20}$$

With these definitions, the shape tensor can be expressed as

$$h_i^{\ j} = -\nabla_S\vec{n}. \tag{2.21}$$

Considering this form of $h_i^{\ j}$ as a 3×3 matrix, it has at most rank $= 2$, since that is the rank of the projection tensor P_{ij}. This form of $h_i^{\ j}$ therefore contains the same information as the tensor defined in Eq. 2.7; it has eigenvalues κ_1, κ_2, and zero, and the mean curvature can be expressed succinctly as

$$H = -\frac{1}{2}\nabla_S\cdot\vec{n}. \tag{2.22}$$

2.2 Coarsening dynamics

Here, we present the dynamics of coarsening from a theoretical perspective. This dynamics provides the starting point for the theoretical methods described in the next section, and the results in Chapters 4, 5, 7, and 8 consist of simulations of this dynamics using the phase field method. First, we describe the bulk thermodynamics, defining the bulk free energy density and chemical potential. Then we introduce the Gibbs-Thomson effect, which relates interfacial geometry to chemical potential. Gradients in chemical potential provide the driving force for mass transport, and two transport mechanisms are introduced, bulk and surface diffusion. The transport mechanism determines the evolution of the interface, completing the description of the coarsening dynamics.

2.2.1 Bulk thermodynamics

We begin by considering a bulk system, i.e., neglecting the effect of the interface. This will motivate an important assumption, constant molar volumes of both phases, and allow us to define important quantities, such as the chemical potential and bulk free energy density. We consider a closed system with two components, A and B, at constant temperature and constant pressure. The Gibbs free energy of a single phase is a function of temperature, pressure, and the number of moles of each component, N^A and N^B [61], $G(T,P,N^A,N^B)$. We can define the molar Gibbs free energy G^m by [31, 62],

$$G(N_A,N_B) = NG^m(X), \tag{2.23}$$

where $N = N^A + N^B$ denotes the total number of moles of α and X is the mole fraction of A, $X = N^A/N$.

If two phases, α and β, are present, then the average mole fraction of the system is $\bar{X} = (N_\alpha/N)X_\alpha + (N_\beta/N)X_\beta$, where X_α and X_β are the mole fractions of the phases, which are assumed to have uniform composition. The total Gibbs free energy of this system is given by

$$G(N^A,N^B) = N_\alpha G^m_\alpha(X_\alpha) + N_\beta G^m_\beta(X_\beta). \tag{2.24}$$

The chemical potentials for each phase are [31]

$$\mu^m_\alpha = \frac{\partial G^m_\alpha}{\partial X_\alpha}, \quad \mu^m_\beta = \frac{\partial G^m_\beta}{\partial X_\beta}, \tag{2.25}$$

The system is at chemical equilibrium when $\mu^m_\alpha = \mu^m_\beta$. The equilibrium compositions X^e_α and X^e_β at which $\mu^m_\alpha = \mu^m_\beta$ can be found by constructing the common tangent of $G_\alpha(X)$ and $G_\beta(X)$, which is illustrated in Fig. 2.1 [61]. The number of moles of α phase, N_α, present in a two-phase mixture at equilibrium is determined by the lever rule, i.e.,

$$N_\alpha = N\frac{\bar{X} - X_\beta}{X_\alpha - X_\beta}, \tag{2.26}$$

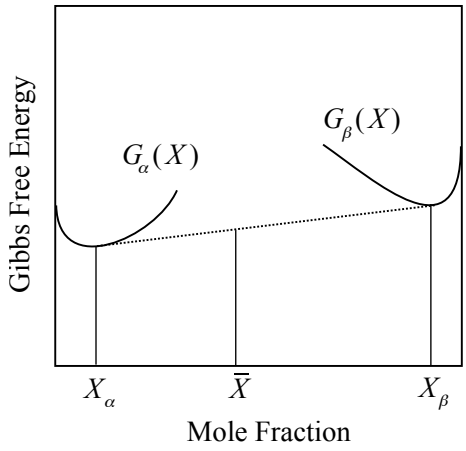

Figure 2.1: Illustration of Gibbs free energy as a function of composition for a two-component system. The dotted line is the common tangent, which indicates the equilibrium Gibbs free energy of the two-phase system, and X_α^e and X_β^e indicate the equilibrium compositions of the phases.

and the total volume of α-phase, V_α, is determined by its molar volume V_α^m by $V_\alpha = N_\alpha V_\alpha^m$.

It is important to note that an additional assumption is required to fix the total volume of this system, $V = V_\alpha + V_\beta$. The phase field models employed here are derived for phase transformations near critical points [62, 63, 64], where it is reasonable to assume that the molar volumes of the phases are equal and constant, $V_\alpha^m = V_\beta^m = V^m$. This assumption has also been adopted for modeling binary solid-liquid mixtures [65], and in both cases it fixes the total system volume. Therefore we adopt it here. Other assumptions are possible for late-stage coarsening, notably constant volume fractions of the phases [52]. With volume and pressure both fixed, the chemical potentials with respect to the Gibbs free energy and Helmholtz free energy are the same [66],

$$\mu^m = \frac{\partial F^m}{\partial X} = \frac{\partial G^m}{\partial X}, \tag{2.27}$$

where F^m is the Helmholtz free energy per mole.

Additionally, phase field models employ volumetric free energy densities, i.e., energy per volume rather than energy per mole. The volumetric free energy density is denoted by $f(X)$, and it is

related to the molar Helmholtz free energy by the molar volume,

$$f(X) = \frac{F^m(X)}{V^m}. \tag{2.28}$$

We denote the chemical potential with respect to $f(X)$ by μ, having used μ^m for the chemical potential with respect to the molar Gibbs free energy G^m. The chemical potential μ is given by

$$\mu = \frac{\partial f_\alpha(X)}{\partial X}. \tag{2.29}$$

Since V^m is constant, the condition for chemical equilibrium between phases is $\mu_\alpha = \mu_\beta$, just as for chemical potentials with respect to the molar Gibbs free energies.

2.2.2 Interfacial energy and Gibbs-Thomson effect

The addition of an interface increases the energy of the system. Interfacial energy can be anisotropic, where it depends on the orientation of the interface relative to a crystalline lattice, or isotropic, where it has no such dependence. The anisotropic case is considered in Chapter 6, and therefore we will consider only isotropic interfacial energy here. The excess interfacial energy per unit area is denoted by γ, and the total energy of a two-phase system, including both bulk and interface contributions, can be written as

$$F = V_\alpha f_\alpha(X_\alpha) + V_\beta f_\beta(X_\beta) + \gamma A. \tag{2.30}$$

The phases can change volume by absorbing more or less mole fraction, X, than their bulk equilibrium mole fractions X_α^e and X_β^e. This change in volume increases the total bulk free energy, $V_\alpha f_\alpha(X) + V_\beta f_\beta(X)$, from its bulk equilibrium state, but it can reduce the total interfacial energy γA.

The balance between the increase in bulk energy and the decrease in interfacial energy (i.e., the equilibrium condition) depends on the geometry of the interface. The Gibbs-Thomson equation

[66, 67] describes local equilibrium at a curved interface,

$$\mu = \mu^e + \frac{2\gamma H}{(X_\beta - X_\alpha)}, \tag{2.31}$$

where H is the mean curvature of the interface and μ^e is the bulk equilibrium chemical potential of the two-phase system (which is also the chemical potential at a planar interface, $H = 0$). Note that the factor $2H$ here also appears in Eq. 2.13 for the evolution of the element of area at a point on the surface. In both cases it denotes how much area changes due to a normal motion of the interface.

The change in X resulting from this change in chemical potential can be found by expanding the chemical potential about the equilibrium mole fraction [31], e.g.,

$$\mu_\alpha = f'_\alpha(X_\alpha) = f'(X^e_\alpha) + \Delta X_\alpha f''(X^e_\alpha) + \mathscr{O}\left[(\Delta X_\alpha)^2\right], \tag{2.32}$$

for the α-phase, where ΔX_α is the change in mole fraction, $\Delta X_\alpha = X_\alpha - X^e_\alpha$. The notation $\mathscr{O}\left[(\Delta X_\alpha)^2\right]$ signifies that the next term is proportional to ΔX_α. Assuming ΔX_α is small, Eqs. 2.31-2.32 allow ΔX_α to be expressed as,

$$\Delta X_\alpha = 2H l^c_\alpha, \tag{2.33}$$

where the quantity

$$l^c_\alpha = \frac{\gamma}{(X^e_\beta - X^e_\alpha) f''_\alpha(X^e_\alpha)}, \tag{2.34}$$

is known as the capillary length of the α phase [31]. We will refer to the effect of curved interfaces on composition and chemical potential due to Eqs. 2.31 and 2.33 as the Gibbs-Thomson effect.

The Gibbs-Thomson effect is closely related to the effect of interfaces on fluids. For fluids, the Young-Laplace equation relates pressure in the fluid to the quantity $2\gamma H$, rather than chemical potential [68, 69, 70, 71]. The contribution of Gibbs [67] was to relate the effect of interfacial energy to chemical potential, which is more physically appropriate than pressure for describing evolution in solids [66, 72]. Differences in chemical potential caused by the Gibbs-Thomson effect provide the driving force for coarsening. Transport mechanisms, the topic of the next two

subsections, are necessary for that driving force to result in evolution.

2.2.3 Coarsening via bulk diffusion

Coarsening in many systems occurs via diffusive mass transport through the bulk of the phases, i.e., by bulk diffusion. Here we obtain equations that govern X (and, by the definition in Eq. 2.29, μ) in the bulk, and an expression for the velocity of the interface. Together with the Gibbs-Thomson equation, which determines μ at the interface, these equations describe the dynamics of coarsening via bulk diffusion.

The principles of irreversible thermodynamics [73, 74] dictate that a gradient in μ results in a flux $\vec{j}$ of X,

$$\vec{j} = -M\nabla\mu, \tag{2.35}$$

where the Onsager coefficient M is the chemical mobility of X. The mole fraction X is locally conserved, and its evolution in time is therefore governed by the continuity equation,

$$\frac{\partial X}{\partial t} + \nabla\cdot\vec{j} = 0. \tag{2.36}$$

Combining Eqs. 2.35 and 2.36 yields the diffusion equation,

$$\frac{\partial X}{\partial t} = \nabla\cdot M\nabla\mu, \tag{2.37}$$

which describes the evolution of the mole fraction X in the bulk of the phases. The motion of the interface is determined by a mass balance,

$$v_n X|_-^+ + \vec{n}\cdot\vec{j}|_-^+ + \nabla_s\cdot\vec{j} = 0, \tag{2.38}$$

where $|_-^+$ denotes quantities evaluated on either side of the interface (i.e., $X|_-^+ = (X_\alpha - X_\beta)$), and $\nabla_s\cdot$ denotes the surface divergence. The terms containing $\vec{j}$ in Eq. 2.38 differ from Eq. 2.36 because

the normal fluxes are discontinuous at the interface. For bulk diffusion, the surface term $\nabla_s \cdot \vec{j}$ is neglected [75], leaving

$$v_n = -\frac{\vec{n} \cdot \vec{j}|_-^+}{X|_-^+}, \tag{2.39}$$

as the expression for the motion of the interface. When the diffusion field is in fact time-dependent, Eqs. 2.37 and 2.39 correspond to growth rather than coarsening [31, 76]. Once the diffusion field has reached steady state, the chemical potential satisfies the Laplace equation,

$$\nabla^2 \mu = 0. \tag{2.40}$$

Eqs. 2.31, 2.39, and 2.40 govern the dynamics of coarsening via bulk diffusion. They were first presented in this form by Mullins and Sekerka [75].

2.2.4 Coarsening via surface diffusion

Coarsening via surface diffusion occurs due to the same driving force as bulk diffusion under circumstances where transport is limited to the interface (e.g., in deeply quenched polymer blends [77] and nanoporous metals at low temperatures [16, 22, 78]). Since in this case the transport, interfacial motion, and chemical potential are all defined at the interface, the dynamics can be expressed in a single governing equation, first derived by Mullins [79]. This equation is,

$$v_n = -\eta \nabla_s^2 H, \tag{2.41}$$

where the coefficient η contains the interfacial energy and transport coefficient for surface diffusion, and ∇_s^2 is the surface Laplacian.

2.3 Theoretical methods for coarsening

As noted in Chapter 1, an extensive literature exists for coarsening of particulate systems (see, e.g., Refs. [23, 24, 28, 29, 31, 32]). Models for particulate systems take advantage of geometric assumptions, like spherical symmetry of the particle and the concentration or chemical potential field around it. This section instead focuses on two theoretical methods that are applicable to any two-phase system: dynamic scaling and the geometrically general theory of DeHoff [52].

2.3.1 Dynamic scaling

Dynamic scaling (i.e., self-similarity) is the time independence of the morphology when it is scaled by the time-dependent characteristic length scale of the evolving system [33]. It can refer to scaling of the evolving geometry itself (e.g., in the case of a single spherical particle) or to statistical descriptions of the morphology. For example, distribution $f(r,t)$, where r has dimension length, satisfies $f[r/L(t_1),t_1] = f[r/L(t_2),t_2]$ for any times t_1 and t_2 during self-similar evolution, where $L(t)$ is the time-dependent characteristic length scale.

Scaling power laws that relate time and L during self-similar evolution are specified by the dimensionality of the governing equations for the problem The power laws for coarsening via bulk and surface diffusion were first obtained by Herring [80], and we will use a method from Ref. [81] to derive them here. Scaling dimensional quantities by the characteristic time scale T and length scale L reduces the governing equations to the power law relationship between T and L. All of the remaining physical and geometric parameters go into the coefficient for this power law, which will be time-invariant if the evolution is self-similar.

Considering surface diffusion (Eq. 2.41) first, the scaled interfacial velocity is $\tilde{v}_n = v_n T/L$, the scaled surface Laplacian is $\tilde{\nabla}_s^2 = L^2\nabla_s^2$, and the scaled mean curvature is $\tilde{H} = LH$. Substituting the scaled quantities into Eq. 2.41 results in

$$v_n \frac{T}{L} = -\eta L^2 \tilde{\nabla}_s^2 L\tilde{H}$$

$$T = L^4 \left(-\eta \frac{\tilde{\nabla}_s^2 \tilde{H}}{\tilde{v}_n} \right). \tag{2.42}$$

Thus, the length scale evolves according to $T^{1/4}$ during self-similar coarsening via surface diffusion.

For coarsening via bulk diffusion, the scaling relationship is captured by the Gibbs-Thomson equation (Eq. 2.31) and the interfacial mass balance (Eq. 2.39). The Laplace equation (Eq. 2.40) determines $\nabla\mu$ but does not otherwise affect scaling. Defining the scaled chemical potential $\tilde{\mu} = 2\gamma\tilde{H}/X|_-^+$ and scaled gradient $\tilde{\nabla} = L\nabla$, and reusing $\tilde{v}_n$ and $\tilde{H}$ from the surface diffusion case, the evolution of the interface can be expressed as

$$\tilde{v}_n \frac{T}{L} = \frac{L^2 \vec{n} \cdot \tilde{\nabla}\tilde{\mu}|_-^+}{X|_-^+}$$

$$T = L^3 \left(\frac{\vec{n} \cdot \tilde{\nabla}\tilde{\mu}|_-^+}{X|_-^+} \right). \tag{2.43}$$

Thus, the power law for self-similar coarsening via bulk diffusion is $T \propto L^3$.

The scaling power laws are geometrically general [82]; they apply to both the large-scale coarsening dynamics considered in this work and to self-similar evolution of simple geometries, like a nearly flat plane [83]. This makes the scaling power laws important tools for understanding coarsening within complex microstructures, and they will be applied throughout subsequent chapters. It should also be noted that while a self-similarly evolving system must coarsen according to the scaling power law for its dynamics, the reverse is not necessarily true. Systems that do not exhibit self-similarity can and do exhibit coarsening kinetics that agree with the power law [10, 40, 43, 84, 85]. In Chapter 7, we show that this can occur when a length scale is kinetically inactive during coarsening. Features can be sufficiently large that they contribute negligibly to the coarsening rate, which is then determined by a self-similarly evolving population of smaller features.

2.3.2 Geometrically general theory

Here, we describe a geometrically general theory of coarsening for bulk diffusion developed by DeHoff [52], which will be applied in Chapters 4 and 8. The core of the theory is an observation that every point on the interface is connected to one other point (its connected neighbor) via a line of constant flux through each phase in which diffusion occurs. The gradient of the chemical potential normal to the interface can be represented as,

$$\vec{n} \cdot \nabla \mu = \frac{2\gamma}{(X_\beta - X_\alpha)} \frac{(H - H_n)}{\lambda}, \tag{2.44}$$

where H_n is the mean curvature of the connected neighbor interface and λ, the diffusional interaction distance, results from a linearization of $\nabla\mu$, $\lambda = \Delta\mu/(\vec{n} \cdot \nabla\mu)$. DeHoff's theory considers diffusional interactions through a single phase, resulting in the following expression for the velocity of the interface,

$$v_n = \frac{K_D}{\lambda}(H_n - H), \tag{2.45}$$

where the kinetic coefficient K_D is $2M\gamma/(X_\beta - X_\alpha)^2$.

On its own, Eq. 2.45 does not provide any additional information about the coarsening problem, since H_n and λ are determined by the solution to the Laplace equation (Eq. 2.40) However, when combined with the following geometric identities [52],

$$\frac{\partial V_\beta}{\partial t} = \int_S v_n dA, \tag{2.46}$$

$$\frac{\partial A}{\partial t} = -\int_S 2 v_n H dA, \tag{2.47}$$

it can provide useful information about the evolution of the entire structure. DeHoff supplements Eqs. 2.45, 2.46, and 2.47 with two additional assumptions to obtain a relationship used in Chapter 4. The first assumption is that the volume of β phase is constant in time, i.e., $dV_\beta/dt = 0$ in Eq.

2.46. With this assumption, the averages of H and H_n over the surface are equal,

$$\langle H_n \rangle = \langle H \rangle . \tag{2.48}$$

The second assumption is that H, H_n, and λ are statistically uncorrelated. Using these assumptions, the following expression can be derived by substituting Eq. 2.45 into Eq. 2.47,

$$\frac{dA}{dt} = -2AK_D \left\langle \frac{1}{\lambda} \right\rangle \left(\left\langle H^2 \right\rangle - \langle H \rangle^2 \right), \tag{2.49}$$

where the quantity $\left\langle H^2 \right\rangle - \langle H \rangle^2$ is the variance of mean curvature. In summary, if its assumptions are satisfied, this theory relates the change in total area of the system to a measure of the global morphology, the variance of mean curvature.

Chapter 3

Methods

This chapter describes how the dynamics described in Chapter 2 were investigated in practice, including the methods for conducting simulations and characterizing the resulting structures. We begin by introducing the phase field model. Specific variants of this model will be introduced in subsequent chapters, but the numerical schemes and parameters that they have in common are summarized here. We also provide a procedure for rescaling dimensional quantities to compare them between simulations with different parameters. Finally, we describe our methods for characterizing the structures resulting from simulations, including characteristic length, interfacial curvatures, and topology.

3.1 Phase field model

Coarsening was simulated in this dissertation using phase field models, which have been widely adopted to study microstructure evolution in materials science (see reviews [86, 87, 88]). Phase field models consider interfaces as diffuse transitions in a continuous variable, such as density or composition. This approach was pioneered by van der Waals for fluids [89, 90], and it is widely used in the physics of critical phenomena [62, 63]. It was first applied to phase transformations in materials science by Cahn and Hilliard [64], and it is their model that will be used here.

The continuous variable we employ is the conserved order parameter ϕ, which may be interpreted as a dimensionless scaled concentration (e.g., $\phi = (X - X_\alpha)/(X_\beta - X_\alpha)$). The free energy

functional $F[\phi, \nabla\phi]$ of the Cahn-Hilliard model is [64],

$$F[\phi, \nabla\phi] = \int_\Omega \left[f(\phi) + \frac{\varepsilon^2}{2} |\nabla\phi|^2 \right] dV, \tag{3.1}$$

where ε is the gradient energy coefficient, and Ω is the domain. Bulk free energy densities $f(X)$ were described in Chapter 2, and the only difference is that the energy of both phases is now described by a single function, $f(\phi)$. For this to result in a two-phase system, $f(\phi)$ must be non-convex (i.e., $f''(\phi) < 0$). This allows the coexistence at equilibrium of two phases with different equilibrium compositions, ϕ_0^+ and ϕ_0^-.

The chemical potential of the Cahn-Hilliard model is the first variation of $F[\phi, \nabla\phi]$ with respect to ϕ,

$$\mu = f'(\phi) - \varepsilon^2 \nabla^2 \phi. \tag{3.2}$$

When ϕ is locally conserved, it evolves according to a generalized diffusion equation [73, 74, 87, 91, 92] that incorporates the chemical potential in Eq. 3.2,

$$\frac{\partial \phi}{\partial t} = \nabla \cdot M \nabla \mu. \tag{3.3}$$

Combining Eqs. 3.2 and 3.3, the Cahn-Hilliard equation is then

$$\frac{\partial \phi}{\partial t} = \nabla \cdot M \nabla \left[f'(\phi) - \varepsilon^2 \nabla^2 \phi \right]. \tag{3.4}$$

We apply this equation and its variants in subsequent chapters. Concentration-dependent mobility is employed in Chapter 4 to study coarsening with dissimilar mobilities between the phases. Two variants with concentration-dependent mobility are examined to study surface diffusion in Chapter 5, and most of our results were obtained with a model in which the chemical potential was also modified (the RRV model, labeled after its authors, Rätz, Ribalta and Voigt). A variant with interfacial energy anisotropy is analyzed in Chapter 6. Chapter 7 employs Eq. 3.4 as written here, and Chapter 8 uses a mobility that is a function of space and time. The specifics of those variants

are discussed in their respective chapters, and information common to them is presented here.

Our simulations often begin with a homogeneous initial condition, where the order parameter is randomly distributed about an average value that satisfies $f''(\phi) < 0$. At early times, the Cahn-Hilliard equation models phase separation, specifically spinodal decomposition [92, 93, 94, 95]. Regions of phase form separated by a diffuse interface with thickness proportional to ε. As the phases reach their equilibrium concentrations, the dynamics of the phase field model converge to the coarsening dynamics introduced in Chapter 2, Eqs. 2.31, 2.39, and 2.40. This convergence can be established mathematically by analysis of the asymptotic limit of zero interfacial thickness [76, 96], i.e., $\varepsilon \to 0$. More information about this method is given in Chapter 6, where it is applied to a model for systems with regularized strongly anisotropic interfacial energy.

Additional information about the model can be obtained by specifying the bulk free energy, which is [64, 92, 97]

$$f(\phi) = \frac{W}{4}\phi^2(\phi-1)^2 \tag{3.5}$$

in subsequent chapters. The minima of $f(\phi)$, $\phi_0^+ = 1$ and $\phi_0^- = 0$, correspond to the equilibrium concentrations of two phases in contact at a planar interface. The parameter W controls the height of the energy barrier between the two energy minima. The interfacial energy γ is given by [64]

$$\gamma = \varepsilon^2 \int_{-\infty}^{+\infty} \left(\frac{d\phi}{dx}\right)^2 dx = \varepsilon \int_{\phi_0^-}^{\phi_0^+} \sqrt{2f(\phi)}\, d\phi = \frac{1}{6}\varepsilon\sqrt{\frac{W}{2}}, \tag{3.6}$$

and the one-dimensional profile of a planar interface is

$$\phi(x) = \frac{1}{2}\left[1 + \tanh\left(\frac{2x}{L_\varepsilon}\right)\right] \tag{3.7}$$

where the interfacial width parameter L_ε is

$$L_\varepsilon = 4\varepsilon\sqrt{\frac{2}{W}}. \tag{3.8}$$

This width parameter is derived using the relationship $f(\phi) = \frac{\varepsilon^2}{2}\left(\frac{\partial\phi}{\partial x}\right)^2$, which is valid at equi-

librium [64]. The maximum of $f(\phi)$ therefore corresponds to the maximum of $\partial\phi/\partial x$, and L_ε represents a lower bound for the distance in x between $\phi = 0$ and $\phi = 1$,

$$L_\varepsilon = \frac{\Delta\phi}{\max(\partial\phi/\partial x)} = \frac{1}{\frac{1}{\varepsilon}f(0.5)} = 4\varepsilon\sqrt{\frac{2}{W}}. \tag{3.9}$$

A comparison between this expression and the expressions for capillary length and γ, Eqs. 2.34 and 3.6, reveals that the interfacial width of the Cahn-Hilliard model is tied to its capillary length for a given form of $f(\phi)$. The capillary length of the $\phi = 0$ phase is

$$l^c = \frac{\gamma}{f''(0)} = \frac{\frac{1}{6}\varepsilon\sqrt{\frac{W}{2}}}{\frac{W}{2}} = \frac{1}{24}L_\varepsilon. \tag{3.10}$$

3.2 Numerical methods

Finite differences were employed to solve the Cahn-Hilliard equation numerically. The spatial domain was discretized by a uniform grid. The Laplacian of the order parameter in Eq. 3.2 was approximated by the conventional five-point stencil in two dimensions (2D), which contains seven points in three dimensions (3D) [98]. This can be expressed as

$$\nabla^2\phi_{i,j} = \frac{1}{4\Delta x^2}\left(\phi_{i+1,j} + \phi_{i-1,j} + \phi_{i,j+1} + \phi_{i,j-1} - 4\phi_{i,j}\right) + \mathscr{O}(\Delta x^2), \tag{3.11}$$

where i and j are the indices of the grid points in the x and y directions and $\mathscr{O}(\Delta x^2)$ indicates that the leading order truncation error is proportional to Δx^2. This approximation of the Laplacian is also used for the term $\nabla \cdot M\nabla\mu$ when the mobility is constant.

Chapters 3, 4, and 8 include models where M is spatially varying, either due to a dependence on ϕ (Chapters 4 and 5) or due to an explicit spatial dependence (Chapter 8). In these cases, $\nabla \cdot M\nabla\mu$ in Eq. 3.4 was approximated by computing $M(\phi)\nabla\mu$ on half-points (i.e., halfway between grid points), and taking a centered difference to find the divergence $\nabla \cdot M(\phi)\nabla\mu$ on the grid points. In

2D, this approximation is

$$\nabla \cdot M\nabla\mu = \frac{1}{(\Delta x)^2}\left(\frac{1}{2}\left[M(\phi_{i+1,j})+M(\phi_{i,j})\right](\mu_{i+1,j}-\mu_{i,j}) - \frac{1}{2}\left[M_{i,j}+M_{i-1,j}\right](\mu_{i,j}-\mu_{i-1,j})\right.$$
$$\left. + \frac{1}{2}\left[M(\phi_{i,j+1})+M(\phi_{i,j})\right](\mu_{i,j+1}-\mu_{i,j}) - \frac{1}{2}\left[M(\phi_{i,j})+M(\phi_{i,j-1})\right](\mu_{i,j}-\mu_{i,j-1})\right)$$
$$+ \mathscr{O}(\Delta x^2). \quad (3.12)$$

This is similar to an approximation in Ref. [99], although they computed $M(\phi)$ using ϕ on the half-point, e.g., $M[\frac{1}{2}(\phi_{i,j}+\phi_{i-1,j})]$.

Periodic boundary conditions were enforced in all simulations. That is, in one dimension, $\phi(0,t) = \phi(L_x,t)$ and $\phi'(0,t) = \phi'(L_x,t)$ at all times t, where L_x is the length of the domain. These were implemented by extending the grid outside of its domain to 'ghost points,' into which order parameter or chemical potential values were copied from the opposite edge/face of the domain. Random initial conditions were employed extensively, and were implemented by assigning values to grid points sampled from a uniform random distribution centered about the desired average composition.

The time discretization was an explicit Euler scheme. Denoting the value of the order parameter at iteration n by ϕ_n, this scheme can be expressed as

$$\phi_{n+1} = \phi_n + \Delta t\left(\frac{\partial\phi}{\partial t}\right)_n + \mathscr{O}(\Delta t) \quad (3.13)$$

where Δt is the timestep and $\mathscr{O}(\Delta t)$ indicates that the truncation error is proportional to Δt. The order parameter was output at regular intervals in time. Simulation times reported in this dissertation are exact, and only the necessary level of precision is provided (e.g., 4×10^3 rather than 4.00×10^3).

Table 3.1: Summary of constant mobility bulk diffusion simulations. Each simulation is indicated by the chapters in which they are referenced, the average order parameter $\langle\phi\rangle$, the initial condition (RN for random noise, or AC for phase-separated by Allen-Cahn dynamics), the length of the cubic domain, L_x, and the duration of the simulation, t_f.

Chapters	$\langle\phi\rangle$	IC	L_x	t_f
4,5, 8.1	0.50	RN	1024	4×10^5
5, 8.1	0.36	RN	1024	10^6
8.1	0.34	RN	1280	1.2×10^6
5, 8.1	0.32	RN	1024	10^6
5	0.30	RN	1024	4×10^5
8.1	0.50	AC	800	1.6×10^5
8.2	0.50	RN	512	4×10^5

3.3 Simulation parameters

All of the coarsening simulations in this dissertation (i.e., excluding the equilibrium shape calculations in Chapter 6) have parameters $\varepsilon^2 = 0.2$ and $W = 0.4$, which result in an interfacial energy of $\gamma = 1/30$ and interfacial width parameter of $L_\varepsilon = 4$ from Eqs. 3.6 and 3.8, respectively. The grid spacing in coarsening simulations was $\Delta x = 1$, resulting in 3-5 points through the interface. The timestep of coarsening simulations was $\Delta t = 0.05$, except for simulations with the RRV surface-diffusion model, which had $\Delta t = 0.04$. Simulations were conducted in cubic domains with side lengths L_x from the initial time $t = 0$ to a final time t_f. The parameters for coarsening simulations with constant mobility are summarized in Table 3.1. RN indicates that the simulation is initialized via random noise about the average composition specified by $\langle\phi\rangle$, and the AC initial condition is described in Section 8.1.

3.4 Nondimensionalization and rescaling

Solutions to Eq. 3.4 with different parameters correspond to solutions to a dimensionless Cahn-Hilliard equation scaled in length and time. To make comparisons to other works that use different forms of the Cahn-Hilliard equation and associated parameters (i.e., [55] and [100]), here we provide a procedure for rescaling to match our parameters. In addition to the parameters ε, M, and

W, the primary difference is in the bulk free energy, $f(\phi)$, that affects the range of ϕ between the two equilibrium values. We consider only models with the same functional forms of the bulk free energy that can be rescaled to a dimensionless function $g(\tilde{\phi})$ by

$$g(\tilde{\phi}) = 16\left(\frac{1}{4} - \tilde{\phi}^2\right)^2 = \frac{1}{\hat{F}} f\left(\frac{\phi - \phi_c}{\hat{\Phi}}\right),$$

where $\hat{F}$ is the height of the double well free energy that is used as the energy density scale, $\hat{\Phi}$ is the difference between the two equilibrium concentrations, and ϕ_c is the midpoint of the equilibrium concentrations. The concentration ϕ_c only shifts the concentration range and will not affect spatial or temporal scaling.

While any scaling length can be chosen for nondimensionalization, we select one that is associated with the interfacial width to rescale all models. The scaling length $\hat{L}$ can now be defined as

$$\hat{L} = \frac{\varepsilon\hat{\Phi}}{\sqrt{2\hat{F}}}, \tag{3.14}$$

which is a generalization of L_ε in Eq. 3.8. The characteristic time $\hat{T}$ associated with $\hat{L}$ is then determined by dimensional analysis of Eq. 3.4,

$$\frac{\hat{\Phi}}{\hat{T}} = \frac{M}{\hat{L}^2}\frac{\hat{F}}{\hat{\Phi}}$$

$$\hat{T} = \frac{\hat{\Phi}^2\hat{L}^2}{M\hat{F}} \tag{3.15}$$

Defining the dimensionless coordinates $\tilde{t} = t/\hat{T}$, $\tilde{x} = x/\hat{L}$, and the dimensionless concentration $\tilde{\phi} = (\phi - \phi_c)/\hat{\Phi}$, the non-dimensional Cahn-Hilliard equation is now given by

$$\frac{\partial\tilde{\phi}}{\partial\tilde{t}} = \tilde{\nabla}^2\left[g'(\tilde{\phi}) - 2\tilde{\nabla}^2\tilde{\phi}\right]. \tag{3.16}$$

For two given simulations A and B, we can now rescale the simulation time t_A from simulation

A to that corresponding to the time t_B as measured in simulation B:

$$\tilde{t} = \frac{t_A}{\hat{T}_A} = \frac{t_B}{\hat{T}_B}$$

$$t_B = \left(\frac{\hat{T}_B}{\hat{T}_A}\right) t_A. \tag{3.17}$$

To compare the coarsening rate constant k in Eq. 4.3 between simulations, we define the dimensionless coarsening rate constant $\tilde{k} = k\hat{T}/\hat{L}^3$. The coarsening rate constant k_A measured in simulation A can now be rescaled to match the length and time scales employed in simulation B:

$$\tilde{k} = \frac{k_A \hat{T}_A}{\hat{L}_A^3} = \frac{k_B \hat{T}_B}{\hat{L}_B^3}$$

$$k_B = \left(\frac{\hat{T}_A \hat{L}_B^3}{\hat{T}_B \hat{L}_A^3}\right) k_A. \tag{3.18}$$

Eqs. 3.17 and 3.18 were used to compare the timescale in Ref. [100] and the coarsening rate constant in Ref. [55], respectively, to the corresponding values in Chapter 4.

3.5 Characterization methods

Simulated structures were characterized in terms of characteristic length, morphology, and topology. The characteristic length is defined as the domain volume per unit of interfacial area, denoted by S_V^{-1} [40, 42, 53], and S_V^{-1} is also used to denote the analogous characteristic length in two dimensions, the ratio of area to interfacial length. In the following subsections, we define the quantities by which curvature and topology are characterized, and the methods by which those quantities are calculated. We also introduce the scaled quantities that enable evaluation of self-similarity.

3.5.1 Interfacial morphology

The order parameter data resulting from the simulation was post-processed using a level-set based method [101]. The interface of each structure was approximated as a triangular mesh of the $\phi = 0.5$ isosurface. Mean curvature H and Gaussian curvature K were calculated on the simulation grid and interpolated to the centers of mesh triangles. Surface integrals were discretized using the mesh faces: $\int_S q dA = \sum_i q_i A_i$, where q_i and A_i correspond to the value of q and the area of the ith mesh face.

This method was used to calculate statistics of interfacial morphology, including average mean curvature $\langle H \rangle$, standard deviation of mean curvature σ_H, and the interfacial shape distribution (ISD). The ISD [41, 42] is a probability density function that represents the probability of finding a point on the interface with a specific pair of principal curvatures, (κ_1, κ_2), which are related to H and K by $H = (\kappa_1 + \kappa_2)/2$ and $K = \kappa_1 \kappa_2$. The ISD can be defined mathematically as

$$P(\kappa_1', \kappa_2') = \frac{1}{A} \int_S \delta(\kappa_1 - \kappa_1') \delta(\kappa_2 - \kappa_2') dA, \tag{3.19}$$

where $\delta(x)$ is the delta function. Figure 4.8 shows this type of ISD, and additional examples can be found in Chapters 5 and 8. Analogously to the 3-D case, we define the ISD of a 2-D structure as the probability of a point on the interface having a specific scalar curvature κ, i.e.,

$$P(\kappa) = \frac{\int_S \delta(\kappa - \kappa') ds}{\int_S ds}. \tag{3.20}$$

This type of ISD is shown in Fig. 4.3. In Chapter 7, a radius-of-curvature distribution is employed instead. This takes the form,

$$P(R) = \frac{\int_S \delta(R - R') ds}{\int_S ds}, \tag{3.21}$$

where $R = 1/\kappa$ is the radius of curvature. Figures 7.7 and 7.6 are examples of this type of ISD.

3.5.2 Topology

Topology of the structures was evaluated in terms of the genus density $g_V = g/V$ of the $\phi = 1$ phase. The genus of a closed surface is related to its Euler characteristic by $\chi = 2 - 2g$ [102]. We note that a different relationship, $\chi = 1 - g$, applies to the Euler characteristic of one of the phase volumes [20, 103].

Euler characteristic χ of the mesh was calculated using Euler's formula [104], $\chi = V - E + F$, where V is the number of vertices, E the number of edges, and F the number of faces. We perform this calculation so that our periodic structure represents a small unit cell of a much larger structure that is closed at some external boundary. To correctly calculate the genus density corresponding to the larger structure, the contribution of elements (edges and vertices) at domain boundaries was halved to account for those elements being shared between two unit cells [103]. Another consideration is that any independent particles in the structure represent separate closed surfaces and add $+2$ to the Euler characteristic. The number of independent particles N was calculated using the LABEL_REGION function in IDL, with an additional algorithm to account for connections through the periodic boundaries. The genus density g_V was then calculated as $g_V = (N - \frac{1}{2}\chi)/V$. Topology is related to interfacial curvature via the Gauss-Bonnet theorem, which is expressed as

$$g_V = \frac{1}{4\pi V} \int_S K dA \tag{3.22}$$

for g_V as computed here.

3.5.3 Morphological scaling

To assess whether the dynamic scaling hypothesis (Section 2.3.1) is being satisfied, we have reported morphological and topological quantities that are scaled by the characteristic length, S_V^{-1}. Scaled mean curvature is H/S_V, scaled Gaussian curvature is K/S_V^2, and scaled genus density is $g_V S_V^{-3}$. The ISDs are reported in terms of scaled principal curvatures κ_1/S_V and κ_2/S_V. Additionally, we note that the Gauss-Bonnet theorem (Eq. 3.22) can be expressed in terms of scaled

quantities as

$$\frac{1}{4\pi}\frac{\int_S K S_V^{-2} dA}{A} = g_V S_V^{-3}. \tag{3.23}$$

That is, the scaled genus density $g_V S_V^{-3}$ is proportional to the average of the scaled Gaussian curvature K/S_V^2 over the interface.

Chapter 4

Simulation of coarsening in two-phase systems with dissimilar mobilities

4.1 Introduction

As discussed in Chapter 1, many experimental systems have two phases with dramatically different mobilities, especially solid-liquid systems [41, 42, 44, 45, 46]. To help bridge the gap between these systems and the idealized systems that have been considered in previous simulation studies [53, 54, 55], we examine how dissimilar mobilities of two phases affects the coarsening of an otherwise idealized system.

To numerically implement dissimilar mobilities of the two phases, we employ a concentration-dependent mobility. Such an approach was originally used to study phase separation via surface or interfacial diffusion [105, 106] and spinodal decomposition with a glassy phase [99, 107, 108]. They have also been applied to two-dimensional (2-D) studies of coarsening with dissimilar mobilities [100, 109, 110]. Sheng et al. [109] studied coarsening in both the one-sided (zero mobility in one phase) and dissimilar-mobility cases. They found a fitted coarsening exponent of $1/3.3$ (i.e., $L \propto t^{1/3.3}$) and scaling of the pair correlation function, a measure of morphology, by the first moment of the structure function, one of the characteristic length scales they examined. Similarly, Ju et al. [110] reported a fitted coarsening exponent of $1/3.2$ for the one-sided case. However, in contrast to those results, Dai and Du predicted [100] reported agreement with the $t^{1/3}$ power law.

In three dimensions, simulations of coarsening with a one-sided mobility were recently carried out [111], but the resulting morphologies were not characterized.

In this chapter, we aim to understand how dissimilar mobilities affects the coarsening morphology and kinetics of complex microstructures in two and three dimensions (2D and 3D, respectively). We present a general phase field model for evolution via bulk diffusion of a two-phase system with dissimilar mobilities. Then, we present simulations with dissimilar mobilities in 2D and 3D with large sample microstructures. Coarsening kinetics and morphological evolution are analyzed, and morphologies are quantified using statistical measures such as the interfacial shape distribution (ISD) [41, 42, 112]. Results with constant mobility are presented for comparison. In the 2-D case, our results address the question of whether coarsening dynamics follow the theoretical $t^{1/3}$ power law introduced in Section 2.3.1. In the three-dimensional (3-D) case, we relate morphology and kinetics using the model introduced in Section 2.3.2.

4.2 Model

In order to study coarsening in systems where the phases have dissimilar mobilities, we employ the Cahn-Hilliard equation with concentration-dependent mobility. The form of the concentration-dependent mobility $M(\phi)$ determines its sensitivity to changes in concentration. Following the approach taken in phase field modeling of solid-liquid systems [113, 114], we express $M(\phi)$ in the general form

$$M(\phi) = (M^+ - M^-)h(\phi) + M^-, \tag{4.1}$$

where $M(\phi_0^+) = M^+$ and $M(\phi_0^-) = M^-$ are the desired bulk mobilities ($M^+ > M^-$ in this study), and $h(\phi)$ is a smooth interpolation function that satisfies $h(\phi_0^+) = 1$ and $h(\phi_0^+) = 0$. Changes in mobility resulting from deviation in concentration in the bulk (e.g., due to the Gibbs-Thomson effect) can affect dynamics if the corresponding bulk mobility is set to be small [81, 115, 116, 117, 118], and the form of $h(\phi)$ determines how much $M(\phi)$ changes when ϕ deviates from its

equilibrium values, $\phi_0^{\pm}$. We therefore select the polynomial interpolation function,

$$h(\phi) = \phi^3(10 - 15\phi + 6\phi^2), \tag{4.2}$$

to sharpen the transition of the mobility from M^- to M^+ near $\phi = 0.5$. As in the sinusoidal interpolation used in Ref. [109], this polynomial form reduces the sensitivity of $M(\phi)$ to the deviation of ϕ from its bulk values compared to linear interpolation, which has been used more commonly [100, 109, 110].

The effect of the choice of interpolation function on the mobility of the low-mobility phase can be demonstrated by considering a small difference in concentration ω, where $\phi = \phi_0^- + \omega$, and expanding the mobility in a Taylor series about ϕ_0^-. For linear $h(\phi)$, $M(\phi) = M^- - \omega h'(\phi_0^-) + \mathscr{O}(\omega^2)$. For our choice of $h(\phi)$, $M(\phi) = M^- - \frac{1}{6}\omega^3 h'''(\phi_0^-) + \mathscr{O}(\omega^4)$. That is, our choice of interpolation function reduces the difference between the desired and actual bulk mobilities, $|M(\phi) - M^-|$, to $\mathscr{O}(\omega^3)$ because it satisfies $h'(\phi_0^{\pm}) = h''(\phi_0^{\pm}) = 0$. In principle, $|M(\phi) - M^-|$ could be reduced to arbitrary order m by requiring that $h^{(m)}(\phi_0^{\pm}) = 0$, but increasing m results in a sharper transition of $h(\phi)$ through the interface (see Fig. 4.1). The interpolation function in Eq. 4.2 represents a compromise between being able to smoothly resolve $M(\phi)$ through the interface and reducing $|M(\phi) - M^{\pm}|$ in the bulk, which is important when one of the mobilities is small.

4.3 Numerical and Characterization Methods

Our simulations are conducted by evolving ϕ according to the Cahn-Hilliard equation, Eq. 3.4, with the concentration-dependent mobility defined by Eqs. 4.1 and 4.2. We set $M^+ = 1$ and $M^- = 10^{-2}$ for the simulations with dissimilar mobilities, and $M = 1$ for the simulations with constant mobility. The sign convention for mean curvature is such that low-mobility-phase convex bodies (e.g., spheres) have positive curvatures.

In 2D, we perform one simulation with constant mobility and one simulation with dissimilar mobilities. In 3D, we perform one simulation with constant mobility and two simulations with

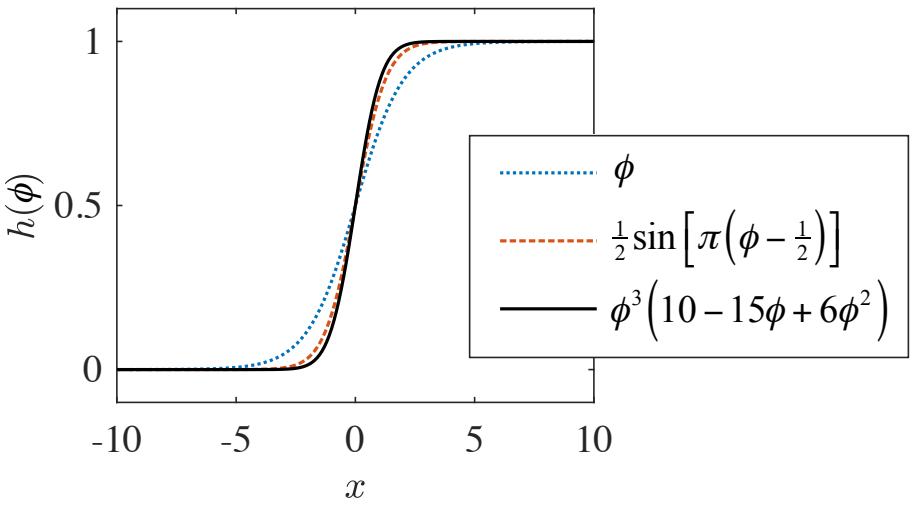

Figure 4.1: Comparison of interpolation functions $h(\phi)$ using the analytical interfacial profile $\phi(x) = \frac{1}{2}[1+\tanh(x/2)]$ (blue dotted curve). The black solid curve is the interpolation function employed in this work. The interpolation function using a sine function from Ref. [85] is also shown by the red dashed curve.

dissimilar mobilities, one with dissimilar mobilities for the entire simulation, and another with constant mobility for phase separation and dissimilar mobilities for subsequent coarsening. We chose to conduct a single simulation for each setup (rather than multiple simulations with smaller domains) to ensure that the simulation domains contained statistically representative structures and that the results are not affected by the periodic boundary conditions imposed on the domain boundaries over the longer simulation times required to examine coarsening. Our simulations were initialized with random noise, and therefore increasing domain size should have the same effect on statistical significance as the averaging of multiple simulations, and the larger domain has the advantage of reduced boundary effects.

4.4 2-D Simulations

Two 2-D simulations were conducted, one with constant mobility and one with dissimilar mobilities, in square domains with sides of length $L_x = L_y = 2844$. Both were initialized with the same random concentration values uniformly distributed within the interval $0.40 - 0.60$. This results

in volume fractions of 50% for both phases at late times, although in the dissimilar-mobilities structure more low-mobility phase is initially present due to its slower rejection of solute.

4.4.1 Morphology

Figure 4.2 depicts the morphology of the simulated 2-D structures during coarsening. The constant mobility structure is shown in Figs. 4.2a-c, and the dissimilar mobilities structure is shown in Figs. 4.2d-e. The portions of the simulated domain presented in Fig. 4.2 are chosen to have the same characteristic area (with the side length $45S_V^{-1}$), enabling us to directly observe morphological changes without the effects of the change in S_V^{-1}. Figures 4.2a and 4.2d show the structures at $t = 4 \times 10^3$, near the end of phase separation. Both structures appear to consist of alternating layers of each phase. While in many locations the layers appear to be flat, they bend and terminate such that the isotropy of the overall structures is preserved. The dissimilar-mobility structure appears to have more high-mobility-phase particles than low-mobility-phase particles, while in the constant-mobility structure, the phases appear to have statistically the same morphology.

As the simulations progress, the constant-mobility structure forms large percolating regions of each phase that contain smaller regions of the opposite phase (Figs. 4.2b and 4.2c). The initially layered structures that were dominated by nearly flat interfaces evolve to more sinuous ones. Overall, these morphological changes are subtle. In contrast, the dissimilar-mobility structure undergoes a significant morphological transition from the initial layered structure to a structure consisting of high-mobility-phase particles in a low-mobility matrix (Figs. 4.2e and 4.2f). This transition occurs through both the disappearance of low-mobility-phase particles and the evolution of high-mobility-phase regions toward their circular equilibrium shape. High-mobility-phase particles also disappear and coalesce, but not rapidly enough to reduce their predominance in the overall structure.

The morphological evolution seen in the simulated structures is quantified by the changes in the ISDs, which are shown in Fig. 4.3. The nearly flat interfaces that are predominant in the layered morphology observed at $t = 4 \times 10^3$ correspond to peaks at $\kappa/S_V = 0$ on the ISDs in Fig.

4.3. In the constant-mobility case, the ISD (Fig. 4.3a) is symmetric about $\kappa/S_V = 0$, which is consistent with the symmetry between the phases: they have the same volume fraction (50%) and, with constant mobility, the same transport kinetics. As the constant-mobility structure evolves, the peak of the ISD remains centered at $\kappa/S_V = 0$, but it broadens over time, with standard deviation σ_{κ/S_V} increasing from 1.0 to 1.3. These changes can be understood in terms of the evolution of three overlapping populations in the ISD: one corresponding to the population having nearly flat interfaces centered at $\kappa/S_V = 0$ and two symmetric populations corresponding to high-curvature features (particles and end-caps of layers) containing each phase appearing between $\kappa/S_V = -2$ and $\kappa/S_V = -1$ and $\kappa/S_V = 1$ and $\kappa/S_V = 2$ In the constant-mobility ISD, the populations of high-curvature features increase symmetrically, while the population with nearly flat interfaces decreases. This may appear unintuitive based on the Gibbs-Thomson condition, but it is not a contradiction because the curvatures are scaled by the characteristic length scale, and overall the interfacial energy is lowered by the reduction of interfaces with large unscaled curvatures as well as the nearly flat interfaces.

The dissimilar-mobility ISD (Fig. 4.3b) is asymmetric at $t = 4 \times 10^3$, with more interface having negative curvature than positive curvature. Negative curvature corresponds to convex high-mobility-phase features, and the asymmetry of the $t = 4 \times 10^3$ ISD is consistent with the greater prevalence of high-mobility-phase particles in Fig. 4.2d. The morphological transition observed in Figs. 4.2d-f is represented in the ISD by the growth of the population centered around $\kappa/S_V = -1.3$ and by the decay of population with positive curvature. The growth near $\kappa/S_V = -1.3$ is due to the longevity of high-mobility-phase domains surrounded by low-mobility-phase matrix observed in Figs. 4.2e and 4.2f. The disappearance of the population with positive curvature corresponds to the loss of low-mobility-phase particles and the evolution of domains of high-mobility phase toward their equilibrium shape, as discussed earlier. Based on the ISDs in Fig. 4.3b, evolution during this simulation is clearly not self-similar, and unlike the constant mobility case, the structure continues to undergo significant evolution even at the latest time we examined.

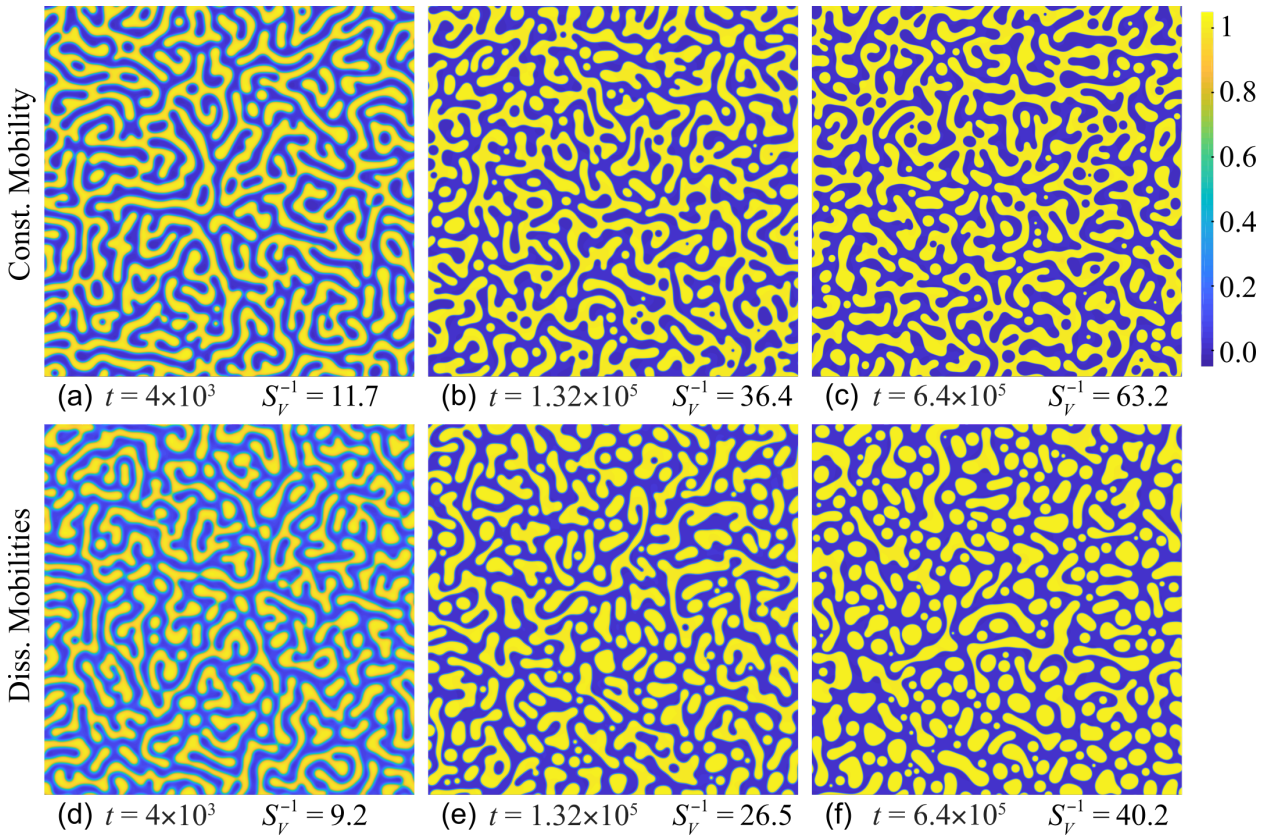

Figure 4.2: Evolution of morphologies in 2D during coarsening with constant mobility (a-c) and dissimilar mobilities (d-f). Each subfigure depicts ϕ within a square subdomain with side length $45S_V^{-1}$. In (d-f), blue indicates the low-mobility phase, while yellow corresponds to the high-mobility phase.

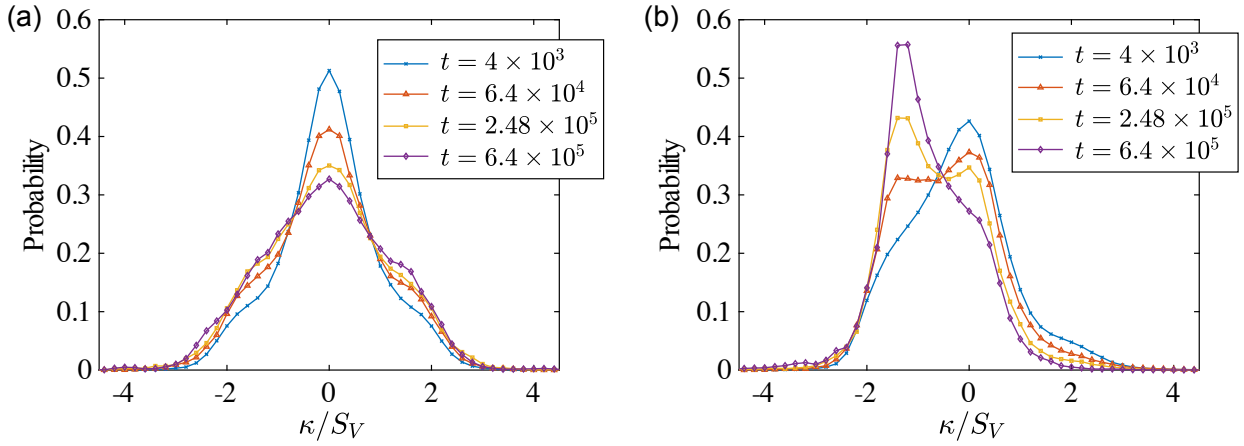

Figure 4.3: Time evolution of interfacial shape distributions (ISDs) of the 2-D structures, (a) coarsened with constant mobility, and (b) coarsened with dissimilar mobilities. ISDs are shown corresponding to four times, $t = 4 \times 10^3$ (blue curve/x-symbols), $t = 6.4 \times 10^4$ (red curve/triangles), $t = 2.48 \times 10^5$ (yellow curve/squares), and $t = 6.4 \times 10^5$ (purple curve/diamonds), which are spaced approximately equally in $t^{1/3}$.

4.4.2 Kinetics

The theoretical $t^{1/3}$ power law for the characteristic length S_V^{-1} is expressed as

$$S_V^{-3}(t) - S_V^{-3}(0) = kt, \tag{4.3}$$

where k is the coarsening rate constant. S_V^{-3} is plotted vs. time in Figs. 4.4a and 4.4b for the constant-mobility and dissimilar-mobility cases, respectively. In the constant-mobility case, the coarsening rate constant increases during an initial transient stage, consistent with the results of [119]. At later times ($t > 2.48 \times 10^5$), a linear fit was used to evaluate convergence to the power law in Eq. 4.3. Good agreement was found, with $R^2 = 0.99996$, and the equation of fit was $S_V^{-3} = 0.409t - 8.93 \times 10^3$. In the dissimilar-mobility case, coarsening rate constant k appears to be decreasing with time over the course of the simulation. Evaluating the coarsening rate constant at the beginning and end of the simulation ($t < 2 \times 10^4$ and $6.2 \times 10^5 < t$, respectively), we find that k decreases from 0.181 to 0.067, a factor of 2.7. The coarsening rate will likely continue to decrease in this case until the scaled morphology reaches a steady state, which may be a particulate structure with circular high-mobility-phase domains embedded in the low-mobility phase.

4.4.3 Discussion

In the dissimilar-mobility case, the complex layered structure resulting from phase separation was observed to transform over time into a system of high-mobility-phase particles in a low-mobility matrix. This transition can be explained in terms of the diffusive interactions between neighboring patches of interface. Interfaces can interact through both phases, but an interface will only coarsen if it has different curvature than the interfaces it is interacting with. We classify two types of geometric features: those that can coarsen via interactions through the high-mobility phase and those that cannot. The first type consists of low-mobility-phase particles (which are surrounded by high-mobility phase) and non-circular high-mobility-phase regions, especially those with complex or elongated shapes. The second type consists of circular high-mobility-phase particles, surrounded

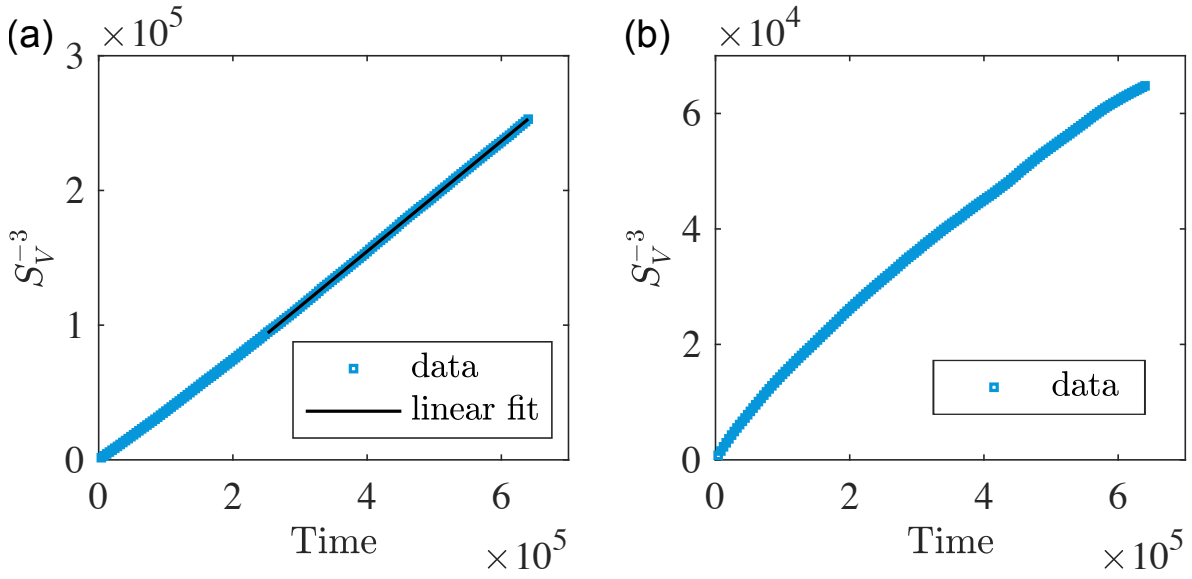

Figure 4.4: Coarsening kinetics of the 2-D structures with (a) constant mobility and (b) dissimilar mobilities. S_V^{-3} is plotted vs. time (blue squares) to evaluate adherence to the power law, and a linear fit (solid black line) is provided for the constant-mobility case.

by low-mobility phase, which can only evolve via interactions through the low-mobility phase because all of the interfaces exposed to that domain of high-mobility phase have the same curvature. The asymmetry in kinetics between these two types of features drives the morphologies observed in Figs. 4.2 and 4.3: low-mobility-phase particles disappear, complex high-mobility-phase particles become circular, and circular high-mobility-phase particles persist. The circular high-mobility-phase particles eventually become the most prevalent feature in the structure.

This morphological transition explains the observed decrease in coarsening rate constant. The area fraction of the circular high-mobility-phase particles surrounded by low-mobility phase increases over time because its evolution is controlled by the diffusion across the low-mobility phase, leading to slower evolution than that controlled by the diffusion across the high-mobility phase. Sheng et al. [109] found $L \propto t^{1/3.3}$ instead of the theoretically predicted $t^{1/3}$ power law, which is consistent with a decrease in the coarsening rate constant (k in Eq. 4.3) over time. We observe a decrease in k, although we do not attribute it to a change in the underlying power law, which is based on the scaling of the governing equations. In contrast, Dai and Du [100] reported agreement with the $t^{1/3}$ power law. We can compare their results to ours using the rescaling methodology

described in Section 3.4.

Dai and Du [100] use $f(\phi) = \frac{1}{4}(\phi^2 - 1)^2$, $\varepsilon = 0.05$, and $M = 1$. The difference in order parameter between the phases at equilibrium is $\hat{\Phi} = 2$ and the height of the double-well free energy is $\hat{F} = 0.25$. Based on Eqs. 3.14 and 3.15, the characteristic length of their system is $\hat{L} = 0.1414$ and the characteristic time is $\hat{T} = 0.32$. In contrast, the present work uses $f(\phi) = \frac{W}{4}\phi^2(1-\phi)^2$ (with $W = 0.4$), $\varepsilon = \sqrt{0.2}$, and $M = 1$, which results in $\hat{\Phi} = 1$ and $\hat{F} = W/64 = 0.00625$. Thus, our characteristic length is $\hat{L} = 4$ and time is $\hat{T} = 2560$. Dai and Du [100] fit the kinetics of a 2-D simulation with a one-sided mobility using times up to $t = 8$. Applying Eq. 3.17, this corresponds to

$$t = \frac{2560}{0.32} \times 8 = 6.4 \times 10^4$$

with our parameters, which is ten times smaller than the latest time in Fig. 4.4. Agreement with the $t^{1/3}$ power law within this early timescale is consistent with our results since the decrease in coarsening rate constant is more evident at later times.

The morphological transition would have been difficult to observe without our use of the ISD to characterize the morphologies of our simulated structures. The structure function and pair correlation function, employed by Sheng et al. [109] to characterize their structures, were previously found to be insensitive to the difference between complex percolating domains and particles embedded in a matrix [95]. Those types of morphology are clearly differentiated in the ISD, and we were able to observe a transition from one type to the other.

4.5 3-D Simulations

Three 3-D simulations were conducted with domains of size $L_x = L_y = L_z = 1024$, initialized with ϕ uniformly distributed within $0.40 - 0.60$ and generated with the same set of random numbers. The first simulation used constant mobility at all times. The second simulation, dissimilar mobilities PS IC (phase-separated initial condition), employed constant mobility until $t = 10^4$ when phase separation was complete, and dissimilar mobilities for subsequent coarsening. The third simula-

tion, dissimilar mobilities RN IC (random noise initial condition), was conducted with dissimilar mobilities for the duration of the simulation, $0 < t \leq 4 \times 10^5$. Two simulations were conducted for the dissimilar-mobility case in 3D in order to determine whether the self-similar state is initial-condition dependent, which was not necessary in the 2-D case because of the lack of a self-similar state.

4.5.1 Morphology

All three simulation conditions resulted in qualitatively similar bicontinuous microstructures. A representative morphology is shown in Fig. 4.5 for the dissimilar-mobility case. Specifically, Fig. 4.5 shows the $\phi = 0.50$ isosurface of the dissimilar-mobility PS IC structure at time $t = 4 \times 10^5$ within a cubic subdomain with side length $8S_V^{-1}$. The isosurface is colored by scaled mean and Gaussian curvature in Figs. 4.5a and 4.5b, respectively. The predominant high-curvature features are necks, four of which are circled. These necks have negative Gaussian curvatures with large magnitudes. Mean curvatures can be positive or negative depending on which phase the neck contains: positive for necks containing low-mobility phase and negative for necks containing high-mobility phase. Negative Gaussian curvature indicates that interfaces are hyperbolic, i.e., they have oppositely signed principal curvatures. As evident in Fig. 4.5, most of the interfaces are either hyperbolic or nearly planar. Elliptic interfaces (with principle curvatures of the same sign) with large positive Gaussian curvatures are also present. However, they are rare and are most likely products of the pinching of necks, which disappear relatively quickly because the same-signed principle curvatures add to the magnitude of the mean curvature that determines the driving force for evolution via the Gibbs-Thomson condition.

Figure 4.6a defines four types of interfaces based on regions of the ISD, which are: 1) nearly flat interfaces, 2) interfaces near the peak of the ISD, 3) interfaces associated with the necks of the low-mobility phase, and 4) interfaces associated with the necks of the high-mobility phase. These interfaces are identified by red highlights in Fig. 4.6b.1-4. As in Fig. 5, the structure is for the dissimilar mobilities PS IC case at time $t = 4 \times 10^5$. Nearly flat interfaces in Fig. 4.6b.1 are

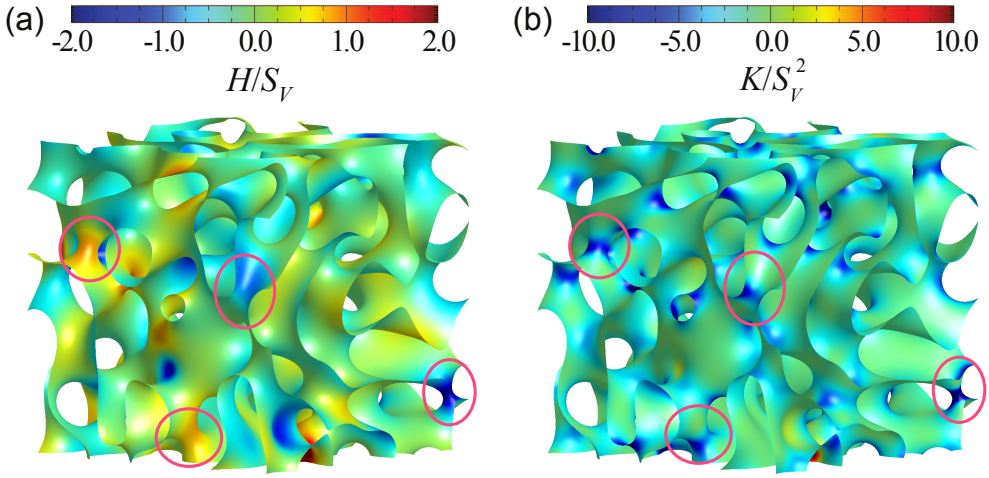

Figure 4.5: Late-time interfacial morphology for the dissimilar-mobility PS IC case at time $t = 4 \times 10^5$. The $\phi = 0.50$ iso-surface is shown colored by (a) scaled mean curvature and (b) Gaussian curvature within a cubic subdomain with side length $8S_V^{-1} = 283$. Four necks are circled, two of which contain high-mobility phase (negative H/S_V) and two of which contain low-mobility phase (positive Gaussian curvature).

present on the structure in small round patches and larger non-circular areas. Interfaces near the ISD peak, highlighted in Fig. 4.6b.2, are present in thin strips of area, some of which appear to partially enclose areas of nearly flat interfaces. Necks were previously identified in Fig. 4.5, and, by comparing it against Figs. 4.6b.3 and 4.6b.4, we observe that regions 3) and 4) of the ISD do correspond to necks in the structures, although some neck areas in Fig. 4.5 are out of the limit of regions 3) and 4) and thus are not highlighted.

Figure 4.7 shows how the integrated probability over each of these ISD regions identified in Fig. 4.6 evolves during coarsening. The constant-mobility case and the dissimilar-mobility case with the phase separated initial condition (dissimilar mobilities PS IC) are identical at $t = 10^4$ because both are simulated with $M = 1$ during the phase separation stage. However, the latter quickly diverges from the constant mobility case, and the probabilities of both dissimilar-mobility cases converge over time to the same late-time values in all of the four types of interfaces. As compared to the constant-mobility structure, the dissimilar-mobility structures have less interfacial area that is nearly flat or near the ISD peak (Figs. 4.7a and 4.7b), and significantly more interfacial area corresponding to high-mobility-phase necks (4.7d), along with slightly more low-mobility-phase

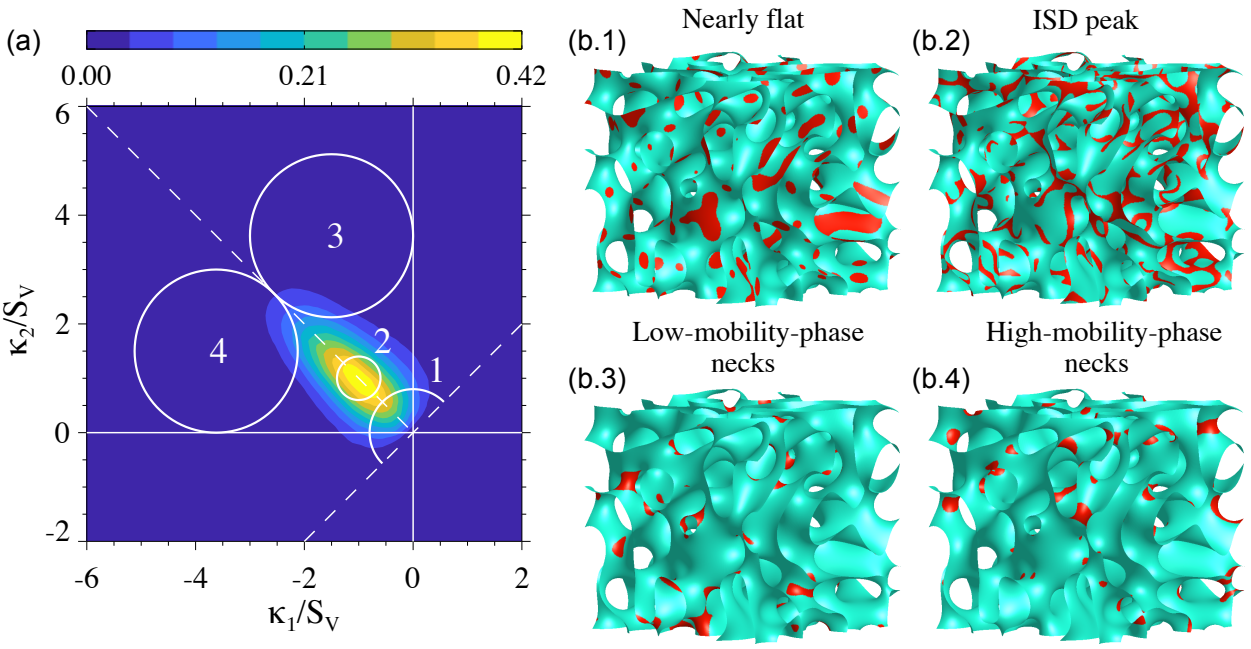

Figure 4.6: (a) ISD and (b) structures identifying four different types of interface: 1) nearly flat interfaces, 2) interfaces at the ISD peak, 3) high-mobility-phase necks, and 4) low-mobility-phase necks. The ISD and structures shown are for the dissimilar-mobility PS IC case at time $t = 4 \times 10^5$.

necks (4.7c).

The constant-mobility ISD does not evolve substantially, except for a slight increase in the amount of area corresponding to necks at early times. The neck probabilities must be statistically identical in the constant-mobility ISD due to kinetic and compositional symmetries, and therefore the observed changes in neck probabilities at late times represent statistical uncertainty due to our finite sample size. In all cases, the morphologies quantified in Fig. 4.7 appear to have converged by $t > 2 \times 10^5$ ($t^{1/3} > 58$).

Figure 4.8 shows late-time ISDs for the constant-mobility, dissimilar-mobility PS IC, and dissimilar-mobility RN IC 3-D cases, time-averaged over the interval $2 \times 10^5 < t \leq 4 \times 10^5$. All three ISDs are concentrated around the line of zero mean curvature, $H = (\kappa_1 + \kappa_2)/2 = 0$, which is indicated by a dashed line extending from the origin to the upper left corner. All cases have average scaled mean curvature $\langle H/S_V \rangle = 0.00$. However, the dissimilar-mobility ISDs are broader than the constant-mobility ISD, having a larger standard deviation of scaled mean curvature, $\sigma_{H/S_V} = 0.37$ vs. $\sigma_{H/S_V} = 0.32$.

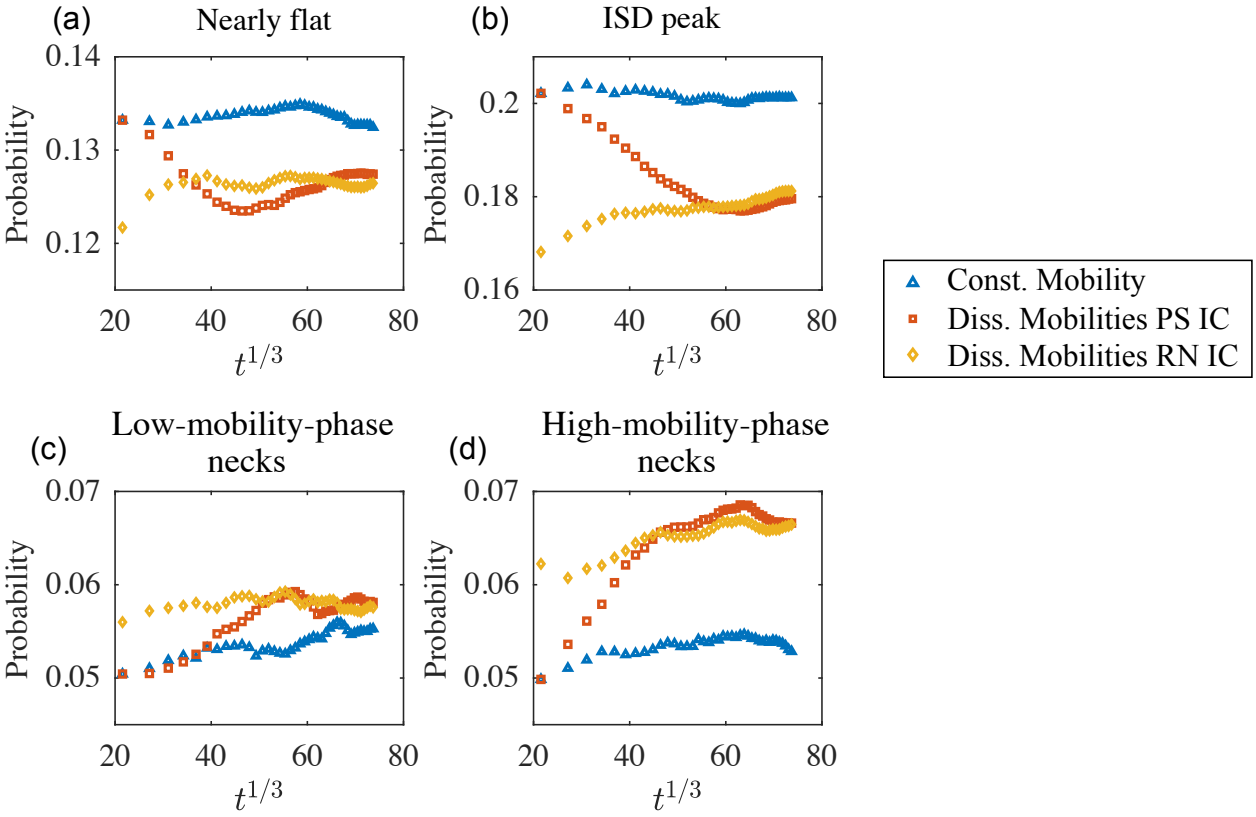

Figure 4.7: Time evolution of the integrated probability (i.e., the area fraction) of the four types of interfacial shape identified in Fig. 4.6 for the three 3-D simulations performed: constant mobility (blue triangles), dissimilar mobilities with phase separated initial condition (red squares), and dissimilar mobilities with random noise initial condition (yellow diamonds).

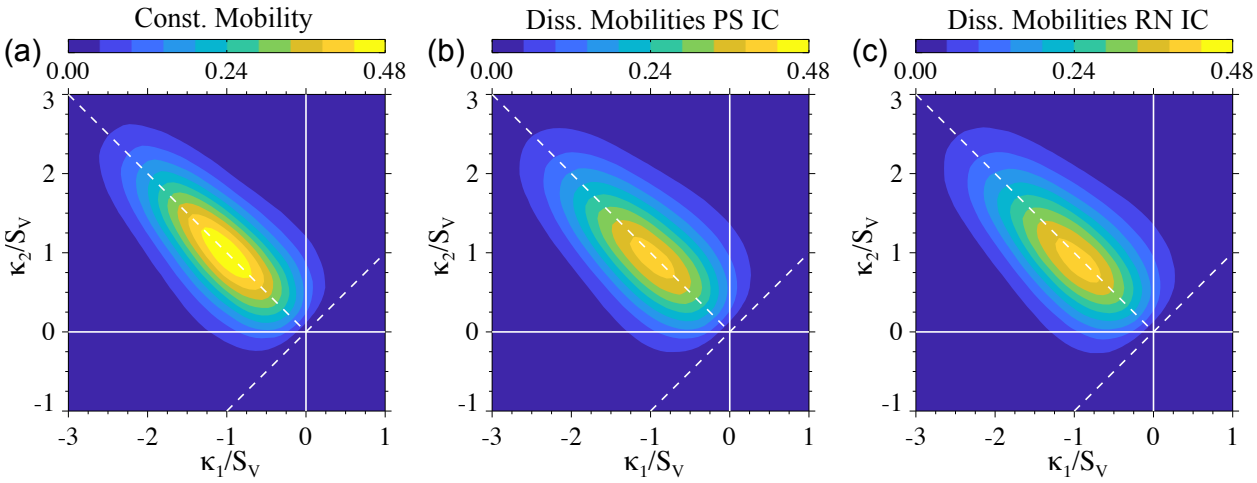

Figure 4.8: Late-time ISDs for the (a) constant mobility, (b) dissimilar mobilities with phase separated initial condition, and (c) dissimilar mobilities with random noise initial condition, time-averaged over the interval $2 \times 10^5 < t \leq 4 \times 10^5$.

As was inferred in Fig. 4.7c and 4.7d, the dissimilar-mobility ISDs in Fig. 4.8b and 4.8c are slightly asymmetric, with more area corresponding to high-mobility-phase necks than to low-mobility-phase necks. This asymmetry originates from the asymmetry in kinetics of coarsening of the two populations of necks. Low-mobility-phase necks are surrounded by high-mobility phase, and they disappear more rapidly than necks containing the high-mobility phase surrounded by the low-mobility phase [120, 121]. High-mobility-phase necks disappear more slowly, and therefore become more prevalent in the structure compared to low-mobility-phase necks. However, unlike high-mobility-phase particles in the 2-D case, they can still evolve away through the diffusion within the neck region. Thus, the structure does appear to reach a bicontinuous steady state, unlike the 2-D dissimilar-mobility case.

4.5.2 Kinetics

Coarsening kinetics of the 3-D structures are illustrated in Fig. 4.9, which shows the cube of characteristic length, S_V^{-3}, vs. time for each simulation alongside linear fits. The dissimilar-mobility conditions have very similar coarsening rates, with equations of fit $S_V^{-3} = 0.112t - 191$ for PS IC and $S_V^{-3} = 0.111t + 905$ for RN IC, while the constant-mobility case coarsens more quickly, with

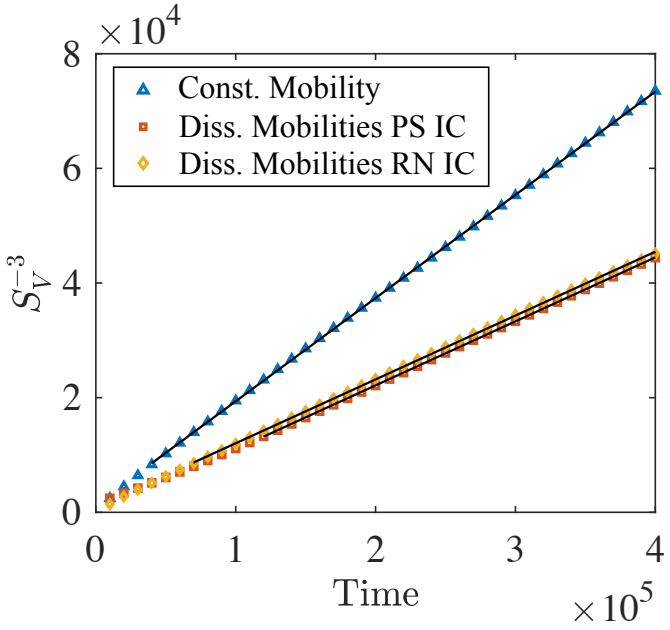

Figure 4.9: Coarsening kinetics for the 3-D structures. The cube of the characteristic length, S_V^{-3}, is plotted vs. time for the three simulations: constant mobility (blue triangles), dissimilar mobilities with phase separated initial condition (red squares), and dissimilar mobilities with random noise initial condition (yellow diamonds). Linear fits are shown as solid black lines.

$S_V^{-3} = 0.180t + 905$. The coarsening rate constant for the constant-mobility case (the coefficient of t in the fit) is in reasonable agreement with a literature value [55] of 0.173 after rescaling as described in Section 3.4. All cases produce excellent fits, with $R^2 = 0.99998$ and $R^2 = 0.99986$ for the dissimilar-mobility PS IC and RN IC cases, respectively, and $R^2 = 0.99996$ for the constant mobility case.

Transient coarsening kinetics are observed in Fig. 4.9 prior to steady-state. In the constant-mobility case, the rate of change of S_V^{-3} (i.e., the instantaneous coarsening rate constant, dS_V^{-3}/dt) decreases as it approaches steady state. The instantaneous coarsening rate constant of the dissimilar-mobility PS IC structure increases over time while that of the dissimlar-mobility RN IC structure decreases, resulting in a crossover of their S_V^{-3} vs. time plots in Fig. 4.9 near $t = 4 \times 10^4$.

4.5.3 Convergence of ISDs

Convergence of the time-dependent ISDs, denoted by $P(t)$ to the average ISDs, denoted by $\bar{P}$, is depicted in Fig. 4.10, which plots the L^1 norm of the difference $P(t) - \bar{P}$ vs. time. This quantity, $||P(t) - \bar{P}||_1$, is the integral of the absolute difference $|P(t) - \bar{P}|$ over the domain of the ISD. Differences between ISDs are sensitive to ISD resolution, which was $\Delta\kappa_1/S_V = \Delta\kappa_2/S_V = 0.08$ in this paper. Since the integrals of the ISDs themselves are unity (because of the normalization in Eq. 3.19), this measure of difference requires no additional normalization. In all cases shown in Fig. S1, $||P(t) - \bar{P}||_1$ has converged to small, stable values $(0.02 - 0.03)$ before $t^{1/3} = 58$, indicating that the average ISDs are representative of the converged, self-similar morphologies.

These values of $||P(t) - \bar{P}||_1$ during the converged regime provide an estimate of the uncertainty of our ISDs, which can be used to assess the statistical significance of the differences between ISDs for different conditions. The L^1-normed difference between dissimilar-mobility ISDs is 0.019, and the L^1-normed difference between either of them and the constant-mobility ISD is 0.135. The time-averaged dissimilar-mobility structures are therefore statistically indistinguishable, and they differ significantly from the constant-mobility structure. The values of $||P(t) - \bar{P}||_1$ during the converged regime can also be used to assess when the structure has converged. In Fig. 4.9, kinetics were fitted over a timescale determined by the ad hoc criterion $||P(t) - \bar{P}||_1 \leq 0.030$.

4.5.4 Application of geometrically general model

The coarsening dynamics of the 3-D structures can be interpreted using a theoretical model by DeHoff [52]. In his work, coarsening is modeled through the diffusional interactions of pairs of interfaces, referred to as communicating neighbors, over some interaction distance λ. The normal velocity of a surface element with mean curvature H and communicating with a neighbor element with mean curvature H_n is given by

$$v_n = K_D \frac{1}{\lambda} (H_n - H) \tag{4.4}$$

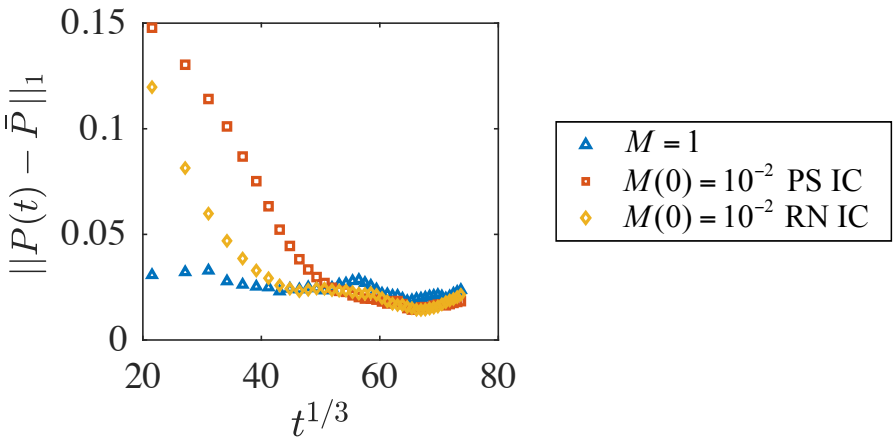

Figure 4.10: Plot of $||P(t) - \bar{P}||_1$ vs. $t^{1/3}$ illustrating convergence of ISDs for the 3-D cases: constant mobility (blue triangles), dissimilar mobilities with phase separated initial condition (red squares), and dissimilar mobilities with random noise initial condition (yellow diamonds).

where the kinetic coefficient K_D is $2M\gamma$ for the phase field model defined by Eqs. 3.4 and 3.5. This velocity results from a diffusive flux driven by the difference in curvature between the surface element and its neighbor element. To obtain a relationship between rate of change of total area, dA/dt, and the morphology, DeHoff used Eq. 4.4 with two additional assumptions: that volume fraction is constant, and that λ, H, and H_n are all uncorrelated. The resulting relationship can be written as

$$\frac{dA}{dt} = -2K_D \left\langle \frac{1}{\lambda} \right\rangle A\sigma_H^2, \tag{4.5}$$

where σ_H^2 is the variance of mean curvature, $\sigma_H^2 = \langle H^2 \rangle - \langle H \rangle^2$, and the brackets denote an area-weighted average over the interfaces.

The rate of change of total area is related to the instantaneous coarsening rate constant of our system, $k(t) = dS_V^{-3}/dt$, by

$$\frac{dS_V^{-3}}{dt} = -3S_V^{-3}\frac{1}{A}\frac{dA}{dt}. \tag{4.6}$$

Substituting DeHoff's relationship, Eq. 4.4, for dA/dt and scaling morphological quantities by S_V^{-1} yields

$$\frac{dS_V^{-3}}{dt} = 6K_D\frac{\sigma_{H/S_V}^2}{\hat{\lambda}}, \tag{4.7}$$

where $\hat{\lambda} = S_V^{-1} \langle 1/\lambda \rangle^{-1}$. Eq. 4.7 relates the coarsening rate constant to the scaled morphology with a single unknown parameter, the scaled average interaction distance $\hat{\lambda}$. For determination of this parameter in our systems, we note that Eq. 4.7 is formulated for diffusion through a single phase. This is a reasonable assumption for the dissimilar-mobility cases, as we can neglect transport through the low-mobility phase. For a bicontinuous structure with constant mobility, fluxes through each phase should contribute equally to the interfacial velocity, and we should have double the coarsening rate as compared to Eq. 4.7. This can be expressed by

$$\frac{dS_V^{-3}}{dt} = 6NK_D \frac{\sigma_{H/S_V}^2}{\hat{\lambda}}, \tag{4.8}$$

where N denotes the number of phases (one or two) with fluxes that contribute to the interfacial velocity.

To examine the relationship presented in Eq. 4.8, $(dS_V^{-3}/dt)/N$ is plotted against σ_{H/S_V}^2 in Fig. 4.11 for the three 3-D simulations. The coarsening rate constants are calculated from the data in Fig. 4.9 by a centered difference between output steps, i.e., $k(t_{n+1/2}) = [S_V^{-3}(t_{n+1}) - S_V^{-3}(t_n)]/(t_{n+1} - t_n)$, where t_n is the time of the nth output step. The variance in scaled curvature σ_{H/S_V}^2 was calculated at $t_{n+1/2}$ by a simple average. The earliest data points (calculated between $t = 10^4$ and $t = 2 \times 10^4$) are circled, and the final data points (calculated between $t = 3.9 \times 10^5$ and $t = 4 \times 10^5$) are noted by black symbols. A single fit to Eq. 4.8 using all of the data is shown as a solid black line.

In the 3-D constant-mobility case, σ_{H/S_V}^2 is nearly constant throughout the evolution, and $\hat{\lambda}$ was found to be 0.44 when Eq. 4.8 was fitted only to this data set. The two 3-D dissimilar-mobility cases, PS IC and RN IC, have similar trends, and when Eq. 4.8 is fit to the dissimilar-mobility datasets we obtain $\hat{\lambda} = 0.48$. Therefore, the primary difference in kinetics due to highly dissimilar mobilities can be interpreted as a factor of two decrease (due to the negligible contribution of the low-mobility phase). Furthermore, it appears that higher morphological driving force (σ_{H/S_V}^2) does indeed increase the coarsening rate constant. This is most apparent in the case where dissimilar-

mobility simulation was initialized with the constant-mobility phase separation morphology (the PS IC case). The simulation data for this case begins close to the cluster of points from the constant-mobility case, where the structure has comparatively smaller σ^2_{H/S_V} than its final state, and the instantaneous rate constant is smaller than its counterpart that was initialized with random noise (RN IC). As σ^2_{H/S_V} increases, the rate constant increases, eventually reaching the cluster of values from the RN IC simulation. Eq. 4.8 also appears to hold for the early stage of the RN IC simulation, where the structure resulting from the random noise initial condition has a distribution in H than the self-similar structure (see the circled yellow triangle in Fig. 4.11). Additional constant-mobility simulations demonstrating this relationship are provided in Section 8.1.

There are also changes in kinetics that cannot be explained by the evolution of σ^2_{H/S_V}. In both of the simulations that evolve with the same dynamics from random noise (constant mobility and dissimilar mobilities RN IC), there is a decrease in dS_V^{-3}/dt at early times. In the constant-mobility simulation, there is no change in σ^2_{H/S_V} to explain the decrease in dS_V^{-3}/dt, and in the dissimilar-mobility RN IC simulation, the change in dS_V^{-3}/dt is larger than predicted by the fit (the solid black line in Fig. 4.11) for its change in σ^2_{H/S_V} . These decreases in dS_V^{-3}/dt could be interpreted in the model as an increase in the average interaction distance $\hat{\lambda}$ in Eq. 4.8. However, as a property of the diffusion field, $\hat{\lambda}$ is difficult to assess independently, and therefore other morphological or kinetic effects cannot be ruled out.

4.6 Conclusions

Coarsening of a two-phase system in which the phases had dissimilar mobilities was studied at 50% volume fraction. Simulations were conducted in two and three dimensions using the Cahn-Hilliard model with a concentration-dependent mobility formulated to reduce the effect of small deviations in concentration, such as those due to the Gibbs-Thomson effect. Simulations with constant mobility were conducted for comparison. The simulated morphologies were characterized by the characteristic length, statistics of mean curvature, and the interfacial shape distribution

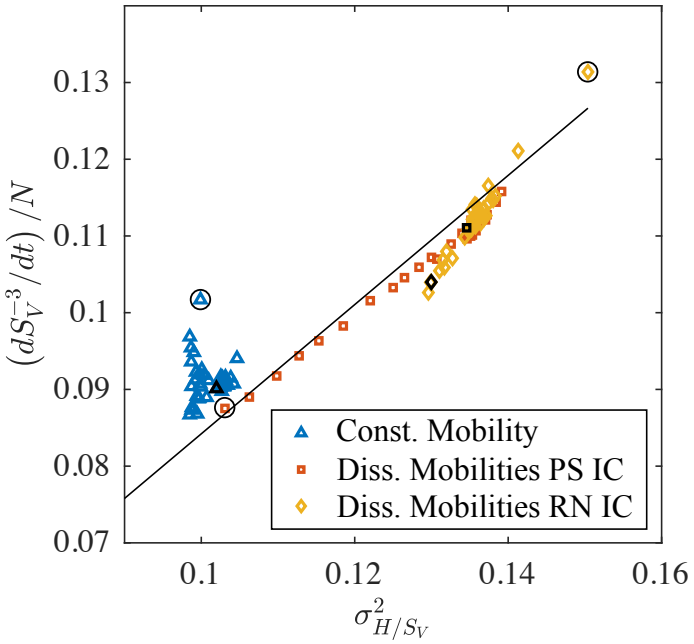

Figure 4.11: Plot of $(dS_V^{-3}/dt)/N$, the instantaneous coarsening rate constant per number of phases with contributing fluxes, vs. the variance of scaled mean curvature, σ^2_{H/S_V}, for the 3-D simulations: constant mobility (blue triangles), dissimilar mobilities with phase separated initial condition (red squares), and dissimilar mobilities with random noise initial condition (yellow diamonds). A fit of Eq. 4.8 to all three data sets is indicated by a solid black line. The earliest data points (calculated between $t = 10^4$ and $t = 2 \times 10^4$) are circled, and the final data points (calculated between $t = 3.9 \times 10^5$ and $t = 4 \times 10^5$) are noted by black symbols.

(ISD). Quantitative analysis of the ISD was applied to the 3-D simulation results.

A morphological transition during coarsening was identified in two dimensions when the mobility was dissimilar, which was not observed when the mobility was constant. In this transition, an initially layered structure transforms into a system of high-mobility-phase particles embedded in a low-mobility matrix. This morphological transition resulted in a decrease of the coarsening rate constant over time, which explains why previous studies [109, 110] did not find agreement with the $L \propto t^{1/3}$ power law but rather suggested smaller coarsening exponents. Morphological evolution was also observed in the 2-D constant-mobility case, and its kinetics agreed with the $t^{1/3}$ power law after an initial transient stage.

The 3-D simulations resulted in bicontinuous morphologies that evolved self-similarly. Close agreement was found between the late-time morphologies of two dissimilar-mobility simulations that differed only in their initial conditions. The self-similar morphology for the dissimilar-mobility cases has greater variance in scaled mean curvature than the constant-mobility morphology. The dissimilar-mobility morphology also possesses slight asymmetry caused by the asymmetry in mobility: it contains more area corresponding to necks surrounded by low-mobility phase, which evolve more slowly, than area corresponding to necks surrounded by high-mobility phase, which evolve more quickly.

Based on theory and simulations, the primary difference in the kinetics of coarsening between the dissimilar-mobility and constant mobility systems were determined to be a factor of two smaller kinetic coefficient in the dissimilar-mobility case due to the lack of diffusion in one of the phases. The coarsening kinetics of the 3-D cases agreed well with the theoretical $t^{1/3}$ power law after initial transient stages. The transient coarsening kinetics in the 3-D simulations were observed to match a theoretical prediction by DeHoff [52] that related the variance in scaled curvature, σ^2_{H/S_V}, to the instantaneous coarsening rate constant, $k = dS_V^{-3}/dt$, calculated between simulation output step). DeHoff's theory assumes that the distances of diffusional interactions between neighboring interfaces are uncorrelated to the curvatures of the interfaces. Applying this theory to the coarsening of bicontinuous structures, we obtained similar scaled average diffusional interaction distances for

the constant- and dissimilar-mobility cases. The resulting expression for the instantaneous kinetic coefficient provides a practical analytical model for materials engineering, as well as fundamental understanding, of the coarsening phenomena that is ubiquitous in a broad range of materials systems. Additional simulation evidence in support of this model is presented in Section 8.1.

Chapter 5

Coarsening of bicontinuous microstructures via surface diffusion

5.1 Introduction

Surface diffusion is thought to be the mechanism for coarsening in nanoporous metallic structures [11, 16, 22, 78]. These nanostructures are of technological interest due to their tunable mechanical properties [19, 20, 122, 123] and functional applications including catalysis [15, 16], actuation [124], sensing [18], and electrochemical supercapacitors [17]. Performance in all of these applications is dependent on the length scale of the nanostructures, which increases during coarsening. Coarsening therefore represents both a method for tuning properties and a challenge to be overcome for engineering applications [11].

Nanoporous metallic structures are typically created by electrochemical dealloying [11, 13], in which the less noble element of the alloy is removed and a porous structure (composed of the more noble element) remains. Electrochemical dealloying can be driven by an applied potential or it can occur via free corrosion, where the alloy is in contact with an electrolyte without an applied potential [123]. Since antiquity, electrochemical dealloying has been used to produce nanoporous gold leaf from Au-Ag alloys [14]. Nanoporous gold continues to be the most widely studied system produced by electrochemical dealloying [15, 16, 17, 18, 19, 20, 22, 78, 122, 123, 124], although nanostructures composed of Ni [125], Pt [126], and other noble elements [127] have also been

fabricated.

Experimental studies of coarsening in nanoporous gold [16, 22, 128] indicate that characteristic length scales evolve according to the $t^{1/4}$ power law for surface diffusion, as discussed in Chapter 2. Recent work also indicates that evolution of nanoporous gold during coarsening may be self-similar [21]. However, little is known theoretically about coarsening via surface diffusion beyond the power law. There is no analytical theory that can predict the self-similar morphology. Simulations are therefore necessary, but they have yet to result in predictions of self-similar morphologies in three dimensions (3D).

Several studies have examined coarsening via surface diffusion in two dimensions using continuum [77, 100, 105, 106, 109, 110, 129, 130] and atomistic- or molecular-scale kinetic Monte Carlo [77, 130] methods, but only one kinetic Monte Carlo study [78] has examined a three-dimensional (3-D) system. This 3-D study [78] investigated coarsening within individual nanoporous nanoparticles. Self-similar coarsening was not observed in the study, as the particles densified over time to reduce the area of their external surface (the surface composed of the outer boundary of the particle, as opposed to the surface within the porous structure), eventually consisting of nearly 100% solid phase. Simulations that have observed self-similar coarsening via bulk diffusion [53, 54, 55] have relied upon large sample microstructures with periodic boundary conditions that avoid the effect of an external surface. We adopt this approach to study coarsening via surface diffusion. The results show that the self-similar states exist, and we characterize differences in self-similar morphology between structures that coarsen via surface and via bulk diffusion.

The evolution of a surface by interfacial-energy-driven surface diffusion was first described at the continuum scale by Mullins [79, 131], and was introduced in Eq. 2.41 in Chapter 2. As evident in the governing equation (Eq. 2.41), namely

$$v_n = -\eta \nabla_s^2 H, \tag{5.1}$$

evolution via surface diffusion is fully specified by the local geometry of the surface. Correspon-

dence between this sharp interface model and a phase field model was first demonstrated by Cahn et al. [132]. They examined a modified Cahn-Hilliard model for spinodal decomposition in a deeply quenched system. In this system, mobility is concentration-dependent and zero in both phases at their equilibrium compositions. Two types of bulk free energy $f(\phi)$ were considered, the double-obstacle potential [133], depicted in Fig. 5.1a, and the low-temperature limit of a regular solution model,

$$f(\phi) = \tilde{T}\left[\phi \ln \phi + (1-\phi)\ln(1-\phi)\right] + \phi(1-\phi), \tag{5.2}$$

where $\tilde{T}$ is the scaled temperature. The low temperature limit $\tilde{T} \to 0$ corresponds to $\phi_0^+ \to 1$ and $\phi_0^- \to 0$. It also corresponds to $f''(\phi_0^\pm) \to \infty$. The effect of this limit is elucidated by Eq. 2.33, which we restate here in terms of the order parameter ϕ,

$$\Delta\phi = -\frac{2\gamma H}{(\phi_0^+ - \phi_0^-) f''(\phi_0^\pm)}. \tag{5.3}$$

The low-temperature limit therefore results in $\Delta\phi \to 0$, i.e., asymptotically small changes in bulk concentration. The double-obstacle potential has $\Delta\phi = 0$, i.e., constant bulk concentration, although Eq. 5.3 is no longer valid because $f(\phi)$ is no longer smooth [133]. Considering the physical two-phase, two-component system, these bulk free energies eliminate the solubility of the non-majority component in each bulk phase. Deviations from the bulk equilibrium concentrations are therefore asymptotically small or zero in the regular solution and double-obstacle cases, respectively, and the concentration-dependent mobility is therefore asymptotically small or zero. Zero mobility in the bulk suppresses bulk diffusion and leaves surface diffusion (i.e., Eq. 2.41) as the only transport mechanism in the system.

Many subsequent authors [100, 105, 106, 109, 110, 134, 135] have employed the double-well potential (Fig. 5.1b) for the bulk free energy instead of the double-obstacle potential (Fig. 5.1a) or regular solution model. The double-well potential permits solubility in the bulk phases, which can allow some bulk diffusion to occur even if the mobility is set to zero at the equilibrium compositions of the phases [116, 117, 118]. Diffusion through the bulk can be eliminated by a modification

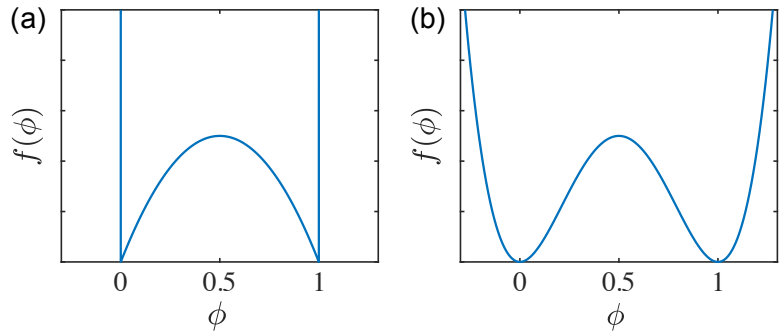

Figure 5.1: Possible forms of bulk free energy function $f(\phi)$ for use in phase field models for surface diffusion: (a) the double-obstacle potential, $f(\phi) \propto |\phi(1-\phi)|$ for $\phi \in [0,1]$, $f(\phi) = \infty$ otherwise, and (b) the double-well potential, $f(\phi) \propto \phi^2(\phi-1)^2$.

to the chemical potential proposed by Rätz, Ribalta, and Voigt (RRV) [136]. The modified chemical potential in the RRV model is non-variational; it no longer represents the variational derivative of the free energy functional (Eq. 3.1) with respect to the order parameter. Using the variational derivative as the chemical potential guarantees that the free energy functional is monotonically decreasing [131], and it is not known whether this is the case for the RRV model. However, asymptotic analyses of the RRV model show that it corresponds to interfacial-energy-driven surface diffusion (Eq. 2.41), and numerical agreement between the phase field and sharp interface models has been demonstrated [136, 137]. We therefore adopt the RRV model to study coarsening of bicontinuous microstructure via surface diffusion.

5.2 Phase field model

We now describe the RRV model as it is employed in this study. Specifically, we consider a system with isotropic interfacial energy and in the limit of fast attachment kinetics (i.e., kinetics that are surface-diffusion limited, rather than attachment-rate limited). To ensure that ϕ is constant in the bulk, the RRV model modifies the Cahn-Hilliard equation, Eq. 3.4, by dividing the chemical potential by a stabilizing function, $g(\phi) \propto f(\phi)$,

$$\frac{\partial \phi}{\partial t} = \nabla \cdot M(\phi) \nabla \frac{1}{g(\phi)} \left[f'(\phi) - \varepsilon^2 \nabla^2 \phi \right], \tag{5.4}$$

The RRV model also uses a concentration-dependent mobility of the form $M(\phi) \propto f(\phi)$, which is zero at the equilibrium concentrations, $M(\phi_0^{\pm}) = 0$.

The sharp interface dynamics of this model was analyzed in Refs. [136, 137]. The shape of the diffuse interface at leading order is unchanged by $g(\phi)$, since it results from a balance of the terms of μ (i.e., setting $\mu = 0$ in Eq. 3.2). The stabilizing function causes higher-order changes to the chemical potential at the interface (e.g., due to the Gibbs-Thomson effect) to vanish away from the interface. The phases therefore have no driving force to change from the bulk equilibrium values of ϕ, and the mobility is zero throughout the bulk.

Following the analysis of Rätz et al. [136], the sharp interface kinetic coefficient α can be determined in terms of the phase field model parameters. This relationship can be expressed as

$$\alpha = \frac{\varepsilon}{(\phi_0^+ - \phi_0^-)} \int_{\phi_0^-}^{\phi_0^+} \frac{M(\phi)}{\sqrt{2f(\phi)}} d\phi \frac{\gamma}{\int_{\phi_0^-}^{\phi_0^+} g(\phi) d\phi}, \tag{5.5}$$

where γ, the interfacial energy, is given by Eq. 3.6

5.2.1 Simulation parameters

The RRV model consisting of Eqs. 3.2 and 5.4 was used to simulate phase separation and coarsening via surface diffusion. The bulk free energy was specified by Eq. 3.5, and the mobility and stabilizing function were chosen to be $M(\phi) = g(\phi) = \phi^2(1-\phi)^2$. Parameters of the phase field model were $W = 0.4$ and $\varepsilon^2 = 0.2$, which result in a sharp interface kinetic coefficient $\eta = 1/6$. Singularity of $1/g(\phi)$ was avoided by the addition of a small positive constant, $\sigma = 10^{-12}$, to the denominator: $1/g(\phi) \approx 1/[g(\phi) + \sigma]$.

This model was simulated in cubic domains, $L_x = L_y = L_z = 1024$, with periodic boundary conditions. The domain was discretized by a uniform Cartesian grid with $\Delta x = 1$, which resulted in 3-5 points through the interface. Eqs. 3.2 and 5.4 were solved numerically using finite differences. Explicit (forward Euler) timestepping was used with $\Delta t = 0.04$, and simulations were initialized with random noise.

5.3 Results

This section describes the results of simulations at two average system compositions, $\langle\phi\rangle = 0.50$ and $\langle\phi\rangle = 0.36$. Our discussion of the coarsening results focuses initially on the evolution of the scaled morphologies. Convergence to self-similar coarsening is demonstrated, and agreement with the $t^{1/4}$ power law is found during the self-similar regime. The self-similar structures are then characterized in greater detail using samples of the structures, statistics of morphology and topology, and interfacial shape distributions. The differences between surface- and bulk-diffusion morphologies are analyzed and discussed.

5.3.1 Evolution of scaled morphology and topology

Fig. 5.2 depicts the evolution of the moments of mean curvature and the scaled topology. Average scaled mean curvature $\langle H/S_V\rangle$, standard deviation of scaled mean curvature σ_{H/S_V}, and scaled genus density $g_V S_V^{-3}$ are plotted vs. characteristic length, which enables a direct comparison between the surface- and bulk-diffusion cases. In the structures with $\langle\phi\rangle = 0.50$, scaled genus density converges quickly, and the first and second moments of scaled mean curvature (Fig. 5.2a and 5.2b) undergo little, if any, evolution. This indicates that the morphologies resulting from phase separation are close to the self-similar coarsening morphologies. More substantial evolution is observed at $\langle\phi\rangle = 0.36$: for both coarsening mechanisms, the average and standard deviation of scaled mean curvature decrease, while scaled genus density increases. In all four cases, bulk and surface diffusion with $\langle\phi\rangle = 0.50$ and $\langle\phi\rangle = 0.36$, there is a late time (large S_V^{-1}) regime at which all of the quantities in Fig. 5.2 appear to be stable.

We focus on scaled genus density to quantify convergence to the stable state, since all four cases experience some genus density evolution. To quantify convergence, we examine the standard deviation of $g_V S_V^{-3}$ within an interval $[S_V^{-1}-5, S_V^{-1}+5]$, i.e., within a moving window $10S_V^{-1}$ wide. We denote this quantity $\sigma_g(S_V^{-1})$, and plot it vs. S_V^{-1} in Fig. 5.3a. Structures were considered converged for all S_V^{-1} greater than the S_V^{-1} at which σ_g initially drops below a critical value, $\sigma_g(S_V^{-1}) = 0.001$,

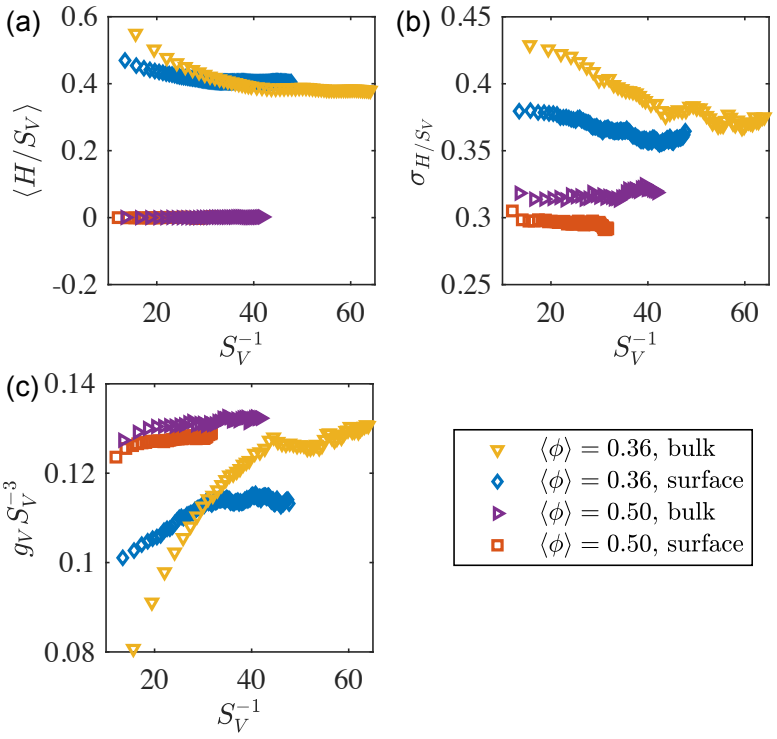

Figure 5.2: Quantitative evolution of the bulk- and surface-diffusion structures. (a) average scaled mean curvature $\langle H/S_V \rangle$, (b) standard deviation of scaled mean curvature σ_{H/S_V}, and (c) scaled genus density $g_V S_V^{-3}$ are plotted vs. the characteristic length S_V^{-1} for all four cases: bulk diffusion $\langle\phi\rangle = 0.36$ (yellow downward triangles), surface diffusion $\langle\phi\rangle = 0.36$ (blue diamonds), bulk diffusion $\langle\phi\rangle = 0.50$ (purple rightward triangles), and surface diffusion $\langle\phi\rangle = 0.50$ (red squares).

which is indicated by the dotted line in Fig. 5.3a. Based on this criterion, the surface-diffusion $\langle\phi\rangle = 0.50$ and $\langle\phi\rangle = 0.36$ structures converged by $S_V^{-1} = 19.1$ and $S_V^{-1} = 32.4$ respectively, while the bulk-diffusion $\langle\phi\rangle = 0.50$ and $\langle\phi\rangle = 0.36$ structures converged by $S_V^{-1} = 21.5$ and $S_V^{-1} = 46.7$. The converged (i.e., self-similar) regime of evolution then consists of all characteristic lengths available for each structure after its characteristic length of convergence.

To verify that the criterion $\sigma_g(S_V^{-1}) \leq 0.001$ adequately represents convergence of the morphology, we plot convergence of ISDs in Fig. 5.3b. For each structure, the ISD was averaged in S_V^{-1} over the self-similar regime, and the average ISDs are denoted by $\bar{P}(\kappa_1/S_V, \kappa_2/S_V)$, in contrast to the time-dependent ISDs $P(\kappa_1/S_V, \kappa_2/S_V; t)$. Fig. 5.3b plots the integrated absolute difference between $P(t)$ and $\bar{P}$ (i.e., the L^1 normed difference $||\bar{P} - P(t)||_1$) vs. characteristic length. This difference is always small for the $\langle\phi\rangle = 0.50$ cases, which is consistent with the minimal evolution of $\langle H/S_V\rangle$ and σ_{H/S_V} in Fig. 5.2. For the $\langle\phi\rangle = 0.36$ cases, the difference $||\bar{P} - P(t)||_1$ decreases substantially during coarsening to low, stable values, indicating convergence of the ISD. We note that the integral of the absolute value of an ISD (i.e., its L^1 norm $||P||_1$) is equal to unity, as it is a probability density function. Thus, the difference $||\bar{P} - P(t)||_1$ is already a relative difference with respect to either ISD. For example, $\bar{P}$ for bulk diffusion with $\langle\phi\rangle = 0.36$ differs by 40% from $P(t)$ at the earliest available time.

Across all cases, $||\bar{P} - P(t)||_1$ appears to increase slowly with S_V^{-1} after convergence. This could correspond to slow, long-term evolution of the ISD, but we note that increasing S_V^{-1} decreases in the size of the statistical sample (i.e., the total interfacial area) used to generate the ISDs. With less area binned at the same ISD resolution ($\kappa_1/S_V = \kappa_2/S_V = 0.125$), the ISD begins to contain more noise. To demonstrate this effect, the differences $P(t) - \bar{P}$ are plotted in Fig. 5.4 in the middle of the self-similar regime for each case (i.e., the midpoint of the self-similar interval in S_V^{-1}). In Fig. 5.4, the magnitude of $P(t) - \bar{P}$ increases from Fig. 5.4a to Fig. 5.4d, matching the increase in S_V^{-1}. The larger differences present at higher S_V^{-1} appear to be uncorrelated: they change rapidly in sign, especially near the peak. Thus, much of the differences $||\bar{P} - P(t)||_1$ in Fig. 5.3b are attributable to noise, and the total amount of evolution during the self-similar regime is likely to be

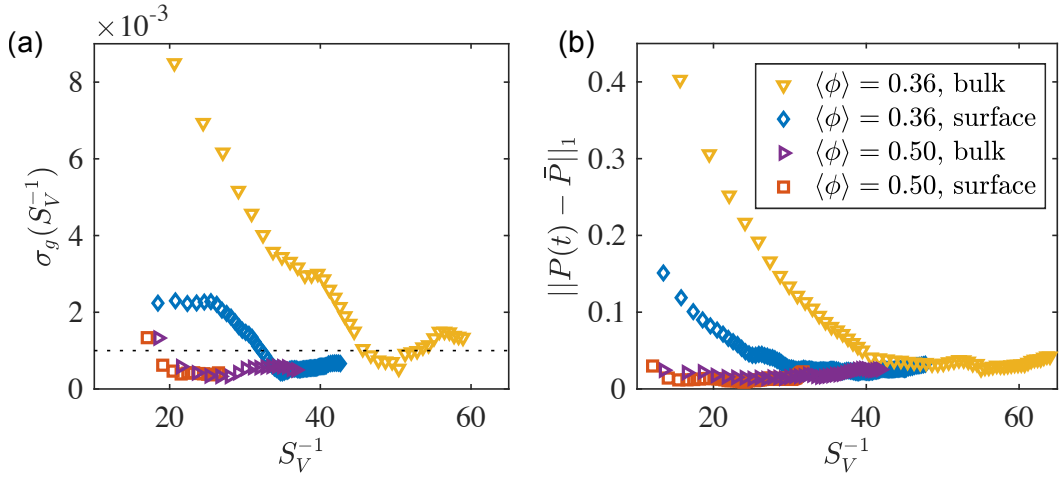

Figure 5.3: Measures of convergence of (a) the scaled genus density and (b) the scaled ISD, both plotted vs. characteristic length. In (a), the quantity $\sigma_g(S_V^{-1})$ represents the standard deviation of $g_V S_V^{-3}$ within an interval centered at S_V^{-1}. The critical value of σ_g used to assess convergence, 0.001, is indicated as a dotted line. In (b) quantity $||P(t)-\bar{P}||_1$ is the integrated absolute difference (i.e., the L^1 normed difference) between a self-similar average ISD $\bar{P}$ and the time-dependent ISD $P(t)$. All four conditions are shown in (a) and (b): bulk diffusion $\langle\phi\rangle = 0.36$ (yellow downward triangles), surface diffusion $\langle\phi\rangle = 0.36$ (blue diamonds), bulk diffusion $\langle\phi\rangle = 0.50$ (purple rightward triangles), and surface diffusion $\langle\phi\rangle = 0.50$ (red squares).

even less than that quantified by $||\bar{P}-P(t)||_1$. Regardless of their source, the values of $||\bar{P}-P(t)||_1$ after convergence can be interpreted as a measure of uncertainty of the ISDs. For the $\langle\phi\rangle = 0.50$ structures, they are in the range $0.01-0.03$, and for the $\langle\phi\rangle = 0.36$ structures, they are in the range $0.02-0.04$.

5.3.2 Kinetics

As discussed above, the simulation results provide evidence that all of the structures converge to a self-similar state, where scaled morphological and topological statistics are constant. During self-similar coarsening via surface diffusion (Eq. 2.41), the time evolution of the characteristic length S_V^{-1} must follow the $t^{1/4}$ power law, which can be expressed as

$$S_V^{-4}(t) - S_V^{-4}(0) = kt, \tag{5.6}$$

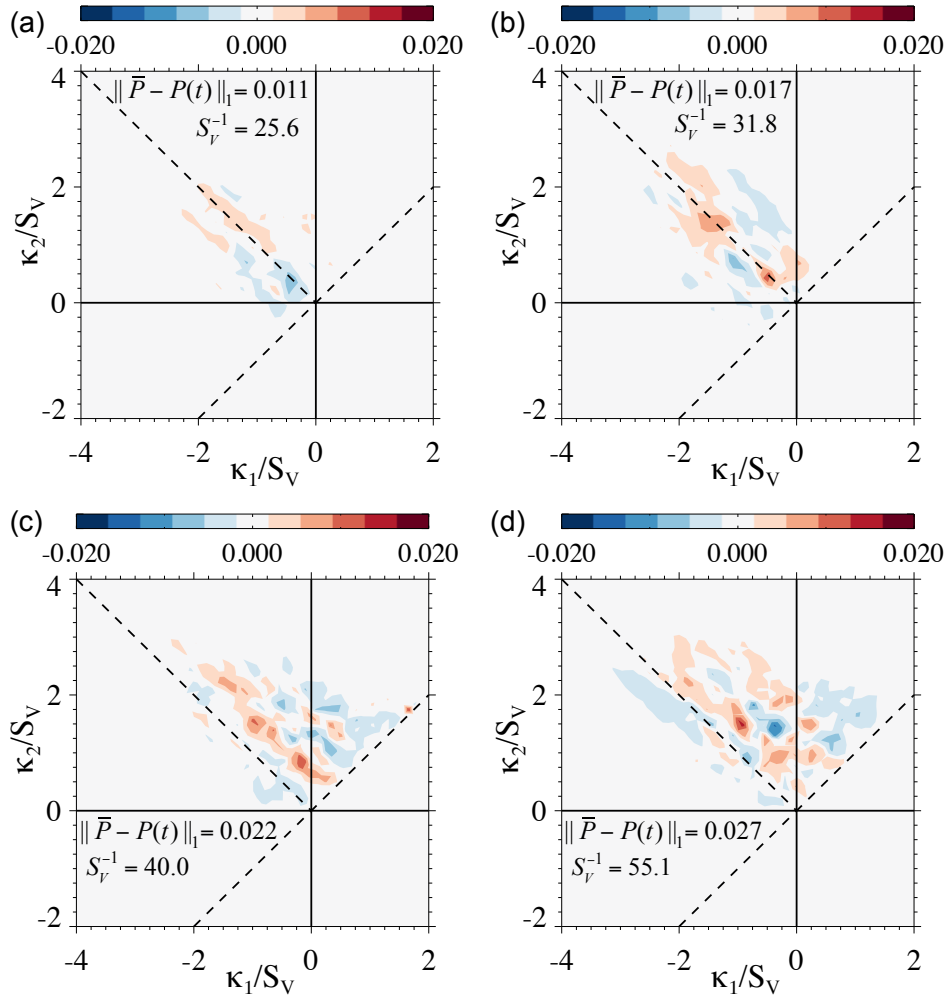

Figure 5.4: Differences between time-averaged and time-dependent ISDs, $P(t) - \bar{P}$, for each condition in the middle of its self-similar regime: (a) surface diffusion, $\langle \phi \rangle = 0.50$, (b) bulk diffusion, $\langle \phi \rangle = 0.50$, (c) surface diffusion, $\langle \phi \rangle = 0.36$, and (d) bulk diffusion, $\langle \phi \rangle = 0.36$.

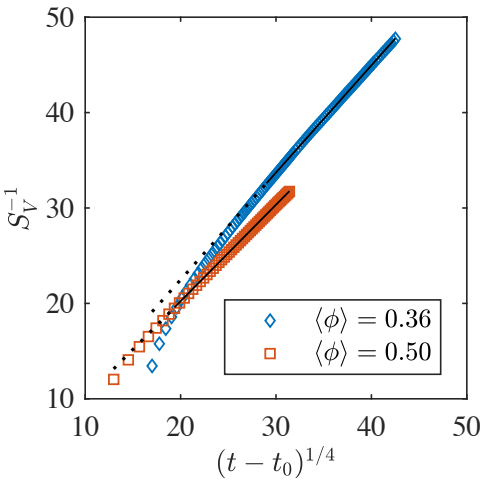

Figure 5.5: Kinetics of coarsening for both surface-diffusion cases, $\langle\phi\rangle = 0.36$ (blue diamonds) and $\langle\phi\rangle = 0.50$ (red squares). Characteristic length S_V^{-1} is plotted vs. the translated time $(t-t_0)^{1/4}$. Fits to Eq. 5.6 within the self-similar regime are shown as solid black lines, and the dotted lines indicate extensions of the fits to earlier times, prior to convergence.

where k is the coarsening rate constant. The time evolution of S_V^{-1} is shown in Fig. 5.5 for the surface-diffusion simulations. Fits to Eq. 5.6 within the self-similar regime are shown as solid lines, and the dotted lines indicate extensions of the fits to earlier S_V^{-1}. The initial times t_0 in Fig. 5.5 were calculated by $t_0 = S_V^{-4}(0)/k$ for each case. Equations of fit were $S_V^{-4} = 1.59t + 1.08 \times 10^5$ for $\langle\phi\rangle = 0.36$ and $S_V^{-4} = 1.05t + 1.30 \times 10^4$ for $\langle\phi\rangle = 0.50$. The fits provided excellent agreement within the self-similar regime used for fitting: coefficients of correlation were $R^2 = 0.99986$ for $\langle\phi\rangle = 0.36$ and $R^2 = 0.99998$ for $\langle\phi\rangle = 0.50$. Prior to the self-similar regime, transient kinetics are observed: the coarsening rate constant decreases over time to its self-similar value. This decrease is more substantial for the $\langle\phi\rangle = 0.36$ case, which correlates to its longer and more substantial evolution prior to convergence.

5.3.3 Self-similar morphologies

In this section, we examine the self-similar morphologies that result from surface diffusion and compare them to the bulk-diffusion cases.

Structures

Fig. 5.6 shows samples of the surface-diffusion structures from the latest available times with the same scaled volume, $(8S_V^{-1})^3$. The $\langle\phi\rangle = 0.50$ case at $t = 9.6 \times 10^5$ is shown in Figs. 5.6a-c, and the $\langle\phi\rangle = 0.36$ case at $t = 3.2 \times 10^6$ is shown in Figs. 5.6d-f. The interfaces (i.e., the $\phi = 0.50$ isosurfaces) are depicted with the $\phi = 1$ phase capped at the sample boundary in Figs. 5.6a and 5.6d, colored by scaled mean curvature H/S_V in Figs. 5.6b and 5.6e, and colored by scaled Gaussian curvature K/S_V^2 in Figs. 5.6c and 5.6f.

The structures appear to be bicontinuous, and most notable high-curvature features are necks. These have highly negative Gaussian curvature and mean curvature of either sign, although necks with negative mean curvature are less common in the $\langle\phi\rangle = 0.36$ structure (Fig. 5.6e). Interfaces with negative Gaussian curvature are known as hyperbolic interfaces, and their principal curvatures κ_1 and κ_2 have opposite signs. Interfaces with positive Gaussian curvature are known as elliptic interfaces, and their principal curvatures have the same sign. More elliptic interfaces are visible in the $\langle\phi\rangle = 0.36$ structure than in the $\langle\phi\rangle = 0.50$ structure, but overall they are less common than hyperbolic interfaces.

Scaled topology and morphological statistics

Table 5.1 compares the average and standard deviation of scaled mean curvature ($\langle H/S_V\rangle$ and σ_{H/S_V}, respectively) and the scaled genus density $g_V S_V^{-3}$ of all four cases (surface- and bulk diffusion, $\langle\phi\rangle = 0.50$ and $\langle\phi\rangle = 0.36$) over the self-similar regime. The structures at $\langle\phi\rangle = 0.50$ are quantitatively similar: the surface-diffusion case has lower σ_{H/S_V} and slightly lower $g_V S_V^{-3}$, with no difference in $\langle H/S_V\rangle$. The $\langle\phi\rangle = 0.36$ cases differ more substantially: the surface-diffusion structure has lower $g_V S_V^{-3}$, lower σ_{H/S_V}, and higher $\langle H/S_V\rangle$.

Comparing the coarsening mechanisms, we find lower σ_{H/S_V} and $g_V S_V^{-3}$ for surface diffusion compared to bulk diffusion. The higher $\langle H/S_V\rangle$ observed in the surface-diffusion case at $\langle\phi\rangle = 0.36$ may also be general for non-symmetric bicontinuous mixtures, but at $\langle\phi\rangle = 0.50$ the symmetry between phases requires that $\langle H/S_V\rangle = 0.00$. Differences due to coarsening mechanism are smaller

Table 5.1: Average scaled mean curvature, standard deviation of scaled mean curvature, and scaled genus density of self-similar structures coarsening via surface and bulk diffusion.

	$\langle\phi\rangle = 0.50$		$\langle\phi\rangle = 0.36$	
	surface	bulk	surface	bulk
$\langle H/S_V \rangle$	0.00	0.00	0.41	0.38
σ_{H/S_V}	0.30	0.32	0.36	0.37
$g_V S_V^{-3}$	0.128	0.132	0.114	0.129

than the differences due to system composition, $\langle\phi\rangle$, except in the case of scaled topology, which was very similar between the bulk-diffusion structures at $\langle\phi\rangle = 0.50$ and $\langle\phi\rangle = 0.36$.

The contribution of independent particles to the scaled topology was also assessed. In the self-similar structures, two independent particles were observed in the $\langle\phi\rangle = 0.36$ surface-diffusion case, and none were observed in the other cases. These particles are a negligible component of the overall topology of the structure, which had at minimum $g = 1116$, and comprise a negligible fraction of the total volume, with $V_f < 10^{-4}$. The evolution observed in the $\langle\phi\rangle = 0.36$ surface-diffusion case is therefore representative of a bicontinuous structure.

Interfacial shape distributions

The self-similar average ISDs $\bar{P}(\kappa_1/S_V, \kappa_2/S_V)$ introduced in Section 5.3.1 are shown in Fig. 5.7. Figs. 5.7a-c depict the $\langle\phi\rangle = 0.50$ cases, while Figs. 5.7d-f depict the $\langle\phi\rangle = 0.36$ cases. The surface-diffusion ISDs are Figs. 5.7a and 5.7d, the bulk-diffusion ISDs are Figs. 5.7c and 5.7f, and Figs. 5.7b and 5.7e show the differences between them. The line $\kappa_1 = -\kappa_2$ corresponds to zero mean curvature ($H = 0$), and is indicated on the ISDs by a dashed line extending from the origin. The lines $\kappa_1 = 0$ and $\kappa_2 = 0$ correspond to zero Gaussian curvature ($K = 0$), where the interfacial shape corresponds to that of a cylinder. Hyperbolic interfaces lie in the quadrant $\kappa_1 < 0$, $\kappa_2 > 0$, and they comprise the majority of interfaces in all four ISDs. The $\langle\phi\rangle = 0.50$ ISDs are concentrated closely around the $H = 0$ line, while the $\langle\phi\rangle = 0.36$ ISDs are more diffuse, and are shifted toward the upper right (higher $H = (\kappa_1 + \kappa_2)/2$). This is consistent with the differences between structures in Fig. 5.6, where the $\langle\phi\rangle = 0.36$ structure (Fig. 5.6d) had substantially more areas with large positive scaled mean curvature than the $\langle\phi\rangle = 0.50$ structure (Fig. 5.6b). The

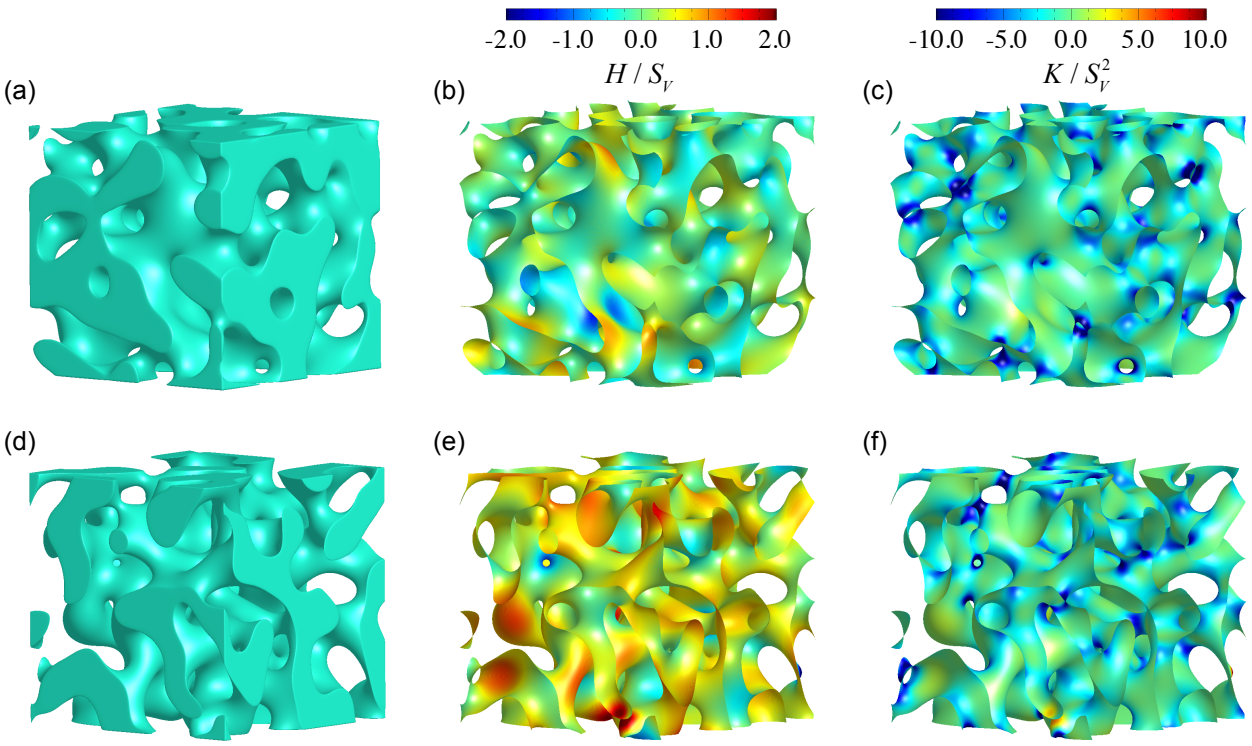

Figure 5.6: Samples of volume $(8S_V^{-1})^3$ of structures with (a) $\langle\phi\rangle = 0.50$ and (b) $\langle\phi\rangle = 0.36$ evolved via surface diffusion. The $\phi = 0.5$ isosurface is shown in (a,c) with the $\phi = 1$ phase capped at the domain boundary, in (b,d) colored by scaled mean curvature, and in (c,f) colored by scaled Gaussian curvature.

$\langle\phi\rangle = 0.36$ ISDs are more diffuse, which is consistent with their higher values of σ_{H/S_V} in Table 5.1.

At $\langle\phi\rangle = 0.50$, the difference between ISDs due to coarsening mechanism (Fig. 5.7b) is small. Quantitatively, $||P_{surf} - P_{bulk}||_1 = 0.04$, which is larger than their time-dependent uncertainties in Fig. 5.3 ($0.01 - 0.03$). The surface-diffusion ISD has more low-curvature area (i.e., near the origin), including more elliptic area, and its higher-curvature areas are more closely concentrated about the $H = 0$ line than in the bulk-diffusion ISD, which may result in its lower σ_{H/S_V} in Table 5.1.

The difference between surface- and bulk-diffusion ISDs at $\langle\phi\rangle = 0.36$ is shown in Fig. 5.7e. Quantitatively, $||P_{surf} - P_{bulk}||_1 = 0.09$, which is substantially larger than the variation in time of either ISD ($0.02 - 0.04$). The line $H/S_V = 0.38$, representing $\langle H/S_V\rangle$ of the bulk-diffusion case, has been drawn onto Fig. 5.7e as a dotted line. The surface-diffusion ISD contains more area to the upper right of this line (with higher H/S_V) and less area to the lower left of it (with lower H/S_V). Much of this increase in area at higher H/S_V corresponds to elliptic areas with $\kappa_1 > 0$, which correspond to 'caps' with positive K in Fig. 5.6. The decrease in area at lower H/S_V corresponds to hyperbolic interfaces with highly negative K, i.e., necks in Fig. 5.6. Both of these changes are expected to reduce $g_V S_V^{-3}$ because of the Gauss-Bonnet theorem (Eq. 3.23), matching the trend in Table 5.1. We note that changing a structure to contain more elliptic areas doesn't necessarily reduce its unscaled genus density, g/V, but it does decrease the size of the characteristic volume S_V^{-3} without increasing genus, thereby resulting in lower scaled genus density.

The differences in morphology due to coarsening mechanism will require additional theoretical developments to fully explain. One route to such an explanation would examine the topological changes that occur during coarsening. Since all of the structures have substantial genus density and a negligible number of particles, the dominant mechanism of topology change is the pinching-off of necks. This has been studied for surface diffusion [138, 139], and for bulk diffusion when the diffusivities of the phases are highly dissimilar [120, 121]. Since this process results in hyperbolic interfaces (necks) turning into elliptic areas (caps), the higher fraction of elliptic area in the surface

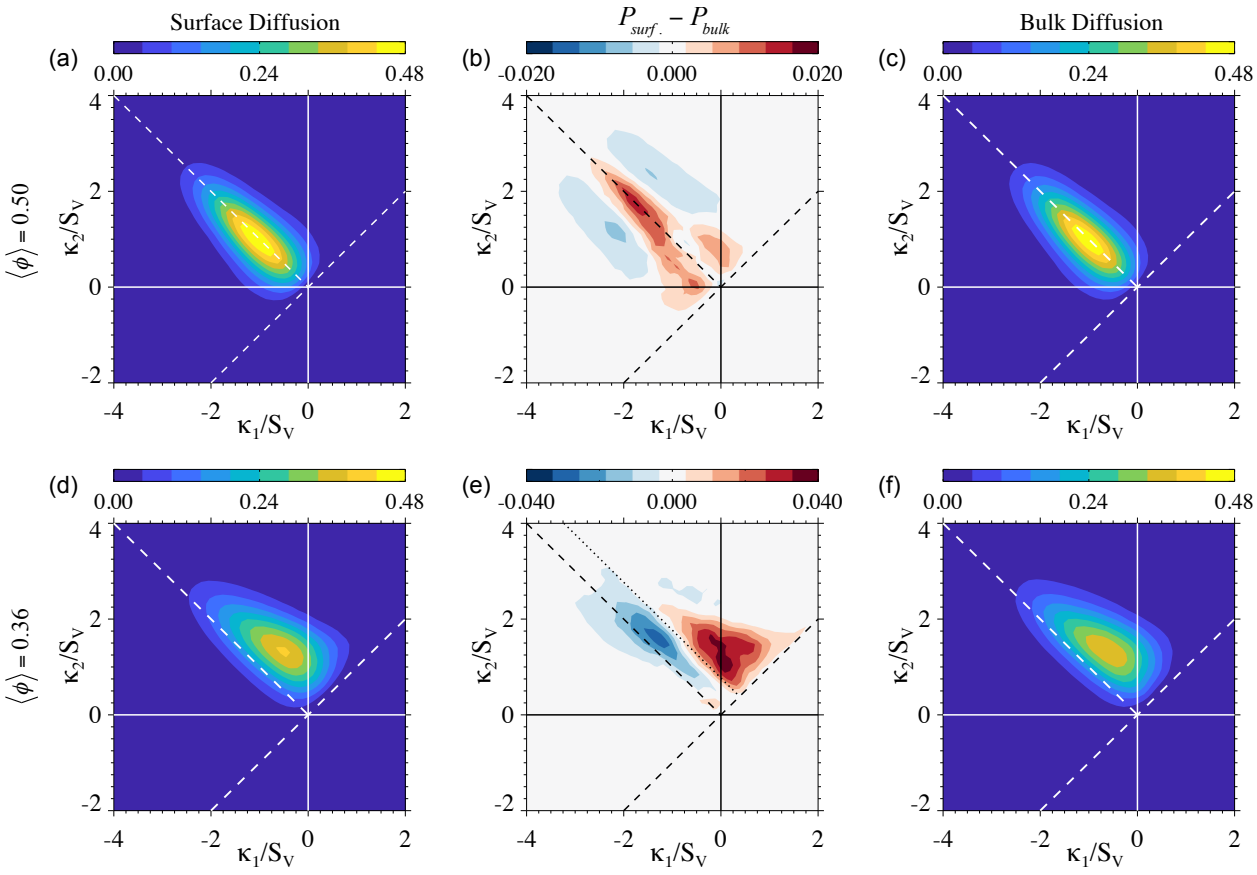

Figure 5.7: Comparison of self-similar average ISDs at (a-c) $\langle\phi\rangle = 0.50$ and (d-f) $\langle\phi\rangle = 0.36$, showing (a,d) the surface-diffusion ISDs, (b,e) the difference between bulk- and surface-diffusion ISDs, $P_{surf} - P_{bulk}$, and (c,f) the bulk-diffusion ISDs. The dotted line in (e) at $H/S_V = 0.38$ indicates the average scaled mean curvature of the bulk-diffusion case (f).

diffusion structures (and the lower $g_V S_V^{-3}$) may represent slower evolution of caps compared to necks relative to the bulk-diffusion case. However, self-similar solutions for the pinching-off of necks by bulk diffusion with uniform diffusivity have not yet been reported, so additional development of this hypothesis is left to future work.

5.3.4 Summary

Three-dimensional phase field simulations were conducted of phase separation and coarsening via surface diffusion at nominal volume fractions of 36% and 50% (average order parameter values of $\langle\phi\rangle = 0.36$ and $\langle\phi\rangle = 0.50$. These simulations resulted in bicontinuous microstructures, with no independent particles at 50% and a negligible volume and number of particles at 36%. The

evolution of morphology and topology was quantitatively analyzed, and convergence to a regime of self-similar coarsening was demonstrated in each case. Good agreement with the theoretical $t^{1/4}$ scaling law was observed during self-similar coarsening, and coarsening kinetics was found to be sensitive to volume fraction.

Simulations of coarsening via bulk diffusion were conducted to provide a quantitative comparison between the self-similar morphologies of each mechanism. At 36%, the surface-diffusion morphology has notably more positive elliptic area, where both mean and Gaussian curvature are positive. This correlated to lower scaled genus density and higher average scaled mean curvature than the bulk-diffusion case At 50%, the bulk- and surface-diffusion morphologies were very similar, with slight differences observed in the ISDs and statistics of mean curvature. With the notable exception of scaled genus density, all quantitative characteristics of the structures were more dependent on volume fraction than coarsening mechanism.

5.4 Coarsening at the limit of bicontinuity

The previous section described results for bicontinuous microstructures at 36% and 50% volume fractions of minority phase. In a previous study of coarsening via bulk diffusion [55], the topology of the structures was found to change abruptly from bicontinuous to disconnected (i.e., to a system of particles) when volume fraction is reduced from 36% to 30%. In this section, we examine coarsening via surface and bulk diffusion at an intermediate nominal volume fraction, 32%, which is close to the volume fractions of experimental nanoporous gold microstructures [128].

Simulations of coarsening via both mechanisms were conducted at $\langle\phi\rangle = 0.32$, and a simulation of coarsening via bulk diffusion was conducted at $\langle\phi\rangle = 0.30$. Besides $\langle\phi\rangle$, all three simulations used the same conditions as in the previous section. Structures at $\langle\phi\rangle = 0.32$ the end of the simulations are shown in Fig. 5.8. While overall the structures appear to be well-connected, there are isolated nearly-spherical particles in both cases, which is consistent with an intermediate state between the disconnected 30% case and the well-connected 36% case.

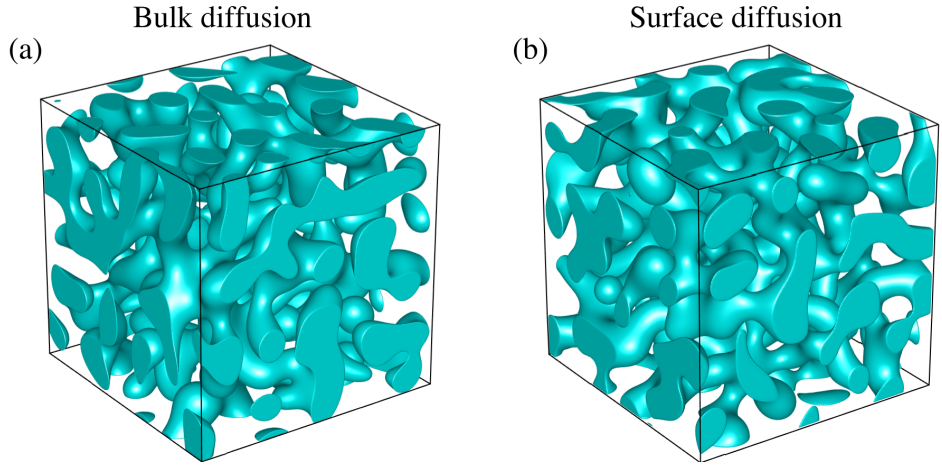

Figure 5.8: Samples of size $\left(10S_V^{-1}\right)^3$ of the (a) bulk-diffusion and (b) surface-diffusion structures at the end of the $\langle\phi\rangle = 0.32$ simulations, $S_V^{-1} = 74.8$ for bulk diffusion and $S_V^{-1} = 49.2$ for surface diffusion.

A mechanism for separation of particles is shown in Fig. 5.9 for the bulk-diffusion structure at $\langle\phi\rangle = 0.32$. Initially (Fig. 5.9a), a thin neck is the only connection between a large well-connected domain of $\phi = 1$ phase and a particle shaped like an elongated droplet. This thin neck narrows in Fig. 5.9b and has broken off completely in Fig. 5.9c, leaving the particle isolated. The remnants of the neck have receded by the time shown in Fig. 5.9c, leaving behind smooth interfaces.

The evolution of scaled topology is compared between the $\langle\phi\rangle = 0.32$ and $\langle\phi\rangle = 0.36$ structures in Fig. 5.10. The scaled genus density (Fig. 5.10a) of the $\langle\phi\rangle = 0.32$ structures is clearly much lower than the $\langle\phi\rangle = 0.36$ structures, and it is very different between coarsening mechanisms. As at $\langle\phi\rangle = 0.36$, the surface-diffusion structure at $\langle\phi\rangle = 0.32$ starts with higher genus density than the bulk-diffusion structure. However, this time it is decreasing during the evolution, while genus density of the bulk-diffusion structure is increasing.

The evolution of the scaled particle density $N_V S_V^{-3}$ is shown in Fig. 5.10b. The bulk-diffusion structure at $\langle\phi\rangle = 0.32$ initially appears to be breaking up, but its scaled particle density starts to decrease around $S_V^{-1} = 42$ and eventually stabilizes near 0.003 by the end of the simulation. In contrast, the surface-diffusion structure at $\langle\phi\rangle = 0.32$ appears to be breaking up continuously. In the bulk-diffusion case, particles have diffusional interactions with the rest of the structure, and may coarsen preferentially if their mean curvature is higher than that of neighboring interfaces.

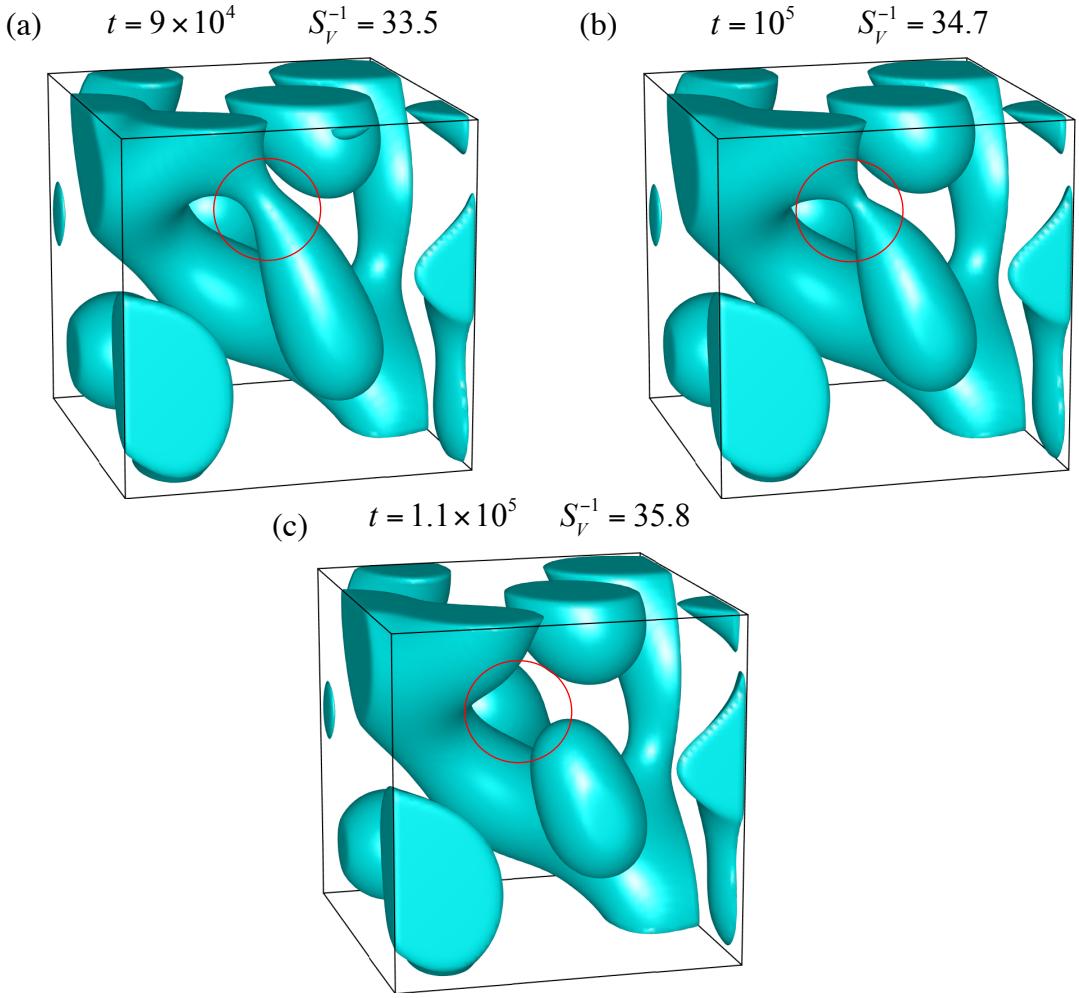

Figure 5.9: Separation of a particle from the main body of phase in the bulk-diffusion $\langle\phi\rangle = 0.32$ structure at (a) $t = 9\times10^4$, $S_V^{-1} = 33.5$, (b) $t = 10\times10^5$, $S_V^{-1} = 34.7$, and (c) $t = 1.1\times10^5$, $S_V^{-1} = 35.8$. In (a), the particle is initially attached to a larger domain of $\phi = 1$ phase b a thin neck (circled in red). This neck shrinks but is still present in (b), and in (c) it has pinched off, separating the particle from the structure. In (c), the interfaces where the neck used to be have already become smooth.

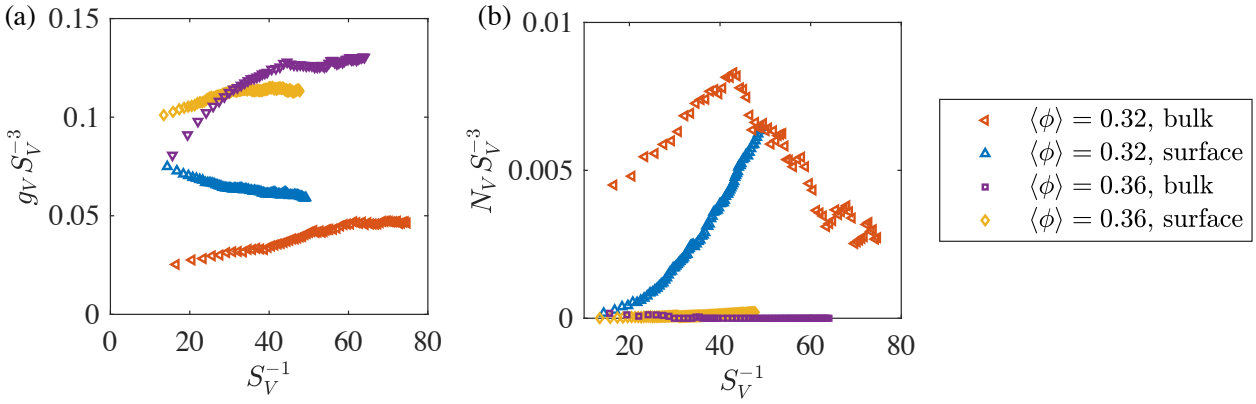

Figure 5.10: Evolution of (a) scaled genus density and (b) scaled particle density for the simulations at $\langle\phi\rangle = 0.32$ and $\langle\phi\rangle = 0.36$: $\langle\phi\rangle = 0.32$ bulk diffusion (red leftward triangles), $\langle\phi\rangle = 0.32$ surface diffusion (blue upward triangles), $\langle\phi\rangle = 0.36$ bulk diffusion (purple squares), and $\langle\phi\rangle = 0.36$ surface diffusion (yellow diamonds).

In the surface-diffusion case, independent particles can only interact with the main structure if by chance they come into contact with it again. There is no other mechanism for particles to disappear, and thus any particles that break away will persist in the structure for long times.

We note, however, that particles still represent a relatively small part of the structures. It is evident from Fig. 5.10 that there are always more necks or handles in the structure, as represented by $g_V S_V^{-3}$, than there are particles, represented by $N_V S_V^{-3}$. The particles also represent a small fraction of the total $\phi = 1$ phase, approximated as the total number of grid points with $\phi > 0.50$. The evolution of this fraction is shown in Fig. 5.11, and particles never contain more than 5% of the volume of $\phi = 1$ phase in the bulk-diffusion case, and never more than 1.5% in the surface-diffusion case.

The ISDs for these mixed bicontinous-particulate structures are depicted in Fig. 5.12 at a small characteristic length, and in Fig. 5.13 at the end of the simulations. All four ISDs are centered near the line $\kappa_1/S_V = 0$, which indicates cylindrical interfacial shapes. Initially, the bulk-diffusion ISD (Fig. 5.12a) has more elliptic interfaces, including some area along the line $\kappa_1 = \kappa_2$, which corresponds to spherical interfacial shapes, i.e., particles. The initial surface diffusion ISD (Fig. 5.12b) is less concentrated than the bulk-diffusion ISD. Over time, the bulk-diffusion ISD shifts to the lower left, with more area near the line $\kappa_1 = \kappa_2$ in Fig. 5.13a. Meanwhile, the late-time surface

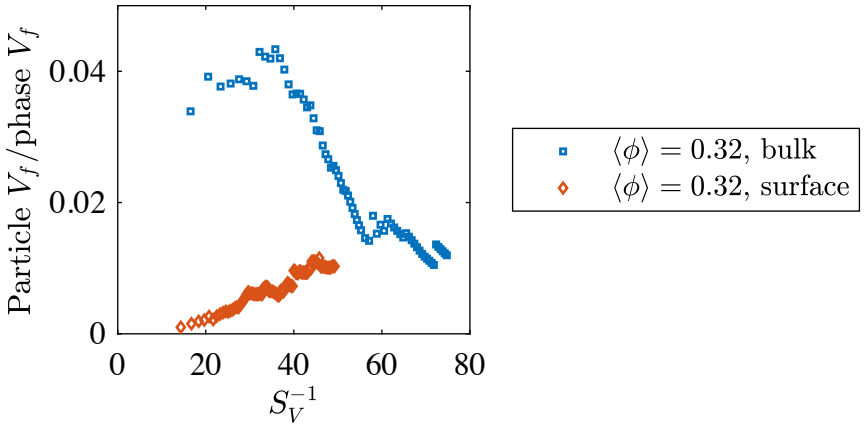

Figure 5.11: Evolution of the fraction of volume of $\phi = 1$ phase that is composed of particles for the $\langle\phi\rangle = 0.32$ bulk-diffusion (blue squares) and surface-diffusion (red diamonds) structures.

diffusion ISD (Fig. 5.13b) has increased area on the line $\kappa_1 = \kappa_2$ at relatively high curvatures. Overall, these trends are consistent with the changes in topology observed in Fig. 5.10: in the bulk-diffusion structure, less elliptic area increases genus density due to the Gauss-Bonnet theorem (Eq. 3.23), while in the surface-diffusion structure more area along the line $\kappa_1 = \kappa_2$ is consistent with more particles.

The substantial difference in initial structure between bulk and surface diffusion may be related to the total volume fraction V_f of $\phi = 1$ phase (approximated as the fraction of grid points with $\phi > 0.50$). This is plotted vs. S_V^{-1} in Fig. 5.14a. The bulk-diffusion structure has much lower V_f initially than the surface diffusion structure, although both converge over time toward the nominal value of 32%. Since the total composition of these systems is fixed, V_f is determined by the compositions of the phases. A possible reason for such a difference in composition is elucidated in Fig. 5.14b, which plots V_f vs. $\langle H\rangle$, the average unscaled mean curvature. The relationship between V_f and $\langle H\rangle$ appears to be linear for bulk diffusion, which implies that the overall average compositions of the phases (i.e., the mean field compositions) are set by the area average of mean curvature, $\langle H\rangle$. This is consistent with the relationship between local interfacial composition and mean curvature given by the Gibbs-Thomson effect, Eq. 2.33. The same mechanism (differences in volume fraction due to the Gibbs-Thomson effect) is also the most likely cause of the large differences between initial structures at $\langle\phi\rangle = 0.36$ found in the previous Section.

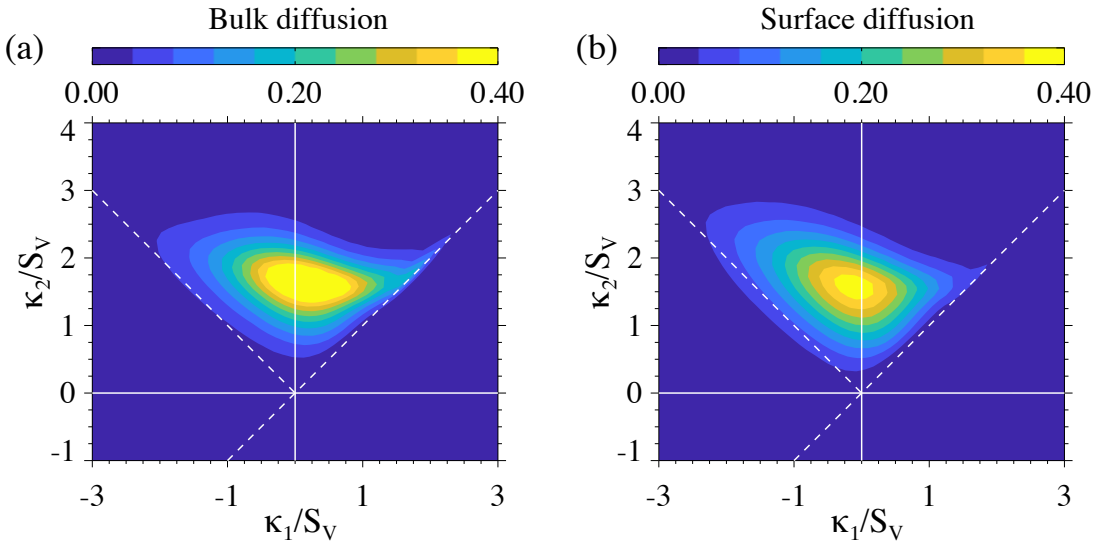

Figure 5.12: ISDs early in the coarsening process ($S_V^{-1} \approx 17$) for $\langle \phi \rangle = 0.32$ structures simulated with (a) bulk diffusion and (b) surface diffusion.

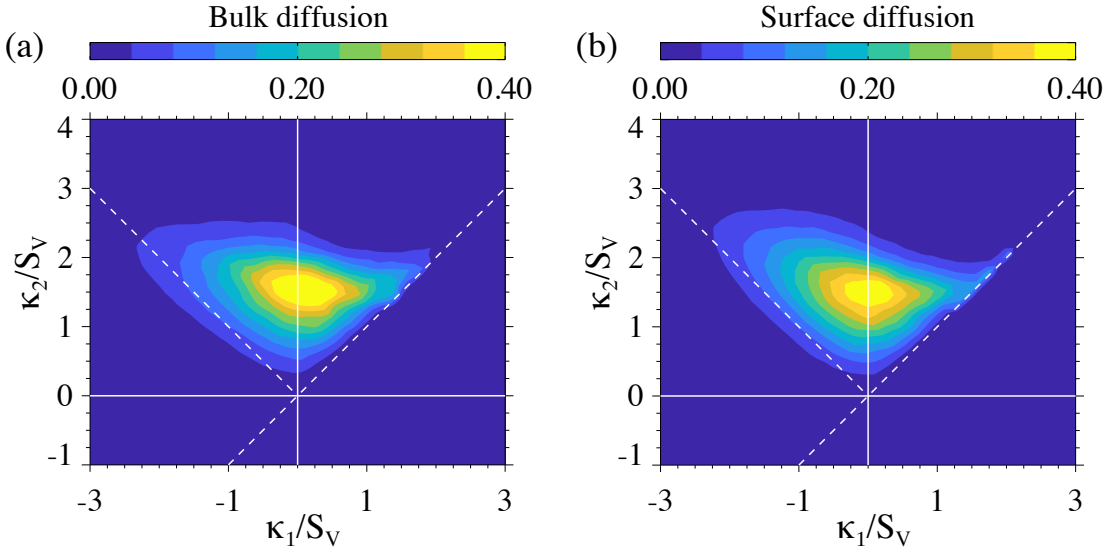

Figure 5.13: ISDs for structures at the end of the $\langle \phi \rangle = 0.32$ simulations with (a) bulk diffusion and (b) surface diffusion. The characteristic lengths are $S_V^{-1} = 74.8$ and $S_V^{-1} = 49.2$ for (a) and (b), respectively.

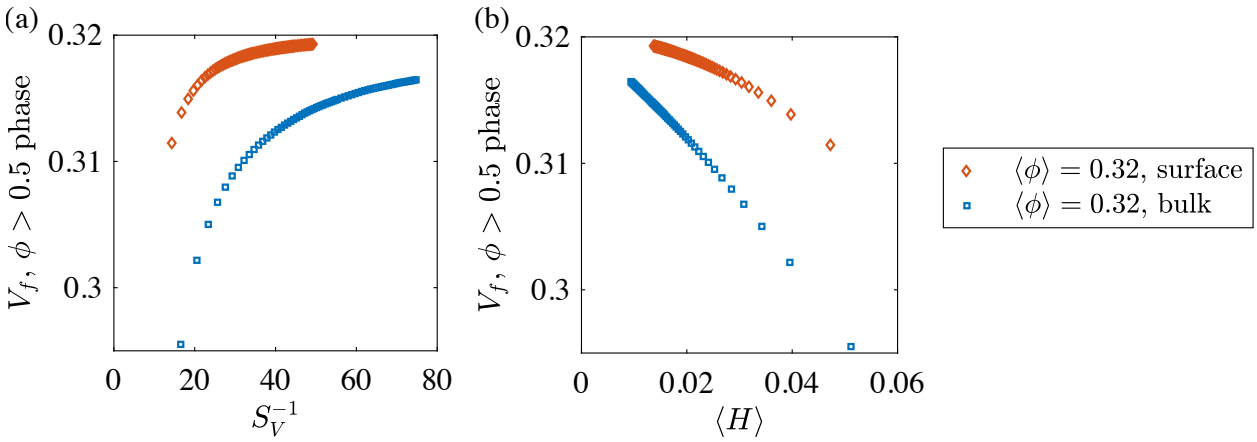

Figure 5.14: Evolution of the total volume fraction of $\phi = 1$ phase plotted vs. (a) S_V^{-1} and (b) $\langle H \rangle$, the average unscaled mean curvature, for the $\langle \phi \rangle = 0.32$ bulk-diffusion (blue squares) and surface-diffusion (red diamonds) structures.

To illustrate how sensitive the topologies of these structures are to volume fraction, Fig. 5.15 compares the bulk-diffusion cases at $\langle \phi \rangle = 0.32$ and $\langle \phi \rangle = 0.30$. The scaled scaled particle densities, scaled genus densities, and particle volume fractions of these cases are plotted in Figs. 5.15a, 5.15b, and 5.15b, respectively. Despite the small difference in composition, the transition from well-connected structure at $\langle \phi \rangle = 0.32$ to disconnected structure at $\langle \phi \rangle = 0.30$ is stark: the $\langle \phi \rangle = 0.30$ structure has substantially increased scaled particle density (Fig. 5.15a) and negligible scaled genus density (Fig. 5.15b). Most importantly, in Fig. 5.15c the volume fraction of independent particles (i.e., $\phi = 1$ phase domains not connected to the largest domain) increases to over 90% at $\langle \phi \rangle = 0.30$, while it is less than 5% at $\langle \phi \rangle = 0.32$. The $\langle \phi \rangle = 0.30$ has therefore completely broken up, and no single domain of $\phi = 1$ phase percolates throughout the structure. The total genus at the end of the simulation is $g = 3$.

5.5 Comparison of phase field models

The model of Rätz, Ribalta, and Voigt [136] enabled us to obtain the results in the previous sections. An alternative model, ostensibly for surface diffusion, was also examined: the Cahn-Hilliard model (Eq. 3.4) with the concentration-dependent mobility but without the stabilizing function introduced

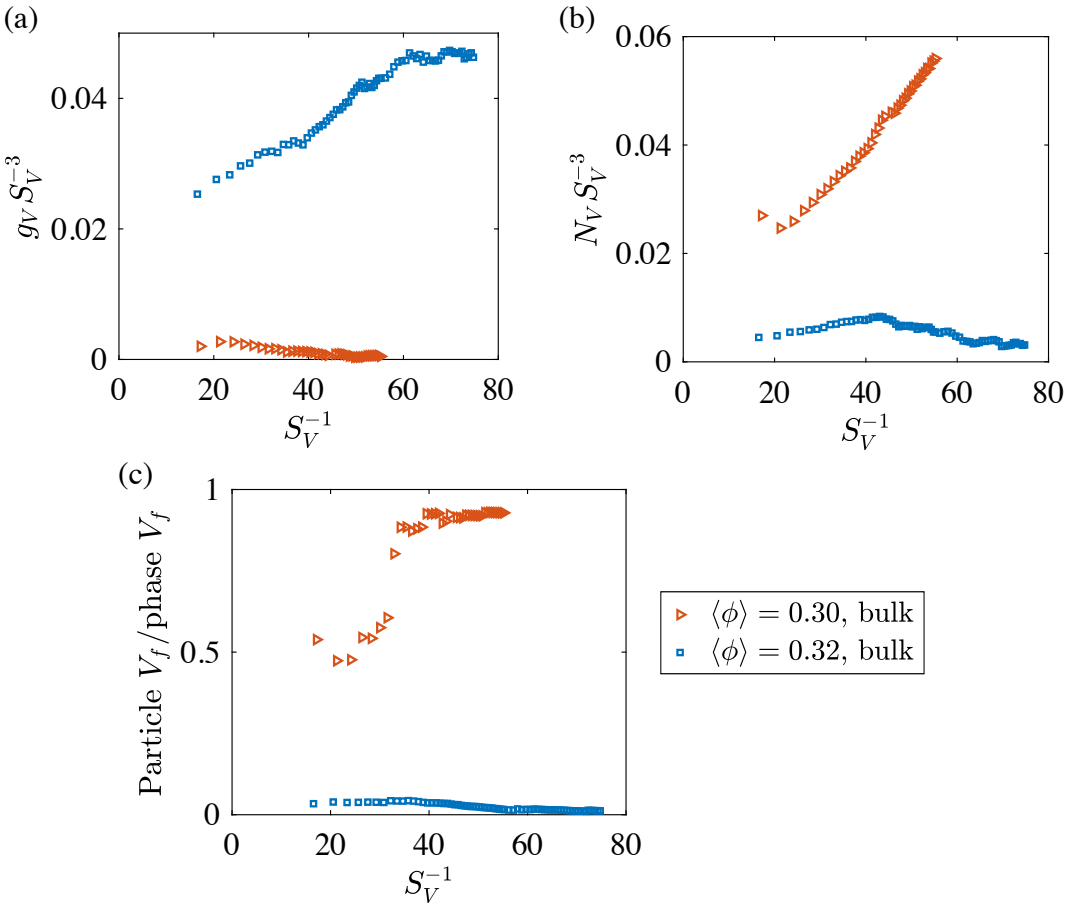

Figure 5.15: Evolution of (a) the scaled particle density, (b) the scaled genus density, and (c) the volume fraction of particles for the $\langle\phi\rangle = 0.30$ (red triangles) and $\langle\phi\rangle = 0.32$ (blue squares) bulk-diffusion structures.

in Eq. 5.4. We will refer to this model as the solubility-permitting (S-P) model, since it differs from the models examined by Cahn et al. [132]) by permitting solubility of non-majority components in the bulk phases. Additionally, in the S-P model the order parameter in the bulk will deviate from its bulk equilibrium values due to the Gibbs-Thomson effect, unlike in the RRV model [115]. The consensus from multiple critiques [115, 116, 117, 118, 137] of the S-P model is that it models interfacial motion due to surface diffusion and some amount of slow or sub-diffusive transport through the bulk, which has been likened to porous medium diffusion in the mathematical literature [116]. Lee et al. [118] note that the contribution of bulk diffusion can be reduced by changing the form of the mobility, for example by using $M(\phi) = \phi^2(1-\phi)^2$ in place of $M(\phi) = |\phi(1-\phi)|$. As they note, the thermodynamic behavior of the S-P model is still different from the deeply quenched or RRV models, but it is not obvious what role this will play in a dynamic process such as coarsening. To answer this question, we perform simulations using a form of the solubility-permitting model.

The specific S-P model we examine is the Cahn-Hilliard equation, Eq. 3.4, with the order parameter-dependent mobility $M(\phi) = 16\phi^2(1-\phi)^2$. The sharp interface dynamics of this system does not correspond strictly to surface diffusion, Eq. 2.41, since there is a contribution from bulk diffusion [115, 116, 118]. However, determining the kinetic coefficient η in Eq. 2.41 enables us to compare the S-P model to the RRV model. Neglecting the contribution from bulk diffusion, we obtain η from Ref. [132],

$$\eta = \frac{\varepsilon\gamma}{(\phi_0^+ - \phi_0^-)^2} \int_{\phi_0^-}^{\phi_0^+} \frac{M(\phi)}{\sqrt{2f(\phi)}} d\phi, \tag{5.7}$$

where the interfacial energy γ is given by Eq. 3.6.

Two simulations were performed using the S-P model, one with $\langle\phi\rangle = 0.50$ with a domain size of $L_x = L_y = L_z = 1024$, and one with $\langle\phi\rangle = 0.36$ with a domain size of $L_x = L_y = L_z = 800$. The parameters $\varepsilon^2 = 0.2$ and $W = 0.4$ were used, which result in $\eta = 4/45$. The numerical scheme was the same as in the previous section, with $\Delta x = 1$ and $\Delta t = 0.05$.

Coarsening kinetics of the S-P and RRV models are compared in Fig. 5.16, which plots S_V^{-4} vs. the scaled time, $t^* = \eta t$. With this time scaling, both models correspond to the same surface

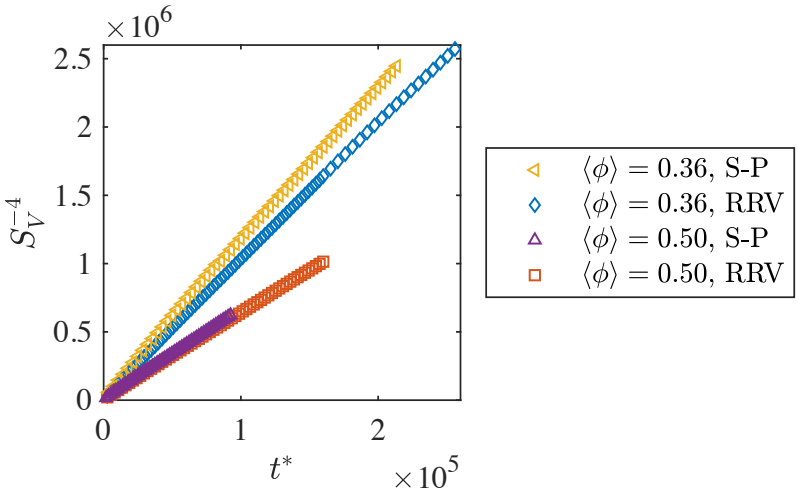

Figure 5.16: Comparison of coarsening kinetics for different models for surface diffusion: the solubility-permitting (S-P) model at $\langle\phi\rangle = 0.36$ (yellow leftward triangles) and at $\langle\phi\rangle = 0.50$ (purple upward triangles), and the RRV model at $\langle\phi\rangle = 0.36$ (blue diamonds) and at $\langle\phi\rangle = 0.50$ (red squares).

diffusion equation,

$$\frac{\partial\phi}{\partial t^*} = \nabla_s^2 H. \tag{5.8}$$

Any difference in kinetics is therefore caused by either a difference in morphology or the bulk diffusion present in the S-P model. Comparing fits of the data in Fig. 5.16 to Eq. 5.6, we find that the S-P model has a rate constant 5% higher than that of the RRV model at $\langle\phi\rangle = 0.50$. The morphologies resulting from the two models at $\langle\phi\rangle = 0.50$ were statistically indistinguishable, with $||P_{S\text{-}P}(t) - P_{RRV}(t)||_1 < 0.02$ for most of their evolution. The small difference in kinetics can therefore be attributed to bulk diffusion in the S-P model.

We also compare the evolution of the total free energy (i.e., F in Eq. 3.1) between the RRV and S-P models at $\langle\phi\rangle = 0.50$ in Fig. 5.17. Total free energy is expected to decrease monotonically in time for the S-P model [131], and this is observed in Fig. 5.17. The same behavior is observed for the RRV model despite its non-variational chemical potential. Energy of the S-P model decreases slightly faster, which is consistent with its faster coarsening kinetics. Most of the decrease in energy occurs in the first time increment (corresponding to phase separation), and greater time resolution in this interval could elucidate additional differences between the models.

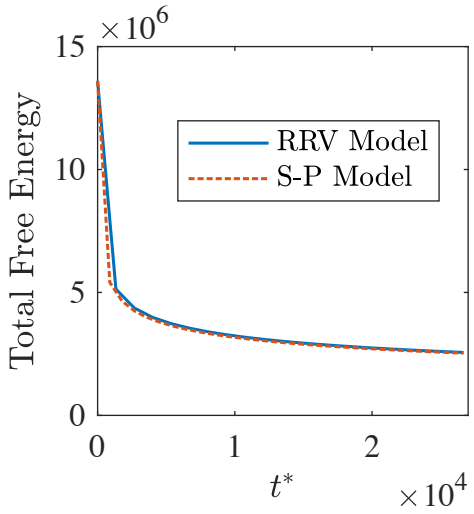

Figure 5.17: Evolution of total energy vs. scaled time at $\langle\phi\rangle = 0.50$ for the RRV model (solid blue line) and the S-P model (red dashed line).

There are larger differences in kinetics and morphology between the RRV and S-P models at $\langle\phi\rangle = 0.36$. The difference in coarsening rate constant is larger, 12% higher for the S-P model than the RRV model, and the morphologies are substantially different. Fig. 5.18 compares the evolution of morphological statistics between the S-P and RRV models for surface diffusion and the bulk-diffusion case. Figs. 5.18a and 5.18b show the evolution of scaled average mean curvature and scaled genus density. At the smallest characteristic length (i.e., immediately following phase separation) the S-P case is much closer in morphology and topology to the bulk-diffusion case than the RRV case. This results in substantially longer transient behavior for the S-P case than for the RRV case, despite faster evolution of the morphology with respect to S_V^{-1} for the S-P case.

The cause of this difference in behavior is illustrated in Fig. 5.18c, which plots the volume fraction of $\phi = 1$ phase (approximated as the fraction of grid points with $\phi > 0.50$) vs. average mean curvature. Identical linear correlations are observed between these quantities for the bulk and S-P cases, while the volume fraction of the RRV case converges non-linearly to the nominal volume fraction, $V_f = \langle\phi\rangle = 0.36$. This relationship between $\langle H\rangle$ and V_f is theoretically predicted for the bulk-diffusion case (see previous Section). The S-P model has the same bulk thermodynamics as bulk diffusion, and therefore some relationship between $\langle H\rangle$ and V_f is expected. What is interesting about our result is that the same relationship is observed in both the bulk-diffusion and solubility-

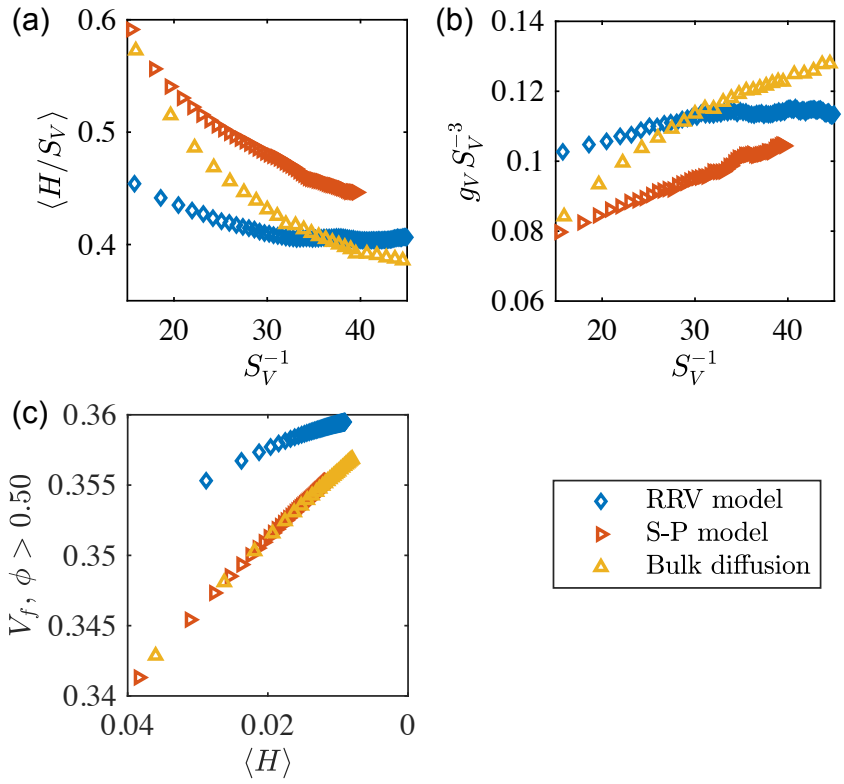

Figure 5.18: Comparison of morphological evolution with $\langle \phi \rangle = 0.36$ between the RRV model (blue diamonds) and S-P model (red rightward triangles) for surface diffusion, and the bulk-diffusion case (yellow upward triangles). The evolution of (a) average scaled mean curvature and (b) scaled genus density are plotted vs. characteristic length, while (c) plots volume fraction of $\phi = 1$ phase vs. average mean curvature. The axis in (c) is reversed to indicate the evolution of $\langle H \rangle$ in time.

permitting models. Reduced mobility in the bulk does not prevent the order parameter in the bulk from reaching its mean field value, nor does it appear to 'trap' the order parameter at non-mean field values.

The results of this comparison between models complement those of Lee et al. [117, 118]. We find that an order-parameter dependent mobility alone is insufficient to model coarsening via surface diffusion. Morphology will be substantially affected by interactions with the bulk unless the thermodynamics of the model are modified as in the RRV [136] or Cahn et al. [132] models. The effect of interactions with the bulk was minimized in our $\langle \phi \rangle = 0.50$ simulation due to the symmetry between the phases, since the average mean curvature (and therefore the mean field chemical potential) was zero.

5.6 Conclusions

3-D simulations of coarsening via surface diffusion were performed with large sample microstructures and periodic boundary conditions using the model proposed by Rätz et al. [136]. At system compositions of $\langle\phi\rangle = 0.36$ and $\langle\phi\rangle = 0.50$, which represent nominal volume fractions of $\phi = 1$ phase of 36% and 50%, self-similar coarsening via surface diffusion was observed for the first time. Scaling of morphology and topology were observed, and coarsening kinetics followed the predicted $t^{1/4}$ power law These self-similarly evolving systems had bicontinuous morphologies, similar to those observed during coarsening via bulk diffusion. Quantitative differences were found between these surface- and bulk-diffusion cases, with lower scaled genus density and lower standard deviation of mean curvature in the surface-diffusion case. Yet overall the difference between morphologies due to coarsening mechanism was smaller than the effect of volume fraction, and the bulk- and surface-diffusion structures were especially similar at 50%.

Coarsening via surface and bulk diffusion was also examined at a lower volume fraction, with $\langle\phi\rangle = 0.32$. These case resulted in structures that contained both a single well-connected domain (typical of bicontinuous structures) and a number of independent particles. Substantial transient evolution of the scaled morphology and topology was observed in both structures. In both structures, particles break off from the larger domain during evolution, but their subsequent evolution depends on the coarsening mechanism. In the surface-diffusion case, independent particles are only rarely absorbed into the main domain of $\phi = 1$ phase, and therefore the scaled particle density is monotonically increasing. In the bulk-diffusion case, particles can shrink and disappear due to diffusional interactions, and the scaled particle density increases initially and then declines to a low late-time value. This change in regime in the bulk diffusion case may have been due to changes in volume fraction over time, which converged toward the nominal value of 32% following a linear relationship with average unscaled mean curvature, which decreases to zero as the structure coarsens. Volume fraction may also explain a considerable difference in early-time morphology and topology between surface- and bulk-diffusion cases. The sensitivity of the structures to vol-

ume fraction was confirmed by examining coarsening via bulk diffusion at 30% volume fraction, in which the initial structure was observed to break up rapidly into particles.

Finally, coarsening was examined via alternative model, which employed the concentration-dependent mobility of the surface-diffusion model but retained the thermodynamics of the bulk-diffusion model, allowing solubility of the order parameter in the bulk. While this solubility-permitting model was shown to have similar coarsening kinetics to the surface diffusion model, including $t^{1/4}$ power-law coarsening, the morphologies observed initially were closer to those observed for bulk diffusion. This resulted in slow, transient evolution of the scaled morphology, and self-similar coarsening was not observed. These substantial differences indicate that the solubility-permitting model does not effectively simulate surface diffusion, complementing the results of recent analytical studies [116, 117, 118].

In summary, this chapter represents pioneering results for coarsening via surface diffusion, a phenomenon that is of increasing engineering importance. The morphologies that are presented here can be compared directly to experimental results. The effects of volume fraction and differences between the bulk- and surface-diffusion structures that have been observed add to the body of knowledge regarding coarsening, and will inform future hypotheses about coarsening dynamics.

Chapter 6

A model for coarsening via bulk diffusion with strongly anisotropic interfacial energy

6.1 Introduction

The phase field models employed thus far do not include interfacial energy anisotropy, which, as noted in Chapter 1, is expected when at least one of the phases is crystalline. Interfacial energy anisotropy is the dependence of the interfacial energy on the orientation of the interface, represented by an angle θ or normal vector $\vec{n}$, relative to the orientation of the crystal lattice. Interfacial energy anisotropy plays a key role in processes such as solidification [140, 141], evolution of thin films [134, 142, 143], nanowire growth [144], and grain boundary evolution [145]. In the absence of elastic effects, interfacial energy anisotropy fully determines the equilibrium shapes of individual particles via the well-known Wulff construction [80, 146]. The present work analyzes the suitability of an existing type of phase field model for strong anisotropy, introduced by Wise and coauthors [134, 143] for evolution of thin films and by Wheeler [147] for solidification of a pure material, for the case of transport via bulk diffusion. The sharp interface dynamics corresponding to the phase field model are obtained, and simulated equilibrium shapes of particles are compared to sharp interface predictions. Our results explain changes to the equilibrium shape that were observed by Wise et al. [134] that were not predicted by Wheeler's analysis [147].

We will begin by reviewing the thermodynamics of anisotropic interfaces from a sharp inter-

face perspective, first in 2D and then in 3D, before proceeding to phase field models for strong anisotropy. The total interfacial energy F_{int} of the 2D system is given by [148],

$$F_{int} = \int_S \gamma(\theta) ds \tag{6.1}$$

where, as in Chapter 2, s is arclength, S is the interface, θ is the orientation angle, the angle (measured clockwise) between the interface normal and the fixed reference vector $(0,1)$, and γ is the interfacial energy. When the interfacial energy $\gamma(\theta)$ is a smooth function of θ, the the anisotropic equivalent of the Gibbs-Thomson equation (Eq. 2.31) can be obtained [149]:

$$\mu = \mu^e + \frac{\gamma(\theta) + \gamma''(\theta)}{X_\beta - X_\alpha}\kappa, \tag{6.2}$$

where the term $\gamma''(\theta) = \frac{\partial^2 \gamma}{\partial \theta^2}$ corresponds to the change in orientation of the interface due to a normal displacement [66], and κ is scalar curvature. At equilibrium, chemical potential must be constant at all points, and the equilibrium shape of a particle with constant chemical potential (i.e., the Wulff shape) can be determined by setting μ to be constant in Eq. 6.2. When anisotropy is present, the curvature κ varies along the interface to offset the variation $\gamma + \gamma''$ [59].

Anisotropy is considered strong [150] when $\gamma(\theta)$ contains cusps (resulting in flat facets at discrete orientations) or has orientations at which $\gamma + \gamma'' < 0$ (resulting in sharp corners in the equilibrium shape). At cusps in $\gamma(\theta)$, its derivative γ' is discontinuous and its second derivative γ'' does not exist, requiring a different form for the Gibbs-Thomson equation from Eq. 6.2. To avoid this additional complexity, we will focus on interfacial energies with orientations for which $\gamma + \gamma'' < 0$. Facets are still possible in this case, but they will contain a small range of orientations rather than a single discrete orientation.

When orientations exist for which $\gamma + \gamma'' < 0$, the constant-chemical-potential shape contains lobes, shown in Fig. 6.1, that are truncated to find the equilibrium shape [151]. Orientations for which $\gamma + \gamma'' < 0$ are labeled as unstable, and orientations for which $\gamma + \gamma'' >= 0$ but are still missing from the equilibrium shape are labeled as metastable. An unstable orientation would sponta-

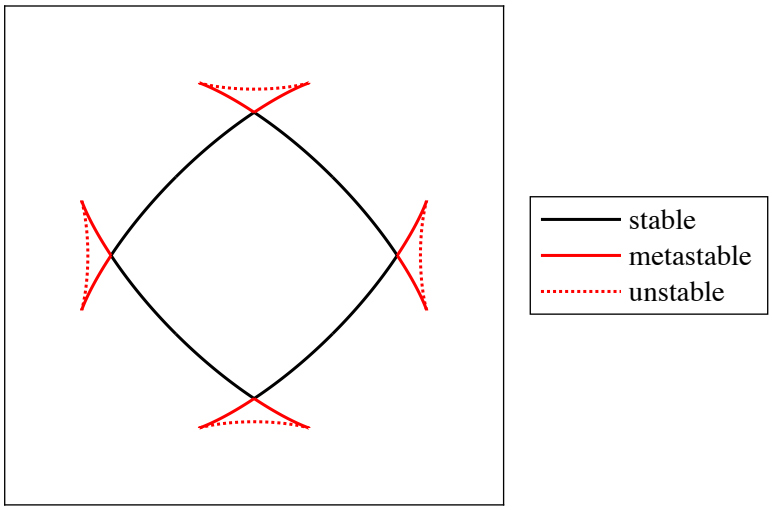

Figure 6.1: Wulff construction for $\gamma = 1 + 0.2\cos 4\theta$ highlighting stable orientations (solid black line), metastable orientations (solid red lines), and unstable orientations (dashed red lines). Removing the lobes containing metastable and unstable orientations results in the physical equilibrium shape.

neously decompose into a corrugated 'hill-and-valley' structure of oppositely facing stable facets, as there is no energy barrier [148], while metastable orientations are energetically unfavorable, but they have an energy barrier for nucleation of the oppositely facing facet. Therefore metastable orientations will not decompose without a perturbation. In experimental systems, surfaces may become unstable due to changes in temperature or vapor pressure [152], and Fig. 6.2 depicts the hill-and-valley structure resulting from temperature-induced decomposition of a vicinal Si(111) surface [153]. The decomposition of unstable interfaces has been considered as analogous to spinodal decomposition [154, 155, 156], in which there is no energy barrier to prevent a single-phase state at an unstable composition from decomposing into two stable phases.

Evolution of a curve in 2D with interfacial energy anisotropy was examined by Angenent and Gurtin [149]. They found that if $\gamma + \gamma'' < 0$, the evolution equation was backward parabolic. In parabolic equations, such as the diffusion equation,

$$\frac{\partial \phi}{\partial t} = \nabla^2 \phi, \tag{6.3}$$

fluctuations in initial data are smoothed out, with smaller-wavelength fluctuations disappearing

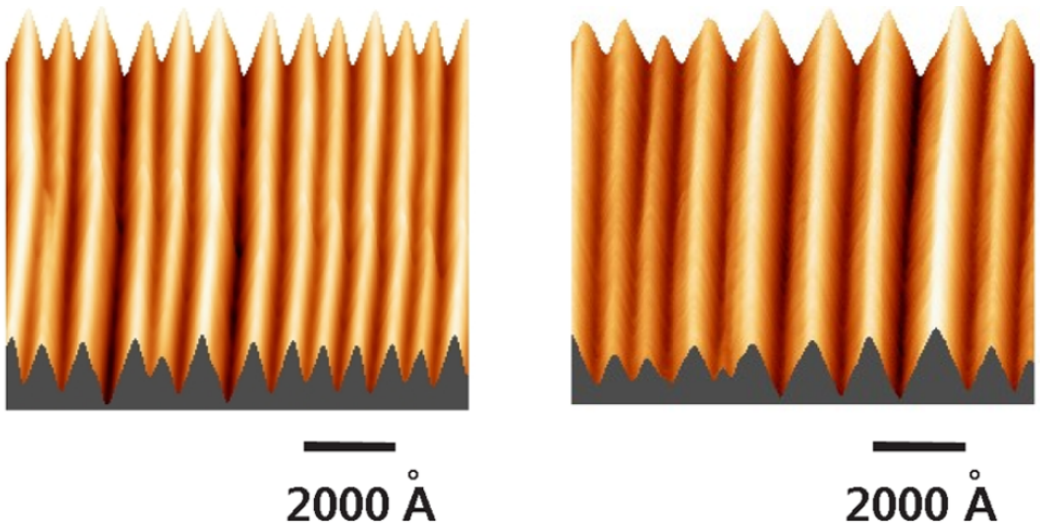

Figure 6.2: Ex-situ atomic force microscopy images of a vicinal Si(111) surface (3.5^o miscut angle) annealed at 35 K below the (1×1)-to-(7×7) transition temperature for 900 s (left) and 1800 s (right). Reprinted from [153] with permission.

more rapidly than larger wavelength fluctuations [98]. Solutions to the diffusion equation are also unique for a given initial condition [157]. The opposite behavior is expected for backward parabolic equations, such as the backwards diffusion equation,

$$\frac{\partial \phi}{\partial t} = -\nabla^2 \phi. \tag{6.4}$$

Since multiple initial conditions can result in the same solution to the (forward) diffusion equation, there can be multiple solutions to the backward diffusion equation for the same initial condition. Additionally, since small fluctuations now increase more rapidly than large fluctuations, solutions to the backwards diffusion equation vary discontinuously with changes in initial data [98]. Clearly, a particular solution to the backward diffusion equation is not as meaningful as a solution to the (forward) diffusion equation. In mathematical terminology, either of these conditions, non-uniqueness of solutions and discontinuous dependence on initial data, makes the equation ill-posed [98]. Angenent and Gurtin [149] note that, as a backward parabolic equation, the evolution equation with $\gamma + \gamma'' < 0$ was ill-posed.

DiCarlo et al. [156] proposed an evolution equation that removes the ill-posedness by including

a curvature-dependent regularization term into the interfacial energy,

$$F_{int} = \int_S \left[\gamma(\theta) + \frac{1}{2}\beta\kappa^2 \right] ds, \tag{6.5}$$

where β is the regularization parameter. The regularization term $\beta\kappa^2$ penalizes sharp transitions in orientation (i.e., corners), introducing a physically relevant corner energy into the model [155] that is not present in the non-regularized energy, Eq. 6.1. This corner energy provides the driving force for facet coarsening observed in Fig. 6.2, where the number of facets in the system (and therefore the number of corners) decreases over time. The regularization also results in rounding of corners over a length scale proportional to $\beta^{1/2}$ [59, 148], which is observed experimentally at the nanoscale [145, 158].

We now consider interfacial energy anisotropy in a three-dimensional (3-D) system. The anisotropic Gibbs-Thomson equation in 3D is given by [60],

$$\mu = \mu^e + \frac{1}{(X_\beta - X_\alpha)} \sum_i^3 \sum_j^3 \left[P_{ij}\gamma(\vec{n}) + \frac{\partial^2 \gamma(\vec{n})}{\partial n_i \partial n_j} \right] h_i^{\ j}, \tag{6.6}$$

in terms of the quantities defined in Section 2.1.2, i.e., where P_{ij} is the projection tensor, $P_{ij} = \delta_{ij} - n_i n_j$ and $h_i^{\ j}$ is the shape tensor, $\nabla_S \vec{n}$. For the case where the coordinates x_1 and x_2 are in the directions of the principal curvatures κ_1 and κ_2, this reduces to [66],

$$\mu = \mu^e + 2H\gamma(\vec{n}) + \left(\frac{\partial^2 \gamma(\vec{n})}{\partial n_1^2}\kappa_1 + \frac{\partial^2 \gamma(\vec{n})}{\partial n_2^2}\kappa_2 \right). \tag{6.7}$$

An alternative way of expressing Eq. 6.6 was introduced by Cahn and Hoffman [159, 160]. They define a vector, $\vec{\xi}$, in terms of a homogeneous extension of $\gamma(\vec{n})$ $\gamma_{ext}(r\vec{n}) = r\gamma(\vec{n})$, where r is a scalar variable,

$$\vec{\xi} = \frac{\partial \gamma_{ext}(r\vec{n})}{\partial(r\vec{n})}. \tag{6.8}$$

The anisotropic Gibbs-Thomson equation in terms of this ξ-vector is [160],

$$\mu = \mu^e + \frac{\nabla_s \cdot \vec{\xi}}{(X_\beta - X_\alpha)}, \tag{6.9}$$

and the envelope of ξ-vectors is geometrically similar to the equilibrium shape. Strong anisotropy is of course still present in 3D. The criterion for missing orientations [60, 161] in 3D is the non-convexity of $\left[P_{ij}\gamma(\vec{n}) + \frac{\partial^2 \gamma(\vec{n})}{\partial n_i \partial n_j}\right]$ in Eq. 6.6. For sharp interface evolution in 3D, Gurtin and Jabbour [60] proposed a regularization of the form

$$F_{int} = \int_S \left[\gamma(\vec{n}) + \frac{1}{2}\beta_1 H^2 + \frac{1}{2}\beta_2 \left(2H^2 - K\right)\right] dA, \tag{6.10}$$

although we will not consider any models for which $\beta_2 \neq 0$. The term H^2 in Eq. 6.10 is known as the Willmore energy [135, 136].

An approach for incorporating general interfacial energies (i.e., any form of $\gamma(\vec{n})$ was introduced by Kobayashi [140] for a model of solidification. For the Cahn-Hilliard free energy in Eq. 3.1, this method of incorporating anisotropy results in

$$F = \int_\Omega \left[f(\phi) + \frac{1}{2}|\varepsilon(\vec{n})\nabla\phi|^2\right] dV, \tag{6.11}$$

where the normal vector is calculated using the gradient of the order parameter (e.g., $\vec{n} = \nabla\phi/|\nabla\phi|$) and the gradient energy coefficient $\varepsilon(\vec{n})$ is proportional to the anisotropic interfacial energy, $\varepsilon(\vec{n}) = \gamma(\vec{n})/\gamma_0$. The chemical potential for this model is

$$\mu = f'(\phi) - \nabla \cdot \left[|\varepsilon(\vec{n})\nabla\phi|\vec{\xi}\right], \tag{6.12}$$

where $\vec{\xi}$ is the Cahn-Hoffman ξ-vector defined in Eq. 6.8 with $r = |\nabla\phi|$. In this case, Eq. 6.8 evaluates to

$$\xi_i = \tilde{\varepsilon} n_i + P_{ij}\frac{\partial \tilde{\varepsilon}}{\partial n_j}, \tag{6.13}$$

where P_{ij} is the projection tensor defined in Chapter 2. It should be noted that specific forms of anisotropy were considered in phase field models prior to Ref. [140]. Notably, Cahn and Hilliard [64] incorporated it via a second-rank tensor α_{ij},

$$F = \int_{\Omega} \left[f(\phi) + \frac{1}{2} \sum_i \sum_j \alpha_{ij} \frac{\partial \phi}{\partial x_i} \frac{\partial \phi}{\partial x_j} \right] dV. \tag{6.14}$$

This is a limited form of anisotropy in which the equilibrium shape must be an ellipsoid [150]; in coordinates where α_{ij} is diagonal, it corresponds to $\varepsilon(\vec{n}) = \alpha_{11} n_1^2 + \alpha_{22} n_2^2 + \alpha_{33} n_3^2$. Higher order tensors [162, 163] and Fourier expansions in orientation angles [164] have been employed to generalize this approach to more complex forms of anisotropy (e.g., cubic and hexagonal symmetries). However, we focus on the general form in Eq. 6.11, which can, for example, model nearly-flat facets for crystals with arbitrary symmetries simply by modification of $\gamma(\vec{n})$ (see e.g., Ref. [144]).

Strong anisotropy results in the ill-posedness of phase field models under the same conditions as sharp-interface models [150]. There are three main approaches to regularizing this ill-posedness. One approach is to rely on the numerical method for regularization (e.g., Ref. [165]). Taylor and Cahn [150] argue that results in this case are meaningful only if the missing orientations are not present. Another is to convexify the anisotropy [142, 150], which entails modifying $\gamma(\vec{n})$ such that all orientations are stable while preserving the strongly anisotropic equilibrium shape, including the sharp corners. Alternatively, the anisotropy can be designed to have nearly-sharp corners while preserving convexity [166]. Both of these result in well-posedness, but they cannot model the decomposition of unstable interfaces, as all orientations are stable [60]. They may still be effective approximations for strong anisotropy under certain conditions; for example, if the length scale and energy scale of the rounded corner are small compared to the scale of the overall simulation, and the decomposition process is not of interest.

The remaining approach is to introduce a higher-order term that penalizes curvature, as in the sharp interface case. This was initially done via the tensor-based method by Abinandanan and

Haider [162],

$$F = \int_\Omega \left[f(\phi) + \frac{1}{2}\alpha|\nabla\phi|^2 + \sigma_{ijlm}\frac{\partial^2\phi}{\partial x_i \partial x_j}\frac{\partial^2\phi}{\partial x_l \partial x_m} \right] dV. \tag{6.15}$$

They analyzed the interfacial energy of this system in one dimension and found it to be determined by the scaling factor $\sigma^{1/4}/\sqrt{\alpha}$. Furthermore, they found good agreement between calculated Wulff shapes (using the numerically calculated interfacial energy) and simulated shapes, with the simulated shapes having rounded corners. For general anisotropy, Wise et al. [134, 143] and Wheeler [147] proposed the regularization energy density $f_{reg} = \frac{1}{2}\delta^2(\nabla^2\phi)^2$, where δ is the regularization parameter. Wise et al. introduced this Laplacian-squared regularization into a Cahn-Hilliard model,

$$F = \int_\Omega \left[f(\phi) + \frac{1}{2}|\varepsilon(\vec{n})\nabla\phi|^2 + \frac{\delta^2}{2}(\nabla^2\phi)^2 \right] dV, \tag{6.16}$$

while Wheeler [147] considered it for solidification of a pure material. Wheeler also analyzed the diffuse corner shape resulting from this regularization, but he treated the regularization as a regular perturbation away from the corner, essentially neglecting its effect on interfacial energy.

A different regularization, $f_{reg} = \frac{1}{2}\delta^2\left(f'(\phi) - \nabla^2\phi\right)^2$ was introduced by Rätz et al. [136], where it is assumed that $f(\phi_0) = f'(\phi_0) = 0$ at the equilibrium concentrations of the phases. For a phase field model with isotropic interfaces, this f_{reg} was conjectured by De Giorgi [167] to approximate H^2 (i.e., the regularization energy in Eq. 6.10 with $\beta_2 = 0$) in the sharp interface limit. However, the anisotropic phase field model in Eq. 6.11 has an orientation-dependent interfacial width that results in excess energy at flat interfaces. Torabi et al. [135] solved this inconsistency by introducing a new formulation of the anisotropy. Including the regularization, the free energy of this model can be written as

$$F = \int_\Omega \varepsilon(\vec{n}) \left[f(\phi) + \frac{1}{2}|\nabla\phi|^2 \right] + \frac{\delta^2}{2}\left[f'(\phi) - \nabla^2\phi\right]^2 dV. \tag{6.17}$$

While this formulation contains the desired chemical potential at the interface, it modifies the bulk thermodynamics, and a relationship analogous to Eq. 2.33 can be obtained for the order parameter

in the bulk,

$$\phi = \frac{\mu}{\varepsilon(\vec{n}) f''(\phi_0^+)}. \tag{6.18}$$

The Torabi et al. model was designed for surface diffusion, in which case there should be $\mu = 0$ in the bulk. Expanding the regularization energy reveals another possible concern for bulk diffusion,

$$f_{reg} = \frac{1}{2}\delta^2 \left(\left[f'(\phi) \right]^2 - 2 f'(\phi) \nabla^2 \phi + \left(\nabla^2 \phi \right)^2 \right) \tag{6.19}$$

Terms containing $\nabla^2\phi$ are expected to go to zero far from the interface [64], but that leaves a bulk-only term, $[f'(\phi)]^2$. This quantity is zero at equilibrium, and is therefore likely to be small in coarsening simulations, but it may be non-negligible for large values of the regularization parameter δ.

To model regularized strong anisotropy with bulk diffusion, we re-examine the Laplacian-squared regularization introduced in Refs. [134, 143, 147]. We consider the effect of the regularization on a planar interface, similarly to Abinandanan and Haider [162], but we additionally analyze the sharp interface behavior of the model using matched asymptotic expansions. Our approach differs from that of Wheeler [147] in that we consider the effect of the regularization at leading order in the inner solution (i.e., in the interface) away from corners. The result of the asymptotic analysis is that the regularized model contains the correct Gibbs-Thomson condition for a modified interfacial energy, with no other effect on dynamics up to second order in the interfacial width. This result justifies a comparison between simulated and predicted shapes, as has been conducted for tensor-based models [162, 168]. Again we go further by demonstrating that the corner shape with the Laplacian-squared regularization corresponds very well to sharp interface predictions [59] for the κ^2 regularization in Eq. 6.5.

6.2 Anisotropic phase field model

The free energy of the model we examine is defined by Eq. 6.16. The time evolution of the order parameter is given by the Cahn-Hilliard equation,

$$\frac{\partial \phi}{\partial t} = \nabla^2 \mu, \tag{6.20}$$

where the chemical potential μ is given by the first variation of F,

$$\mu = f'(\phi) - \nabla \cdot \left[|\varepsilon(\vec{n}) \nabla \phi| \vec{\xi} \right] + \delta^2 \nabla^2 (\nabla^2 \phi). \tag{6.21}$$

The vector $\vec{\xi}$ is the Cahn-Hoffman ξ-vector specified by Eq. 6.13.

6.3 Analysis

This section consists of two parts, an analysis of the 1-D time-independent solution to Eqs. 6.20-6.21 (i.e., a planar interface at equilibrium) and an asymptotic analysis of Eqs. 6.20-6.21. The 1-D analysis details the effect of the regularization on the interfacial energy, and its principal result is a modified ξ-vector that includes the effect of the regularization, denoted by $\vec{\Xi}$, The asymptotic analysis shows that the model has the correct [160] Gibbs-Thomson condition for the new ξ-vector,

$$\mu = \frac{\nabla_s \cdot \Xi}{(X_\beta - X_\alpha)}, \tag{6.22}$$

and that the behavior in the bulk is unaffected by the regularization to at least second order in the interfacial width.

6.3.1 Planar Interface

Before we begin the asymptotic analysis, it will be useful to first consider the problem of a planar interface at equilibrium. This interface $\phi(x)$ minimizes the functional $\Gamma[\phi, \nabla\phi, \nabla^2\phi]$,

$$\Gamma = \int_{-\infty}^{+\infty} \left(f(\phi) + \frac{1}{2}\varepsilon^2\phi_x^2 + \frac{\delta^2}{2}\phi_{xx}^2 \right) dx, \tag{6.23}$$

which describes the energy of the interface.

We introduce $\zeta = \sqrt{\delta}$ as the interfacial width parameter. Using a scaled spatial coordinate $z = \zeta x$ and scaled anisotropy $\tilde{\varepsilon} = \varepsilon/\zeta$, Eq. 6.23 becomes

$$\Gamma = \zeta \int_{-\infty}^{+\infty} \left(f(\phi) + \frac{1}{2}\varepsilon^2\phi_z^2 + \frac{1}{2}\phi_{zz}^2 \right) dz, \tag{6.24}$$

where subscripts by z denote the partial derivatives $\phi_z = \partial\phi/\partial z$, $\phi_{zz} = \partial^2\phi/\partial z^2$, etc.

Denoting the integrand in Eq. 6.24 by $\mathscr{L}(\phi, \phi_z, \phi_{zz})$, the Euler-Lagrange equation for this system is [169]

$$0 = \frac{\partial\mathscr{L}}{\partial\phi} - \frac{d}{dz}\frac{\partial\mathscr{L}}{\partial\phi_z} + \frac{d^2}{dz^2}\frac{\partial\mathscr{L}}{\partial\phi_{zz}} \tag{6.25}$$

which upon evaluation results in

$$0 = f'(\phi) - \tilde{\varepsilon}^2\phi_{zz} + \phi_{zzzz}, \tag{6.26}$$

which is simply the 1-D expression for chemical potential, Eq. 6.21, with $\mu = 0$.

An alternative form of the Euler-Lagrange equation can be used to derive a relationship between the terms in Eq. 6.24. The following equation is equivalent to Eq. 6.25 [64, 169],

$$0 = \frac{d}{dz}\left(\mathscr{L} - \phi_z\frac{\partial\mathscr{L}}{\partial\phi_z} - \phi_{zz}\frac{\partial\mathscr{L}}{\partial\phi_{zz}} + \phi_z\frac{d}{dz}\frac{\partial\mathscr{L}}{\partial\phi_{zz}} \right). \tag{6.27}$$

Integrating this equation in z gives

$$\text{const.} = \mathscr{L} - \phi_z \frac{\partial \mathscr{L}}{\partial \phi_z} - \phi_{zz} \frac{\partial \mathscr{L}}{\partial \phi_{zz}} + \phi_z \frac{d}{dz} \frac{\partial \mathscr{L}}{\partial \phi_{zz}}, \tag{6.28}$$

We expect that $\mathscr{L}$, ϕ_z, and ϕ_{zz} all go to zero as $z \to \infty$. Thus the constant of integration must be zero [64]. Substituting $\mathscr{L}$ from Eq. 6.24 gives

$$0 = f(\phi) - \frac{1}{2}\tilde{\varepsilon}^2 \phi_z^2 - \frac{1}{2}\phi_{zz}^2 + \phi_z \phi_{zzz}. \tag{6.29}$$

Substituting for $f(\phi)$ in Eq. 6.24 gives the following expression for the interfacial energy:

$$\Gamma = \zeta \int_{-\infty}^{+\infty} \left(\tilde{\varepsilon}^2 \phi_z^2 + \phi_{zz}^2 - \phi_z \phi_{zzz} \right) dz. \tag{6.30}$$

The $\phi_z \phi_{zzz}$ term can be integrated by parts, noting that $\phi_z \to 0$ as $z \to \infty$, leaving the final expression

$$\Gamma = \zeta \int_{-\infty}^{+\infty} \left(\tilde{\varepsilon}^2 \phi_z^2 + 2\phi_{zz}^2 \right) dz, \tag{6.31}$$

as a simplified form of the interfacial energy.

For the next subsection, we also need to know the effect of $\tilde{\varepsilon}$ on Γ, i.e., the effect of the input anisotropy function on the 'output' interfacial energy of the model. Evaluating $\partial\Gamma/\partial\tilde{\varepsilon}$ with Γ defined as in Eq. 6.24 yields

$$\frac{\partial \Gamma}{\partial \tilde{\varepsilon}} = \zeta \int_{-\infty}^{+\infty} \left(f'(\phi) \frac{\partial \phi}{\partial \tilde{\varepsilon}} + \tilde{\varepsilon} (\phi_z)^2 + \tilde{\varepsilon}^2 \phi_z \frac{\partial^2 \phi}{\partial \tilde{\varepsilon} \partial z} + \phi_{zz} \frac{\partial^3 \phi}{\partial \tilde{\varepsilon} \partial z^2} \right) dz, \tag{6.32}$$

and by integrating by parts we arrive at

$$\frac{\partial \Gamma}{\partial \tilde{\varepsilon}} = \zeta \tilde{\varepsilon} \int_{-\infty}^{+\infty} (\phi_z)^2 dz + \zeta \int_{-\infty}^{+\infty} \left(f'(\phi) - \tilde{\varepsilon}^2 \phi_{zz} + \phi_{zzzz} \right) \frac{\partial \phi}{\partial \tilde{\varepsilon}} dz. \tag{6.33}$$

Comparing the second integral to Eq. 6.25 we note that it equals zero, leaving

$$\frac{\partial \Gamma}{\partial \tilde{\varepsilon}} = \zeta \tilde{\varepsilon} \int_{-\infty}^{+\infty} (\phi_z)^2 dz \tag{6.34}$$

We can use Eqs. 6.31 and 6.25 to define the Ξ-vector, which follows the general definition of the Cahn-Hoffman ξ-vector [159, 160] and uses the homogeneous extension $\Gamma_{ext}(\nabla\phi) = |\nabla\phi|\Gamma(\vec{n})$:

$$\Xi_i = \frac{\partial \left(\Gamma\left[(\tilde{\varepsilon}(\vec{n})\right]|\nabla\phi|\right)}{\partial \nabla_i \phi} = \Gamma \frac{\partial |\nabla\phi|}{\partial \nabla\phi} + |\nabla\phi| \frac{\partial \Gamma}{\partial \tilde{\varepsilon}} \frac{\partial \tilde{\varepsilon}}{\partial \vec{n}} \frac{\partial \vec{n}}{\partial \nabla\phi} \tag{6.35}$$

Noting that $\partial|\nabla\phi|/\partial\nabla_i\phi = n_i$ and

$$\frac{\partial n_i}{\partial \nabla_j \phi} = \frac{1}{|\nabla\phi|}(\delta_{ij} - n_i n_j), \tag{6.36}$$

Eq. 6.35 can also be written as

$$\Xi_i = \Gamma n_i + \sum_j (\delta_{ij} - n_i n_j) \frac{\partial \Gamma}{\partial \tilde{\varepsilon}} \frac{\partial \tilde{\varepsilon}}{\partial n_j} = \frac{\partial \Gamma}{\partial \tilde{\varepsilon}} (\xi_i - \tilde{\varepsilon} n_i) + \Gamma n_i$$

This expression uses the ξ as defined in Eq. 6.13, which allows straightforward use of literature results in the next section.

6.3.2 Asymptotic Analysis

In this section, we analyze the phase field model defined in Eqs. 6.20-6.21 in the limit of an asymptotically thin interface [76, 170, 171, 172, 173]. As in the previous section, the interfacial width parameter is defined as $\zeta = \sqrt{\delta}$. The limit of interest is therefore $\zeta \to 0$. To obtain a balance between the gradient term and the regularization term, we assume that $\tilde{\varepsilon} = \varepsilon/\sqrt{\delta}$ is $\mathscr{O}(1)$ with respect to ζ, and the resulting equations are,

$$\frac{\partial \phi}{\partial t} = \nabla^2 \mu, \tag{6.37}$$

$$\mu = f'(\phi) - \zeta^2 \nabla \cdot \left[|\tilde{\varepsilon}(\vec{n}) \nabla \phi| \vec{\xi} \right] + \zeta^4 \nabla^2 (\nabla^2 \phi). \tag{6.38}$$

The approach of this type of analysis is to split the mathematical problem into two parts, an outer solution in which the terms containing ζ are treated as a regular perturbation [174], and an inner solution, located in a layer of thickness $\mathscr{O}(\zeta)$ about the interface, in which the interface normal coordinate is scaled by ζ so that all of the terms appear at leading order. These solutions are matched in successive orders of ζ, and the physics at the interface (i.e., Eqs. 2.31 and 2.39) are obtained from this matching process. Following Ref. [76], we consider behavior in a late timescale, $t_1 = t/\zeta$.

The variables of the outer solution are denoted by $\hat{\mu}$ and $\hat{\phi}$, and they are expanded in ζ as

$$\hat{\phi}(\vec{x}; t_1) = \hat{\phi}^{(0)}(\vec{x}; t_1) + \zeta \hat{\phi}^{(1)}(\vec{x}; t_1) + \zeta^2 \hat{\phi}^{(2)}(\vec{x}; t_1) ... \tag{6.39}$$

$$\hat{\mu}(\vec{x}; t_1) = \hat{\mu}^{(0)}(\vec{x}; t_1) + \zeta \hat{\mu}^{(1)}(\vec{x}; t_1) + \zeta^2 \hat{\mu}^{(2)}(\vec{x}; t_1) ... \tag{6.40}$$

where $\vec{x}$ are Cartesian coordinates. Following Ref. [76], we consider behavior in a late timescale, $t = \mathscr{O}(1/\zeta)$, and the governing equations for the outer solution are

$$0 = \nabla^2 \hat{\mu}, \tag{6.41}$$

to all orders, and

$$\hat{\mu}^{(0)} = f' \left(\hat{\phi}^{(0)} \right), \tag{6.42}$$

at leading order, $\mathscr{O}(1)$, and

$$\hat{\mu}^{(1)} = f'' \left(\hat{\phi}^{(0)} \right) \phi^{(1)}, \tag{6.43}$$

at first order, $\mathscr{O}(\zeta)$. These equations are unchanged from Ref. [76]. The anisotropic term and regularization term therefore do not affect the governing equations for the outer solution to the orders we consider. Their effect is limited to the boundary conditions of the outer solution at the interface, which are obtained by matching to the inner solution.

The behavior of the inner solution is governed by Eqs. 6.37 and 6.38 expressed in local orthogonal coordinates at the interface $(\vec{s}, z)$, where $\vec{s}$ are the surface coordinates and z is a scaled normal coordinate $z = \rho/\zeta$, where ρ is the signed distance from the interface. The inner solution will be denoted by μ and ϕ, and is also expanded in ζ as

$$\phi(\vec{s}, z; t_1) = \phi^{(0)}(\vec{s}, z; t_1) + \zeta\phi^{(1)}(\vec{s}, z; t_1) + \zeta^2\phi^{(2)}(\vec{s}, z; t_1)... \tag{6.44}$$

$$\mu(\vec{s}, z; t_1) = \mu^{(0)}(\vec{s}, z; t_1) + \zeta\mu^{(1)}(\vec{s}, z; t_1) + \zeta^2\mu^{(2)}(\vec{s}, z; t_1)... \tag{6.45}$$

With $\vec{x}_0$ and $\vec{s}_0$ denoting the same point on the interface in Cartesian and surface coordinates, respectively, the matching conditions correspond to the limit $z \to \infty$ at successive orders of ζ [172],

$$\mu^{(0)}(\vec{s}_0, \pm\infty; t_1) = \hat{\mu}^{(0)}(\vec{x}_0\pm; t_1), \tag{6.46}$$

$$\mu^{(1)}(\vec{s}_0, \pm\infty; t_1) = \hat{\mu}^{(1)}(\vec{x}_0\pm; t_1) + \hat{\mu}^{(0)}(\vec{x}_0\pm; t_1) + \mathscr{O}(1) \tag{6.47}$$

The Laplacian in the inner coordinates is [76, 172],

$$\nabla^2 = \frac{1}{\zeta^2}\frac{\partial^2}{\partial z^2} + 2\frac{1}{\zeta}H\frac{\partial}{\partial z} + \mathscr{O}(1), \tag{6.48}$$

and therefore the biharmonic operator $\nabla^2\nabla^2$ is,

$$\nabla^2\nabla^2 = \frac{1}{\zeta^4}\frac{\partial^4}{\partial z^4} + 4\frac{1}{\zeta^3}H\frac{\partial^3}{\partial z^3} + \mathscr{O}(1/\zeta^2). \tag{6.49}$$

The first two orders of the anisotropic divergence $\zeta^2\nabla\cdot(|\tilde{\varepsilon}(\vec{n})\nabla\phi|\vec{\xi})$ are given by [175],

$$\zeta^2\nabla\cdot(|\tilde{\varepsilon}\nabla\phi|\vec{\xi}) = \tilde{\varepsilon}^2\phi_{zz}^{(0)} + \zeta\tilde{\varepsilon}^2\phi_{zz}^{(1)} + \zeta\left(\tilde{\varepsilon}\vec{\xi}\cdot\nabla_s\phi_z^{(0)} + \nabla_s\cdot\tilde{\varepsilon}\vec{\xi}\phi_z^{(0)}\right) + \mathscr{O}(\zeta^2) \tag{6.50}$$

where $\tilde{\varepsilon}$ and $\vec{\xi}$ make use of the leading order interface normal vector.

Leading order

In the interface coordinates, Eqs. 6.20 and 6.21 become, at leading order in ζ,

$$0 = \mu_{zz}^{(0)} \tag{6.51}$$

and

$$\mu^{(0)} = f'(\phi^{(0)}) - \tilde{\varepsilon}^2 \phi_{zz}^{(0)} + \phi_{zzzz}^{(0)} \tag{6.52}$$

respectively. The leading order matching condition is [172],

$$\mu^{(0)}(\vec{s}, \pm\infty; t_1) = \hat{\mu}^{(0)}(\vec{s}, \pm 0; t_1), \tag{6.53}$$

where $\hat{\mu}^{(0)}(\vec{s}, \pm 0; t_1)$ is the outer solution on either side of the interface at the point $\vec{s}$. It will be abbreviated as $\hat{\mu}^{(0)}(\pm 0)$.

Integrating Eq. 6.51 by z twice and using this matching condition leads to

$$\hat{\mu}^{(0)}(\pm 0) = f'(\phi^{(0)}) - \tilde{\varepsilon}^2 \phi_{zz}^{(0)} + \phi_{zzzz}^{(0)} \tag{6.54}$$

Adapting the treatment of [76] for the outer solution, which as we have noted is unchanged by the Laplacian-squared regularization, the chemical potential $\hat{\mu}^(0)$ will be at equilibrium (i.e., zero) everywhere by this timescale. Based on Eq. 6.42, $\hat{\phi}^{(0)}$ is constant at its equilibrium values in each phase. The problem in Eq. 6.54 is therefore exactly the 1-D planar interface at equilibrium considered in the previous section.

First order

At first order in the expansion, Eq. 6.37 becomes

$$0 = \mu_{zz}^{(1)} + 2H\mu_z^{(0)}, \tag{6.55}$$

where the $\mu_z^{(0)}$ term disappears because $\mu^{(0)}$ is constant. Eq. 6.38 becomes,

$$\mu^{(1)} = f''(\phi^{(0)})\phi^{(1)} - \tilde{\varepsilon}^2\phi_{zz}^{(1)} + \phi_{zzzz}^{(1)} - \left(\tilde{\varepsilon}\vec{\xi}\cdot\nabla_s\phi_z^{(0)} + \nabla_s\cdot\tilde{\varepsilon}\vec{\xi}\phi_z^{(0)}\right) + 4H\phi_{zzz}^{(0)}, \tag{6.56}$$

The matching condition at this order is [172]

$$\mu^{(1)}(\vec{s},z;t_1) = \hat{\mu}^{(1)}(\pm 0) + z\hat{\mu}_z^{(0)}(\vec{s},\pm 0;t_1) + \mathscr{O}(1) \text{ as } z\to\pm\infty, \tag{6.57}$$

although again the $\hat{\mu}_z^{(0)}(\pm 0)$ term disappears as $\hat{\mu}^{(0)}(\pm 0)$ is constant. Integrating Eq. 6.55 twice and applying the matching condition yields

$$\hat{\mu}^{(1)}(\pm 0) = f''(\phi^{(0)})\phi^{(1)} - \tilde{\varepsilon}^2\phi_{zz}^{(1)} + \phi_{zzzz}^{(1)} - \left(\tilde{\varepsilon}\vec{\xi}\cdot\nabla_s\phi_z^{(0)} + \nabla_s\cdot\tilde{\varepsilon}\vec{\xi}\phi_z^{(0)}\right) + 4H\phi_{zzz}^{(0)}, \tag{6.58}$$

Multiplying both sides by $\phi_z^{(0)}$ and integrating over $(-\infty,\infty)$ eliminates the $\phi^{(1)}$ terms, yielding the solvability condition [172]

$$\hat{\mu}^{(1)}(\pm 0)\int_{-\infty}^{+\infty}\phi_z^{(0)}dz = -\int_{-\infty}^{+\infty}\phi_z^{(0)}\left(\tilde{\varepsilon}\vec{\xi}\cdot\nabla_s\phi_z^{(0)} + \nabla_s\cdot\tilde{\varepsilon}\vec{\xi}\phi_z^{(0)} - 4H\phi_{zzz}^{(0)}\right)dz, \tag{6.59}$$

The LHS of this equation is simply $\hat{\mu}^{(1)}(\pm 0)\phi^{(0)}|_{-\infty}^{+\infty}$, and the remainder of this subsection will consist of reducing the RHS of Eq. 6.59 to a form that allows substitution of $\vec{\Xi}$ from Eq. 6.3.1. Application of identities of vector calculus and integration of the $\phi_{zzz}^{(0)}$ term by parts yields

$$RHS = -\int_{-\infty}^{+\infty}\left[\nabla_s\cdot\tilde{\varepsilon}\vec{\xi}\left(\phi_z^{(0)}\right)^2 + 4H\left(\phi_{zz}^{(0)}\right)^2\right]dz. \tag{6.60}$$

Substituting $2H\left(\phi_{zz}^{(0)}\right)^2 = \nabla_s\cdot\left(\phi_{zz}^{(0)}\right)^2\vec{n}$, the RHS can be re-expressed as

$$RHS = -\nabla_s\cdot\int_{-\infty}^{+\infty}\left[\tilde{\varepsilon}\vec{\xi}\left(\phi_z^{(0)}\right)^2 + 2\vec{n}\left(\phi_{zz}^{(0)}\right)^2\right]dz. \tag{6.61}$$

Note that the identity $2H = \nabla_s\cdot\vec{n}$ was introduced with the opposite sign in Chapter 2; the current

sign represents the convention in Ref. [176]. Using the expression for the modified interfacial energy Γ (Eq. 6.31) to substitute for the $\phi_{zz}^{(0)}$ term in Eq. 6.61 results in

$$RHS = -\nabla_s \cdot \left[\left(\tilde{\varepsilon}\vec{\xi}\,\zeta - \vec{n}\frac{\tilde{\varepsilon}^2}{\zeta} \right) \int_{-\infty}^{+\infty} \left(\phi_z^{(0)} \right)^2 dz + \frac{1}{\zeta}\vec{n}\Gamma \right], \tag{6.62}$$

Using the expression for $\partial\Gamma/\partial\tilde{\varepsilon}$ (Eq. 6.34) to substitute for the $\phi_z^{(0)}$ term, we have

$$RHS = -\frac{1}{\zeta}\nabla_s \cdot \left[\frac{\partial\Gamma}{\partial\tilde{\varepsilon}} \left(\vec{\xi} - \vec{n}\tilde{\varepsilon} \right) + \vec{n}\Gamma \right] \tag{6.63}$$

Recalling Eq. 6.35, this is exactly $-\frac{1}{\zeta}\nabla_s \cdot \Xi$, and the complete solvability condition (simplified from Eq. 6.59) is,

$$\hat{\mu}^{(1)}(\pm 0) = -\frac{1}{\zeta}\frac{\nabla_s \cdot \Xi}{\phi^{(0)}\big|_{-\infty}^{+\infty}}. \tag{6.64}$$

This is the correct form of the Gibbs-Thomson equation expressed with the Cahn-Hoffman ξ-vector [160]. We could proceed to derive the equation for interfacial motion (Eq. 2.39), but it is unchanged from Ref. [76], and therefore we conclude our analysis at this point.

6.4 Equilibrium shapes

This section compares phase field simulations to equilibrium shapes predicted for the modified interfacial energy Γ. The phase field method, a conservative Allen-Cahn equation, is introduced first, followed by methods for calculating equilibrium shapes with and without the effect of the regularization. Finally, comparisons are made between particle shapes and the shapes of the diffuse corners predicted by the sharp interface theory and simulated using the phase field method.

6.4.1 Phase field method

To reduce the computation time needed for convergence to the equilibrium shape, a globally conservative Allen-Cahn equation was employed in place of the (locally conservative) regularized

anisotropic Cahn-Hilliard equation (Eqs. 6.20-6.21). This method minimizes the free energy energy in Eq. 6.16 [177], and a Lagrange multiplier is used to enforce global conservation of ϕ, i.e.,

$$\int_\Omega \frac{\partial \phi}{\partial t} dV = 0 \tag{6.65}$$

The globally conserved Allen-Cahn equation with regularized strong anisotropy is,

$$\frac{\partial \phi}{\partial t} = -M\left(f'(\phi) + \lambda - \nabla \cdot \left[|\varepsilon(\vec{n})\nabla\phi|\vec{\xi}\right] + \delta^2 \nabla^2(\nabla^2\phi)\right), \tag{6.66}$$

where λ is the Lagrange multiplier, and following [177], $\lambda = \int_\Omega f'(\phi) dV$. Finite differences discretization of Eq. 6.66 requires a centered difference of the anisotropic divergence $\nabla \cdot \left[|\varepsilon\nabla\phi|\vec{\xi}\right]$, an example of which can be found in Ref. [134]. The present work improves upon their technique by using isotropic stencils, which were derived following the methodology in Ref. [178]. Time discretization consisted of a forward Euler scheme.

An equilibrium shape simulation consisted of a single, initially circular particle centered a cubic domain with periodic boundary conditions. Bulk free energy was $f(\phi) = \frac{1}{4}\phi^2(1-\phi)^2$, and a simple four-fold anisotropy was used [134, 142],

$$\varepsilon(\vec{n}) = 1 + a\left[4(n_1^4 + n_2^4 + n_3^4) - 3\right]. \tag{6.67}$$

The particle was initialized as a circle with a diffuse interface,

$$\phi(\vec{x}) = \frac{1}{2}\left[1 + \tanh\left(\frac{|\vec{x} - \vec{x}_0| - r}{2}\right)\right]. \tag{6.68}$$

The particles had initial radius $r = 80$ and the size of the domain was $L_x = L_y = 256$. Grid spacing was $\Delta x = 0.5$, and timestep was $\Delta t = 0.008$ for $\delta = 1$ and $\Delta t = 0.004$ for $\delta = 2$, the two regularizations considered. Comparisons to the sharp interface predictions were made using the $\phi = 0.5$ isocontour.

6.4.2 Sharp interface predictions

Equilibrium shapes were calculated in 2-D incorporating the effect of regularization both at the regularized corner [59] and far away from it. We will describe the methods for calculating equilibrium shapes in three stages: calculation of the non-regularized equilibrium shape (the Wulff shape), calculation of the Wulff shape for the modified interfacial energy Γ, and calculation of the equilibrium shape with the asymptotic solution for the regularized corner shape [59] and the modified interfacial energy. The shapes are parametrized by the orientation angle θ. In terms of θ, the anisotropy in Eq. 6.67 is,

$$\gamma = 1 + a\cos 4\theta. \tag{6.69}$$

Arc length of the Wulff shape was calculated by integration [59] of

$$s = \int_0^\theta \left[\gamma(\theta) + \gamma''(\theta)\right], d\theta, \tag{6.70}$$

and the x and y coordinates of the Wulff shape were determined by the integrations

$$x = \int_0^s \cos(\theta) ds, \tag{6.71}$$

$$y = -\int_0^s \sin(\theta) ds, \tag{6.72}$$

which result in the analytical expressions

$$x = \gamma'(\theta)\cos(\theta) + \gamma(\theta)\sin(\theta), \tag{6.73}$$

$$y = -\gamma'(\theta)\sin(\theta) + \gamma(\theta)\cos(\theta). \tag{6.74}$$

For strong anisotropy, this construction results in non-physical lobes in the Wulff shape, which are illustrated in Fig. 6.1. Unstable orientations satisfy $\gamma + \gamma'' < 0$. When γ is symmetric about the reference orientation (as in Eq. 6.69), the critical angle θ_c between stable and metastable orientations

is the solution [59] to

$$\tan(\theta_c) + \frac{\gamma'(\theta_c)}{\gamma(\theta_c)} = 0. \tag{6.75}$$

The physical equilibrium shape results from truncation of the lobes from the Wulff shape [151], and here it was calculated piecewise: $s(\theta)$ was calculated using Eq. 6.70 on the intervals $[-\frac{\pi}{4}, -\theta_c]$ $[\theta_c, \frac{\pi}{4}]$. These segments were joined at the point corresponding to the sharp corner, and their rotations provided the rest of the equilibrium shape since $\gamma(\theta)$ has four-fold symmetry. This is the first type of sharp interface prediction we will compare to phase field simulations, and it does not include any effect of the regularization.

The effect of the regularization on the interfacial energy away from corners was considered first. This effect was the topic of Section 6.3.1, and the interfacial energy Γ was found to depend on a single parameter, $\tilde{\varepsilon} = \varepsilon/\sqrt{\delta}$. This dependence was evaluated numerically by solving Eq. 6.66 in one dimension, and the resulting plot of normalized interfacial energy including the regularization, Γ/γ_0, vs. $\tilde{\varepsilon}$ is shown in Fig. 6.3. At $\tilde{\varepsilon} = 0$, this energy is entirely due to the Laplacian-squared regularization, representing the limit $\delta \to \infty$ or $\varepsilon \to 0$. As $\tilde{\varepsilon}$ increases, Γ/γ_0 converges towards it, such that the effect of the regularization is a small part of the overall interfacial energy by $\tilde{\varepsilon} = 2$.

To determine the equilibrium shape using the regularized interfacial energy, values of $\Gamma(\theta)$ were calculated from the data in Fig. 6.3 by interpolation, and its derivatives $\Gamma'(\theta)$, and $\Gamma''(\theta)$ were calculated using finite differences. The critical angle θ_c was recalculated by using Eq. 6.75 with $\Gamma(\theta)$ and $\Gamma'(\theta)$, and the equilibrium shape was calculated using Eqs. 6.70-6.72. This is the second type of equilibrium shape we compare to simulations, in which the effect of regularization is taken into account in the interfacial energy, but the corner shape is not regularized.

Spencer [59] provides a method for determining the shape of the regularized corner. Considering θ and s related by Eq. 6.70, the effect of the regularization is to modify θ by

$$\theta_{reg}(s) = \theta(s) \pm \theta_c \exp\left(\pm \lambda s/\beta^{1/2}\right), \tag{6.76}$$

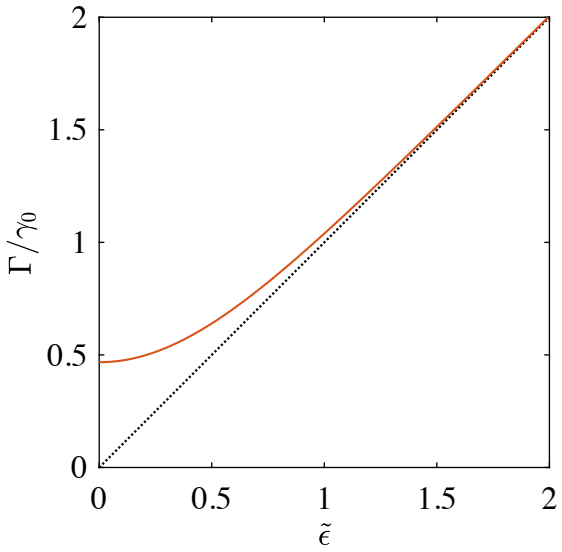

Figure 6.3: Plot of normalized interfacial energy Γ/γ_0 (red line) as a function of the scaled anisotropy function $\tilde{\varepsilon} = \varepsilon/\sqrt{\delta}$. This relationship is universal for a given $f(\phi)$. The black dotted line indicates the unregularized case, $\Gamma/\gamma_0 = \tilde{\varepsilon}$.

where

$$\lambda = \sqrt{\Gamma''(\theta_c) - \cos(\theta_c)\left[\Gamma'(\theta_c)\sin(\theta_c) - \Gamma(\theta_c)\cos(\theta_c)\right]}, \tag{6.77}$$

and $\beta^{1/2}$ is the regularization parameter $\sqrt{\delta\pi/A}$, where A is the particle area. For agreement between the predicted and simulated shapes, this area must correspond to the particle area, which was calculated from the $\phi = 0.5$ isocontour using Green's theorem,

$$A = \frac{1}{2}\int_C \left(x\frac{dy}{ds} - y\frac{dx}{ds}\right) ds. \tag{6.78}$$

The predicted shape was then scaled to have the same area as the $\phi = 0.5$ isocontour and centered in the simulation domain. The predicted shape with the regularized corner (i.e., using Eq. 6.76) was used to set the area for scaling for the other predicted shapes.

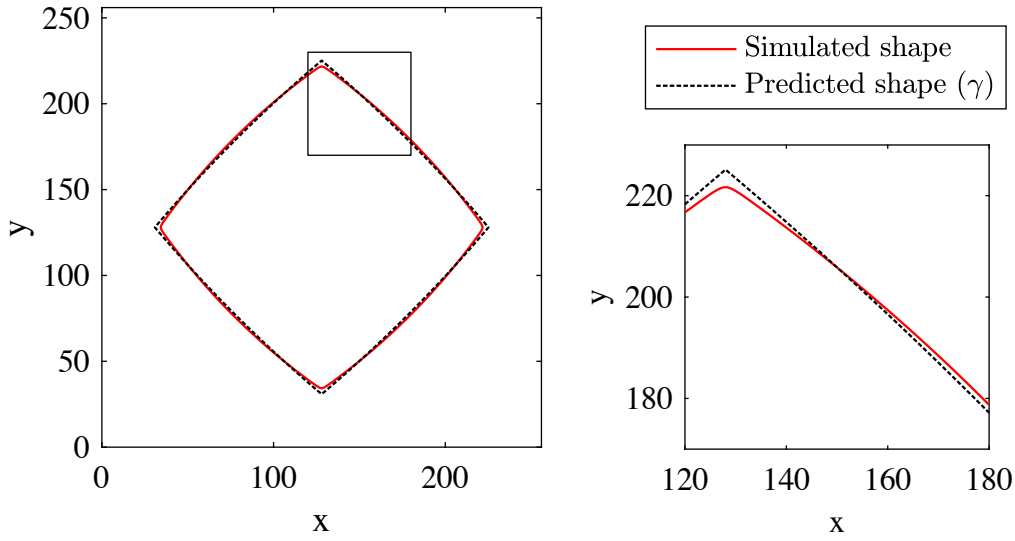

Figure 6.4: Comparison of a simulated equilibrium shape (red line) and the Wulff shape calculated without considering any effect of the regularization (black line) for $a = 0.4$, $\delta = 2$.

6.4.3 Results

A comparison between the phase field simulation and the Wulff shape without including the effect of the regularization is depicted in Fig. 6.4, with parameters $a = 0.4$ and $\delta = 2$. The simulation deviates from the predicted shape both at the corner and far away from it. In Fig. 6.5, the same condition ($a = 0.4$, $\delta = 2$) is compared to the sharp interface prediction for Γ, the modified interfacial energy, and much better agreement is obtained. This demonstrates the effect of the regularization on the effective interfacial energy Γ. A regularization-dependent change in the equilibrium shape was found in previous studies [134, 135], but now we have verified the mechanism for this effect.

The corner shapes are compared between simulations and sharp interface predictions in Fig. 6.6a-c. While it has not been rigorously demonstrated that the Laplacian-squared regularization should act in the same way as the κ^2 regularization (Eq. 6.5), we nevertheless find very good agreement between simulations and predictions. This agreement holds over a range of anisotropies and regularizations, with better agreement for relatively weaker anisotropy and stronger regularization (i.e., Fig. 6.6b, with $a = 0.2$ and $\delta = 2$). The particle shapes themselves are shown in Fig. 6.6a-c, and good agreement between the predictions and simulations is found in all cases.

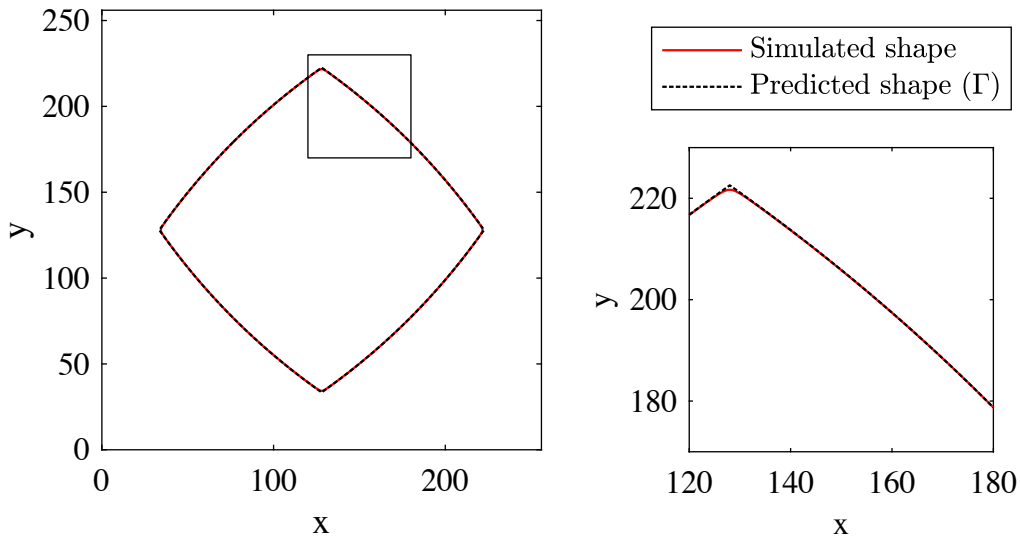

Figure 6.5: Comparison of a simulated equilibrium shape (red line) and the Wulff shape calculated using $\Gamma(\theta)$, the interfacial energy modified by the regularization, (black line) for $a = 0.4$, $\delta = 2$.

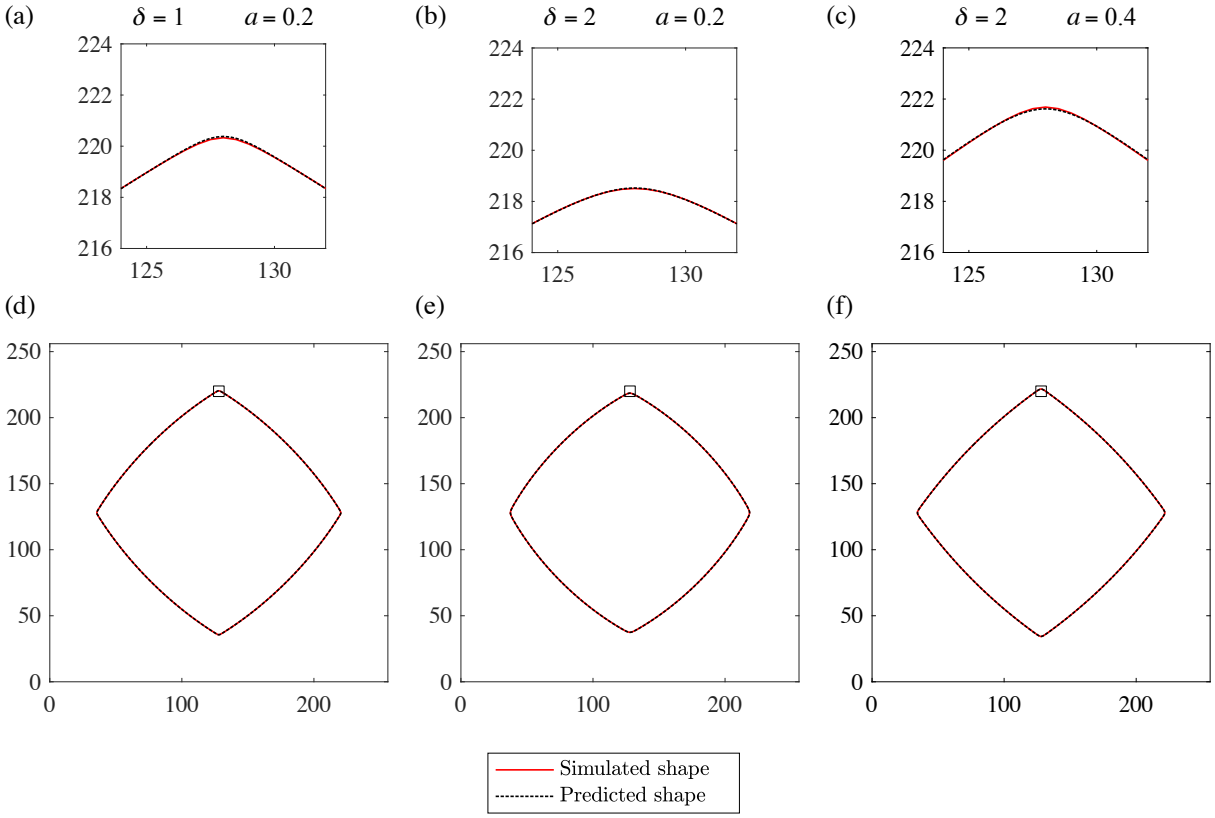

Figure 6.6: Comparison of simulated equilibrium shapes (red lines) and the regularized Wulff shape calculated using $\Gamma(\theta)$ (black dashed lines) at the corner (a-c) and for the entire particle (d-e) at $a = 0.2$, $\delta = 1$ (a,d); $a = 0.2$, $\delta = 1$ (b,e); and $a = 0.4$, $\delta = 2$ (c,f).

6.5 Conclusions

This chapter examined a phase field method for evolution via bulk diffusion when strong anisotropy is present, which occurs in solid-solid [162] and solid-liquid [46, 168] systems. This model, the strongly anisotropic Cahn-Hilliard equation with the Laplacian-squared regularization, does not change the kinetics or thermodynamics of the bulk phase, and it smooths out the sharp corners that are characteristic of strong anisotropy. However, results in this chapter show that it does affect interfacial energy. A planar interface at equilibrium was examined in Section 6.3.1. The interfacial energy was found to be affected by the regularization, and a Cahn-Hoffman $\boldsymbol{\xi}$-vector was derived for the modified interfacial energy. In Section 6.3.2, asymptotic analysis of the phase field model found that it incorporates the correct Gibbs-Thomson condition for the modified Ξ-vector. Equilibrium shapes simulated with the phase field model were compared to predictions based on the results of the analysis. Excellent agreement was obtained for the particle shapes away from the regularized corners, confirming the analysis. Simulated corner shapes were found to agree with sharp interface predictions for the curvature-squared regularization. These results provide a fundamental understanding of the strongly anisotropic Cahn-Hilliard equation with the Laplacian-squared regularization, which will help users of this model determine the effect of the regularization on interfacial energy, whether it is small enough to be neglected, and how to parametrize their interfacial energy to simulate the desired dynamics. This will enable simulations of coarsening and microstructural evolution in strongly anisotropic systems.

Chapter 7

Coarsening with inactive length scales

7.1 Introduction

Two-phase mixtures, from metallic alloys to islands on surfaces, undergo coarsening wherein the total interfacial area of the system decreases with time. Theory predicts that during coarsening the average size-scale of a two-phase mixture increases with time as $t^{1/3}$ when the two-phase mixture is self-similar, or time independent when scaled by a time-dependent length. However, in many cases a classical $t^{1/3}$ power law for the average size scale of a two-phase mixture is observed without a self-similar two-phase morphology [40, 43, 84, 85, 95]. The most striking example is given by Marsh and Glicksman [40] who show that even though a structure evolves in a non-self-similar fashion from a dendritic morphology to a polydisperse array of approximately spherical particles, the characteristic length scale of the two-phase system still increases as $t^{1/3}$.

Here, we explain why this temporal power law is so robustly observed even when the microstructure is not self-similar. We show that there exists an upper limit to the length scales in the system that are kinetically active during coarsening, which we term the self-similar length scale. Length scales smaller than the self-similar length scale evolve, leading to the classical temporal power law for the coarsening dynamics of the system. Longer length scales are largely inactive, leading to a non-self-similar structure. This result holds for any two-phase mixture with a large

distribution of morphological length scales.

7.2 Results

To examine the existence of inactive length scales in coarsening and to illustrate that the conclusions are not limited to dendritic structures, we simulate coarsening of a simpler, two-dimensional microstructure containing second-phase particles with a bimodal particle size distribution. The two modes of this distribution correspond to populations of large and small particles, where the difference in radii is sufficiently large such that the large particles may be inactive. Comparing the overall evolution of this system to the evolution of each population of particles should test the hypothesis of inactive length scales. This initial microstructure is shown in Fig. 7.1, and details regarding its generation are provided in the following section.

Coarsening of the structure was simulated using the Cahn-Hilliard equation (Eq. 3.4) with periodic boundary conditions. The evolution of the structure is depicted in Figs. 7.2-7.4. The small particles have coarsened, either growing or shrinking and disappearing, and are substantially fewer in number at later times (Figs.7.3 and 7.4). The large particles have grown at the expense of their smaller neighbours. Time evolution of the characteristic length, S_v^{-1}, is shown in Fig. 7.5, and S_v^{-1} increases from 47.2 to 101.5 over the course of the simulation. The fit to the power law given by Eq. 4.3 is $S_V^{-3}(t) = 1.31t + 9.66 \times 10^4$, which determines the initial time t_0 in Fig. 7.5 as $t_0 = -S_v^{-3}(t_0)/k = -7.39 \times 10^4$. While some deviation is apparent at early times, we find excellent agreement overall between the evolution of characteristic length and the expected coarsening power law, and the coefficient of determination of the fit is $R^2 = 0.9995$.

The temporal evolution of the morphology is described quantitatively in Figs. 7.6 and 7.7. Fig. 7.6 depicts distributions of interfacial radius of curvature, $R = 1/\kappa$, scaled by the characteristic length S_V^{-1}. Fig. 7.7 depicts the distributions of unscaled interfacial radius of curvature. These distributions are weighted by interfacial length and normalized. Therefore, they represent the probability that a point on the interface has a particular (scaled or unscaled) radius of curvature.

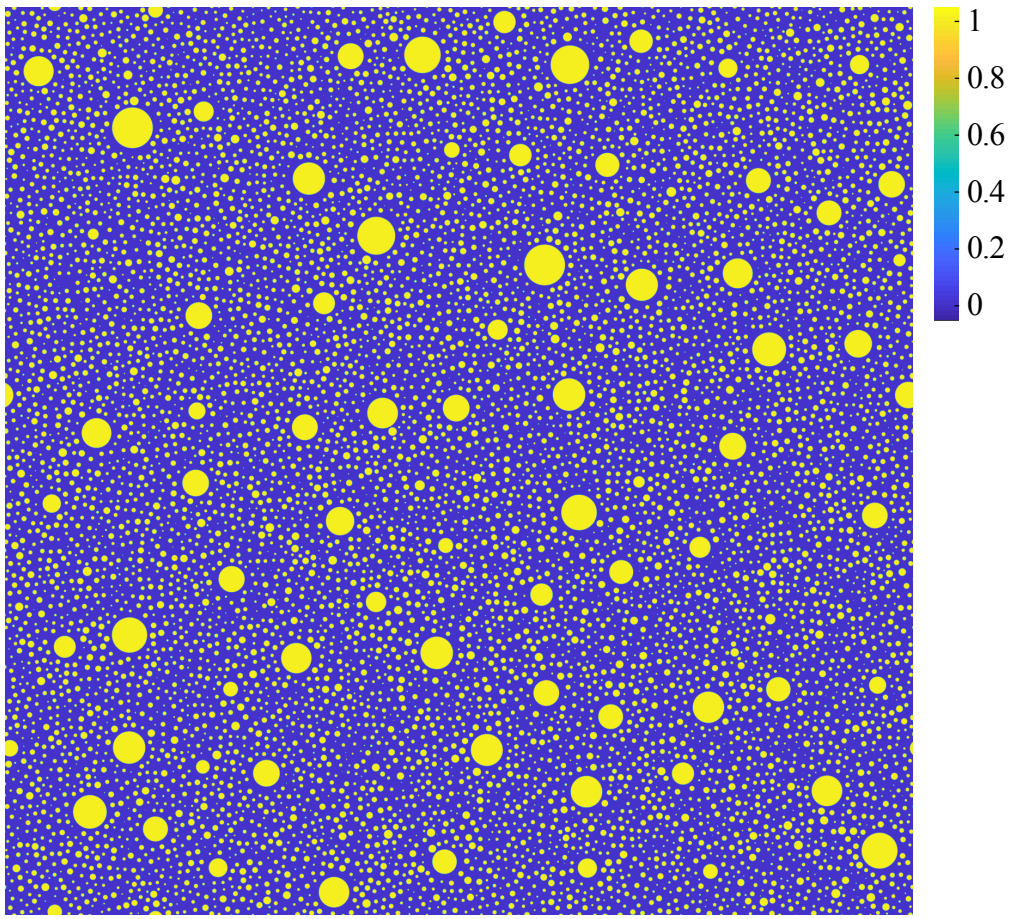

Figure 7.1: 2-D initial condition (order parameter) for the phase field simulation of coarsening with a bimodal initial particle size distribution.

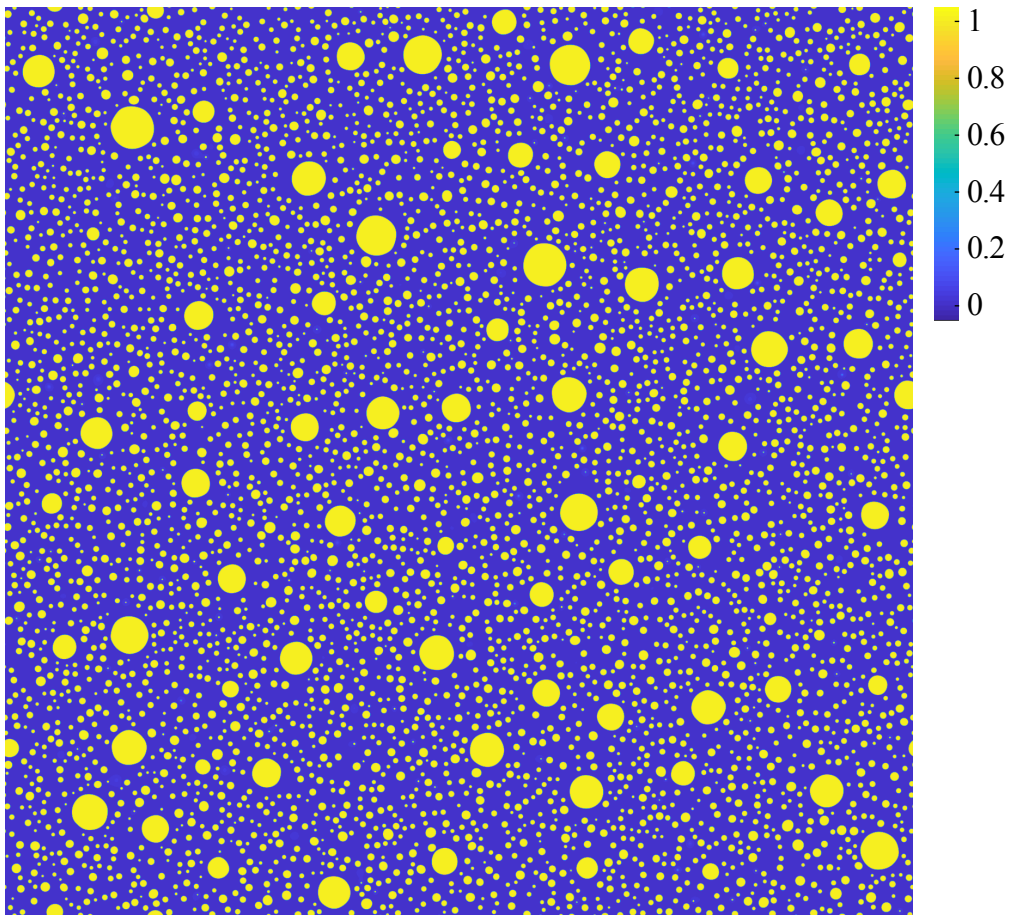

Figure 7.2: Order parameter at time $t = 1.4 \times 10^5$ during the simulation of coarsening with an initially bimodal particle size distribution.

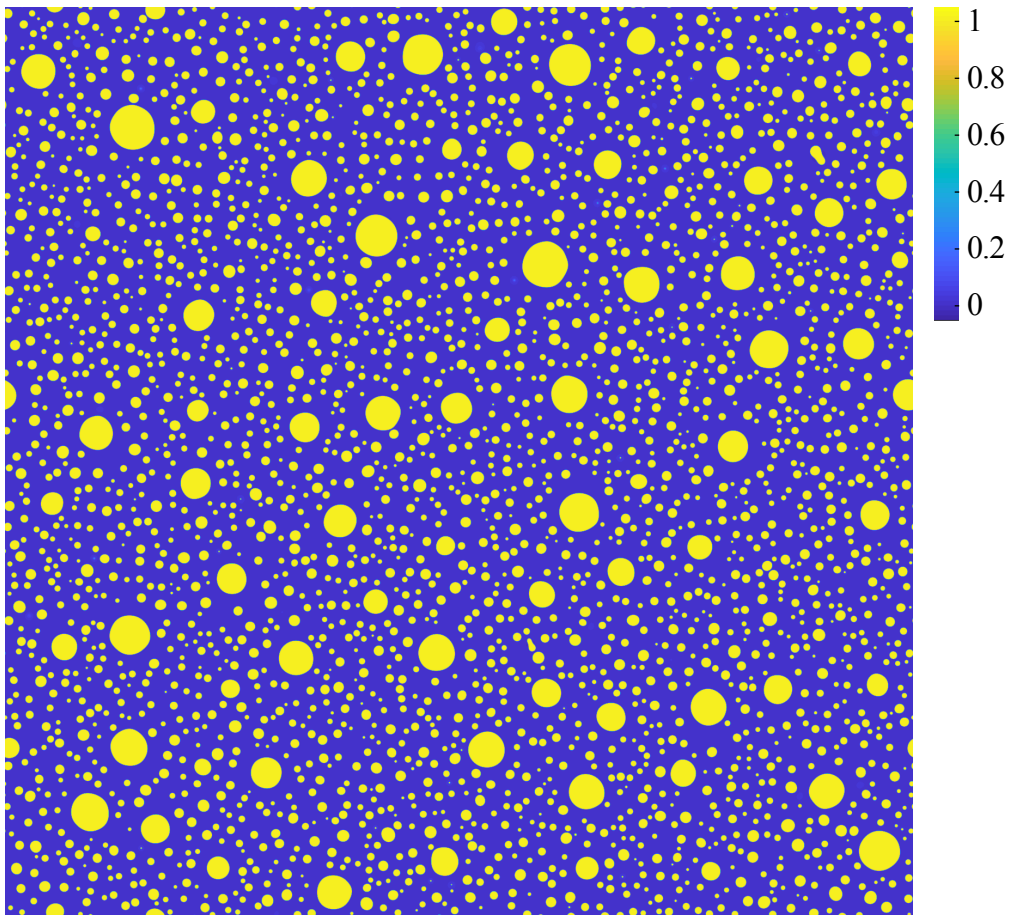

Figure 7.3: Order parameter at time $t = 3.7 \times 10^5$ during the simulation of coarsening with an initially bimodal particle size distribution.

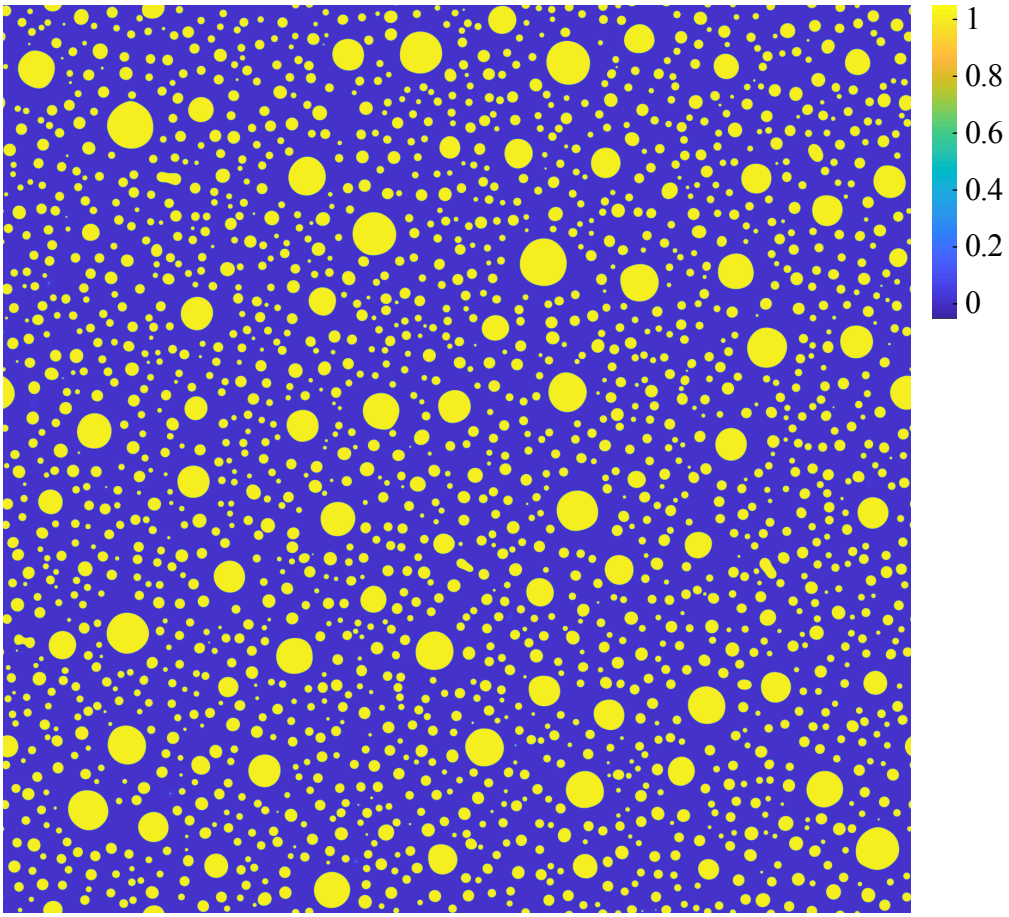

Figure 7.4: Order parameter at time $t = 7.2 \times 10^5$, the end of the simulation of coarsening with an initially bimodal particle size distribution.

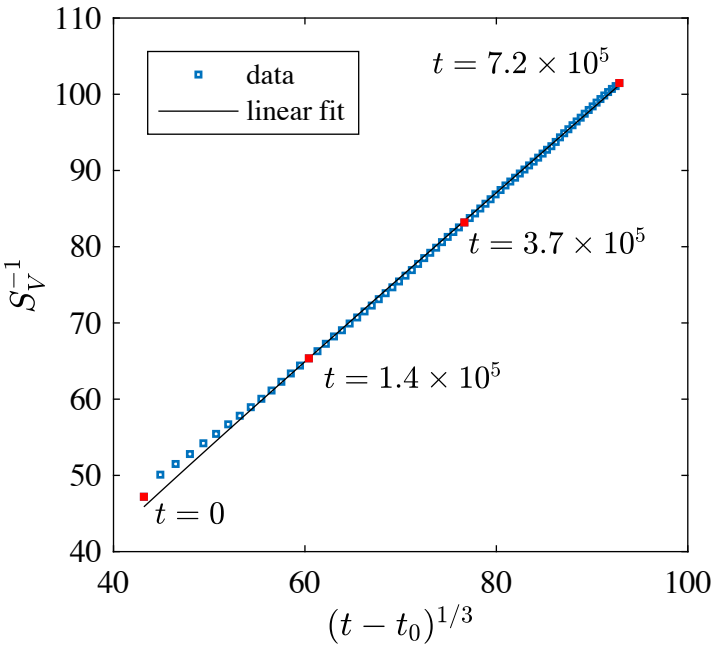

Figure 7.5: Characteristic length S_V^{-1} for the structure with an initially bimodal particle size distribution (blue squares) is plotted vs. time t alongside a fit to the expected coarsening power law (black line). The times depicted in Figs. 7.1-7.4 are indicated by red symbols.

These distributions would be equivalent to one-dimensional ISDs, except that they are functions of radius of curvature rather than curvature itself. For visualization, the distributions are plotted in semilog scale, where log is taken for the horizontal axis. These choices (independent variable, weighting, and axis scale) were made to clearly represent the two populations with highly disparate length scales.

Two peaks are present in Figs. 7.6 and 7.7, corresponding to large and small particles. In Fig. 7.6, the small-particle peak remains stationary about $R = 0.34\ S_V^{-1}$ over time, indicating that the small particles coarsen with the same rate as the overall structure. The height and area of the large-particle peak increase at the expense of the small-particle peak, which means that it contains a growing proportion of the total interfacial length in the system. In addition, the large-particle peak shifts leftward, indicating that the large particles are coarsening more slowly than the characteristic length scale of the system. These trends are confirmed when we examine the unscaled behavior, shown in Fig. 7.7: the location of the large-particle peak shifts from $R = 94$ to $R = 106$, or by 12%, over the course of the simulation, while the small-particle peak shifts from $R = 17$ to $R = 34$, or by

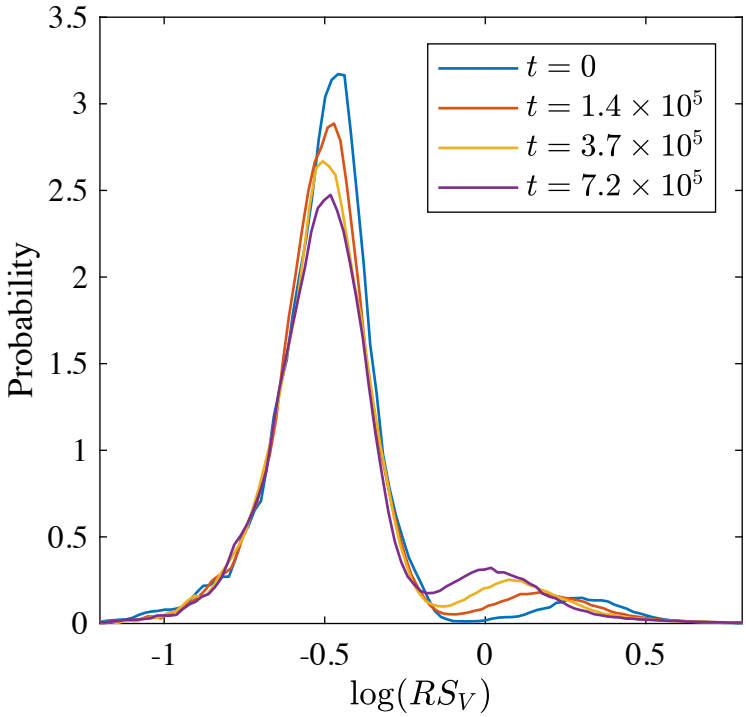

Figure 7.6: Distributions of scaled radius-of-curvature, $RS_V = S_V/\kappa$, for the structures shown in Figs. 7.1-7.4. Two peaks are present corresponding to the small and large particle distributions introduced in the initial condition, and the small-particle peak is stationary.

100%. Thus the change in the small-particle peak is much larger relative to its initial state, which explains why it dominates the evolution of the overall system. These simulation results support the hypothesis that there exists a critical length scale that separates populations of interfaces that evolve self-similarly from those that do not, even though the simulated microstructure is vastly different from its experimental counterpart. We also identify that the domination of the actively evolving population is responsible for the $t^{1/3}$ growth power law observed so universally.

7.3 Methods

Particle coarsening was simulated using the Cahn-Hilliard equation, Eq.3.4. The size of the simulation domain was $L_x = L_y = 6400$, and the model and discretization parameters are described in Section 3.3.

The structure used as an initial condition for the simulation was generated in stages. Starting

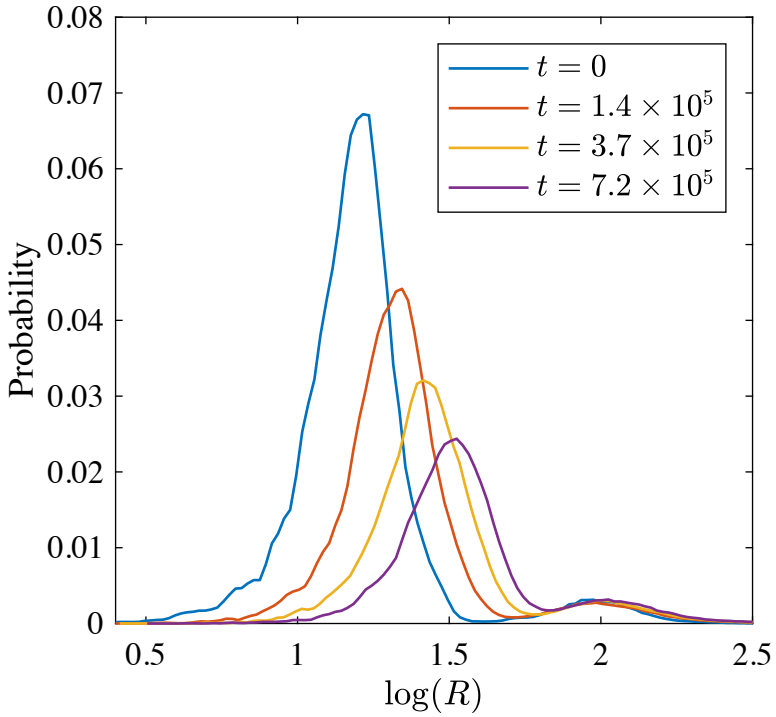

Figure 7.7: Distributions of unscaled radius-of-curvature, $R = 1/\kappa$, for the structures shown in Figs. 7.1-7.4. Two peaks are present corresponding to the small and large particle distributions introduced in the initial condition, and the large-particle peak is approximately stationary.

from a uniformly zero concentration field, large particles were generated sequentially until $\langle\phi\rangle = 0.051$. Then small particles were generated until $\langle\phi\rangle = 0.210$, and finally a uniform concentration field was added to approximate the mean field concentration during coarsening, resulting in $\langle\phi\rangle = 0.218$. Details of these stages are given below.

To generate a particle, three random floating-point numbers were sampled from a uniform distribution over $[0,1]$. The first two were multiplied by the domain length to set the coordinates of the particle center, x_0 and y_0. The remaining number was interpolated onto a discrete cumulative particle size distribution to determine particle radius R. To prevent the creation of overlapping particles, the trial is aborted if $\phi(x,y) > 0.5$ within a fixed radius of (x_0, y_0). This radius, r_{contact}, corresponds to the minimum allowed distance between the center of the new particle and the perimeter of any existing particles. For large particles, $r_{\text{contact}} = 384$ was used, and for small particles, $r_{\text{contact}} = 32$.

If this check was passed, then a new particle was added to the existing concentration field $\phi_0(x,y)$:

$$\phi(x,y) = \phi_0(x,y) + \frac{1}{2}\left(1 + \tanh\left\{\left[R - \sqrt{(x-x_0)^2 + (y-y_0)^2}\right]/2\right\}\right). \tag{7.1}$$

Since the hyperbolic tangent is zero in most of the domain, only a small part of the total domain, a square with side length $L_{sq} = 4R + 64$ centered at (x_0, y_0), was ever updated each time a particle was added. If this square was intersected by a domain boundary, then a translation of the particle would be added to the translation of the square to ensure periodicity. For example, if $x_0 + L_{sq} > L_x$, then a particle centered at $(x_0 - L_x, y_0)$ with the same radius as the original would be added to a square centered at $(x_0 - L_x, y_0)$.

To minimize morphological evolution within each mode, the particle size distributions (PSDs) used for sampling were based on the steady-state PSD for $\langle\phi\rangle \approx 0.22$. This PSD was obtained from a smaller 1600^2 phase field simulation with $\langle\phi\rangle = 0.221$ initialized with a single-modal PSD with average radius $\bar{R} = 8$. The PSD of the single-modal simulation appeared to converge after $t = 5 \times 10^4$, and so the steady state PSD was taken to be the time average over $6 \times 10^4 \leq t \leq 10^5$. The resulting PSDs are shown in Figure 7.8. They reflect input $\bar{R}$ values of 16 for small particles and 96 for large particles. Due to truncation of the steady state PSD at $R/\bar{R} = 2$ and $R/\bar{R} = 1.5$ for small and large particles, respectively, these result in actual average radii of 14.6 and 80.9.

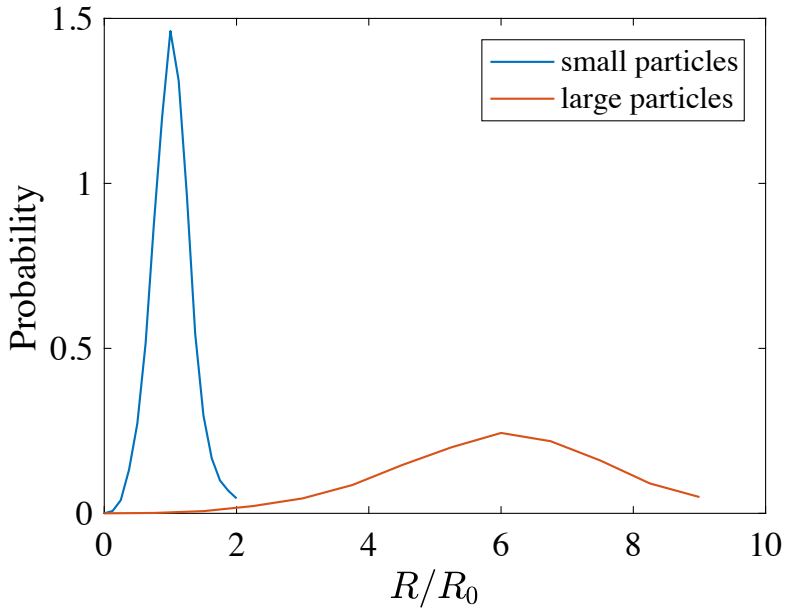

Figure 7.8: Particle size distributions sampled to generate the simulation initial condition. They are normalized independently, and so do not reflect probability in the final structure, where large particles would be much less frequent.

Chapter 8

Preliminary work

This chapter comprises two sections of preliminary work, essentially short chapters that have neither been published nor considered as comprehensively as Chapters 4-6. The first considers additional simulation results that support the relationship between kinetics and morphology derived in Chapter 4, and the second describes a model and results for kinetically inhibiting pinching-off of necks during coarsening.

8.1 Application of geometrically general theory

Here we consider additional systems in which the geometrically general theory for coarsening [52] was found to be applicable. The theory was introduced in Chapter 2, but we specifically examine Eq. 4.8, which was derived in Chapter 4 and applied to relate the coarsening kinetics and morphologies of 3-D systems with dissimilar mobilities. Eq. 4.8 expresses a linear relationship between dS_V^{-3}/dt, the instantaneous coarsening rate constant, and σ^2_{H/S_V}, the variance in scaled mean curvature. The principal assumption of this equation, noted in Chapters 2 and 4, is that H, the mean curvature of an interface, H_n, the mean curvature of its connected neighbor interface, and λ, the distance over which they interact, are all uncorrelated. This assumption seemed to be valid for the bicontinuous structures examined in Chapter 4, and here we test it for structures at non-50/50 volume fractions, 36/64, 34/66, and 32/68. We also examine the effect of differences in morphology other than volume fraction by simulating coarsening in a structure at 50/50 that was phase separated with non-conserved (Allen-Cahn [179]) dynamics.

8.1.1 Kinetics and morphology at non-$50/50$ volume fractions

We consider structures with $\langle\phi\rangle = 0.32$, $\langle\phi\rangle = 0.34$, $\langle\phi\rangle = 0.36$, and $\langle\phi\rangle = 0.50$, all initialized by random noise and simulated with the Cahn-Hilliard equation, Eq. 3.4, with constant mobility. These structures correspond to nominal volume fractions of $32/68$, $34/66$, $36/64$, and $50/50$, respectively. The $\langle\phi\rangle = 0.50$ structure has been previously discussed in Chapters 4 and 5, and the $\langle\phi\rangle = 0.32$ and $\langle\phi\rangle = 0.36$ structures were compared to surface-diffusion structures in Chapter 5. The remaining structure, $\langle\phi\rangle = 0.34$, had a larger domain size, $L_x = L_y = L_z = 1280$, than the others, but other parameters were the same.

Coarsening kinetics of the structures are compared in Fig. 8.1 up to $t = 8 \times 10^5$. Consistent with the results of a previous study [55], we find that coarsening rate constant increases with decreasing volume fraction of $\phi = 1$ phase (i.e., greater asymmetry between the volume fractions). The instantaneous coarsening rate constant dS_V^{-3}/dt was calculated by taking centered differences between the points in Fig. 8.1. The variance of mean curvature σ^2_{H/S_V} was calculated using methods described in previous Chapters, and the relationship between dS_V^{-3}/dt and σ^2_{H/S_V} is plotted in Fig. 8.2.

In Fig. 8.1, the $\langle\phi\rangle = 0.34$, $\langle\phi\rangle = 0.36$, and $\langle\phi\rangle = 0.50$ structures appeared to follow the same linear trend. They were fitted together to Eq. 4.8, resulting in $\hat{\lambda} = 0.44$, the same value obtained for $\langle\phi\rangle = 0.50$ by itself in Chapter 4. However, the $\langle\phi\rangle = 0.34$ and $\langle\phi\rangle = 0.36$ structures undergo more evolution; σ^2_{H/S_V} decreases substantially in both cases, resulting in a corresponding decrease in dS_V^{-3}/dt. The $\langle\phi\rangle = 0.32$ structure is slightly offset from the fitted line, and a fit to it alone results in $\hat{\lambda} = 0.48$. Its variance of mean curvature and coarsening rate increase initially then decrease to near their original values. The different behavior of the $\langle\phi\rangle = 0.32$ case is likely due to its proximity to the limiting volume fraction for bicontinuity discussed in Section 5.4.

In summary, the relationship between kinetics and morphology given by Eq. 4.8 appears to generalize well to lower volume fractions of $\phi = 1$ phase. For non-$50/50$ mixtures that are still

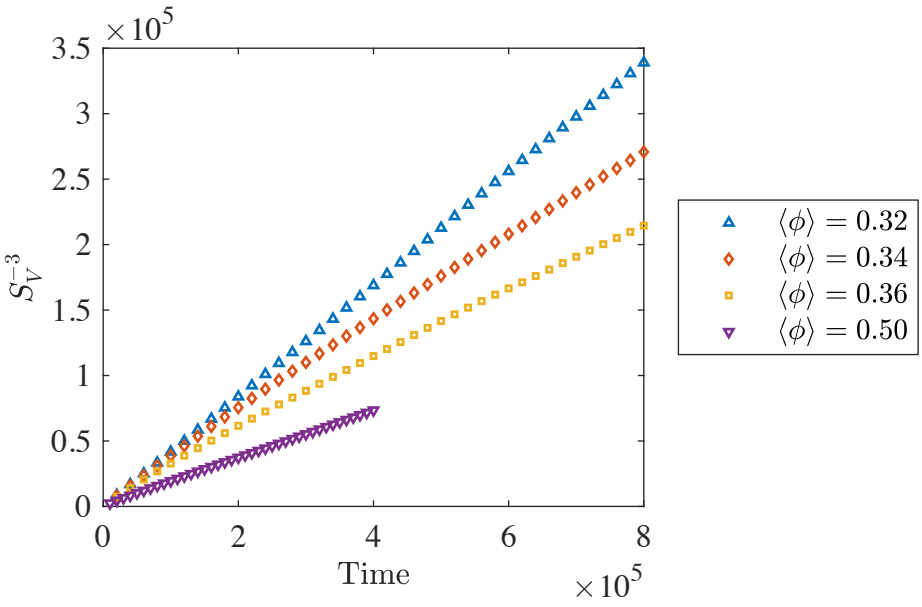

Figure 8.1: Kinetics of coarsening via bulk diffusion for systems with different average compositions. S_V^{-3} is plotted vs. time for $\langle\phi\rangle = 0.32$ (blue upward triangles), $\langle\phi\rangle = 0.34$ (red diamonds), $\langle\phi\rangle = 0.36$ (yellow squares), and $\langle\phi\rangle = 0.50$ (purple downward triangles).

bicontinuous, Eq. 4.8 can be re-expressed to separately account for the fluxes through each phase,

$$\frac{dS_V^{-3}}{dt} = 6K_D\frac{\sigma^2_{H/S_V}}{\hat{\lambda}^+} + 6K_D\frac{\sigma^2_{H/S_V}}{\hat{\lambda}^-}, \tag{8.1}$$

where $\hat{\lambda}^+$ and $\hat{\lambda}^-$ are the interaction distances of the phases. For these systems, $\hat{\lambda}$ in Eq. 4.8 is therefore the harmonic mean of the interaction distances for each phase,

$$\frac{2}{\hat{\lambda}} = \frac{1}{\hat{\lambda}^+} + \frac{1}{\hat{\lambda}^-}. \tag{8.2}$$

The difference between $\hat{\lambda}^+$ and $\hat{\lambda}^-$, if one exists, cannot be calculated from the current simulations, but might be obtainable by simulations with dissimilar mobilities at lower volume fractions.

8.1.2 Kinetics and morphology with different initial conditions

Here, we compare evolution at $\langle\phi\rangle = 0.50$ with constant mobility, but different initial morphologies. The $\langle\phi\rangle = 0.50$ simulation considered elsewhere in this dissertation was initialized with ran-

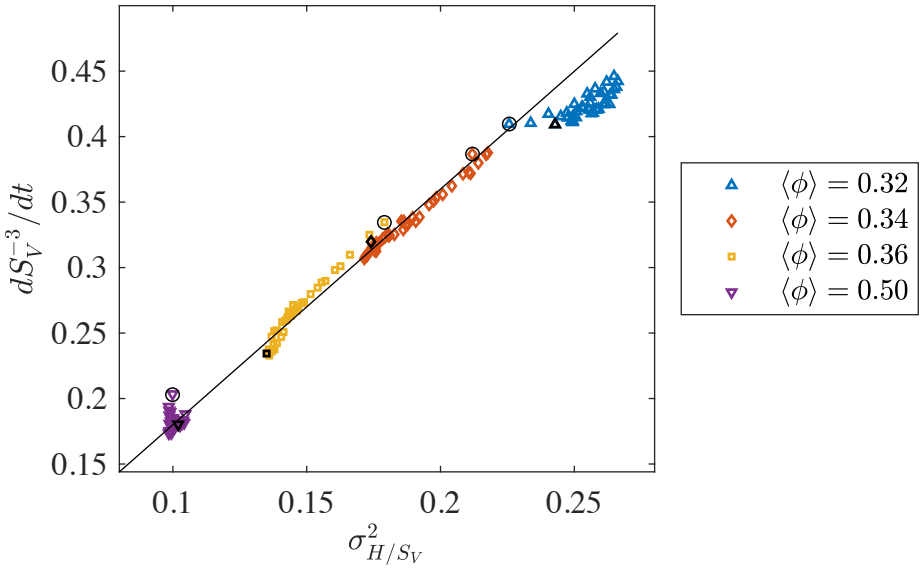

Figure 8.2: Plot of dS_V^{-3}/dt, the instantaneous coarsening rate, vs. the variance of scaled mean curvature, σ^2_{H/S_V}, for systems with different average compositions: $\langle\phi\rangle = 0.32$ (blue upward triangles), $\langle\phi\rangle = 0.34$ (red diamonds), $\langle\phi\rangle = 0.36$ (yellow squares), and $\langle\phi\rangle = 0.50$ (purple downward triangles). A fit of Eq. 4.8 to the $\langle\phi\rangle = 0.34$, $\langle\phi\rangle = 0.36$, and $\langle\phi\rangle = 0.50$ data sets is indicated by a solid black line with slope 1.80. The earliest data points are circled, and the final data points are noted by black symbols.

dom noise and evolved with the Cahn-Hilliard equation, Eq. 3.4. In this sub-section, it is referred to as the RN IC structure, for random noise initial condition. The other simulation considered in this section was phase separated with the Allen-Cahn equation [179],

$$\frac{\partial\phi}{\partial t} = -\left[f'(\phi) - \varepsilon^2\nabla^2\phi\right], \tag{8.3}$$

and is referred to as the AC IC structure, for Allen-Cahn initial condition. It was parametrized with the same $f(\phi)$ and ε^2 as the Cahn-Hilliard model, and the same finite difference approximations were used, with $\Delta t = 0.5$ and $\Delta x = 1$. The order parameter ϕ was initialized with random noise in a domain of size $L_x = L_y = L_z = 800$. It was evolved with Eq. 8.3 until $t = 120$, which resulted in a bicontinuous structure with $S_V^{-1} \approx 13$. Re-setting the simulation time to $t = 0$, the AC IC simulation was then evolved with the Cahn-Hilliard equation, Eq. 3.4, until $t = 1.6 \times 10^5$.

The initial and final ISDs for the AC IC structure are shown in Fig. 8.3, and they differ substantially from those of the RN IC structure (shown in Figs. 4.8 and 5.7). The initial ISD (Fig. 8.3a) is

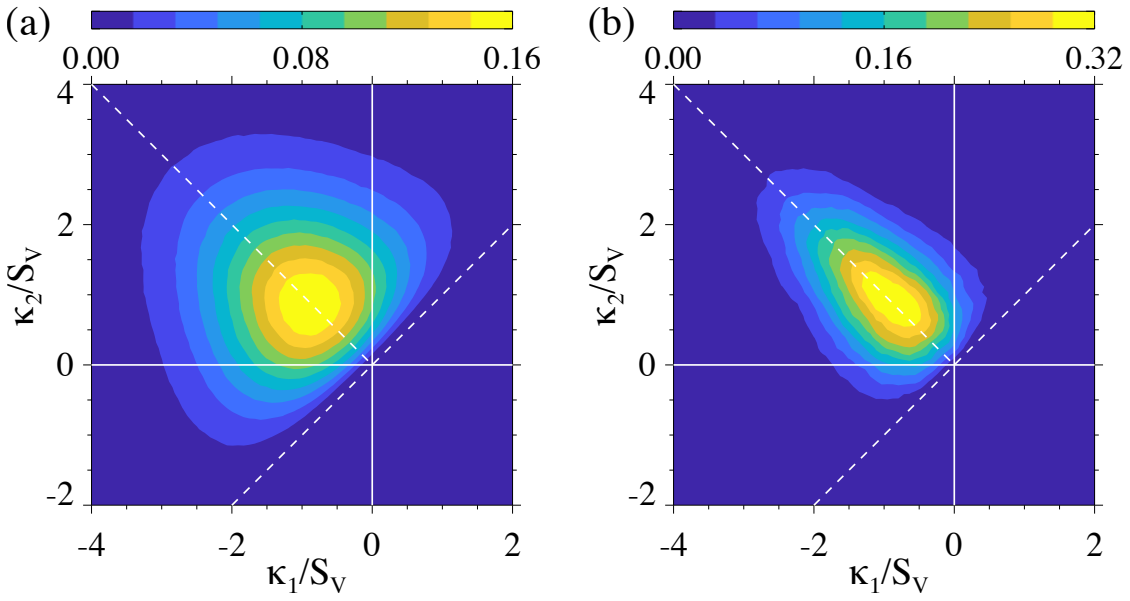

Figure 8.3: (a) Initial and (b) final ISDs for the AC IC structure ($\langle\phi\rangle = 0.50$, coarsened via bulk diffusion).

very broad, but by $t = 1.6 \times 10^5$ (Fig. 8.3b) it becomes more concentrated around the line $H = 0$, like the RN IC structure. The coarsening kinetics of these structures are shown in Fig. 8.4. The AC IC structure coarsens much more quickly than the RN IC structure, reaching a similar final characteristic length ($S_V^{-1} \approx 40$, ten times the interfacial thickness) in less than half of the time.

The relationship between instantaneous coarsening rate constant, dS_V^{-3}/dt, and variance of scaled mean curvature, σ^2_{H/S_V}, is plotted in Fig. 8.5 for the RN IC and AC IC structures. A fit of Eq. 4.8 to both data sets is indicated by the solid black line in Fig. 8.5, and it resulted in $\hat{\lambda} = 0.44$. The faster coarsening rate constant of the AC IC structure is therefore fully explained by the change in morphology. This example provides a well-controlled validation of Eq. 4.8, as it lacks any of the possible confounding variables in the previous examples (the difference in kinetics between constant- and dissimilar mobility structures in Chapter 4 and the differences in $\langle\phi\rangle$ in the previous subsection). Now that we have independently confirmed $\hat{\lambda} \approx 0.44$ as the scaled diffusional interaction distance for $\langle\phi\rangle = 0.50$, the agreement in $\hat{\lambda}$ between different volume fractions becomes more compelling. This value, $\hat{\lambda} \approx 0.44$, may a universal constant for coarsening of bicontinuous structures via bulk diffusion with a constant mobility.

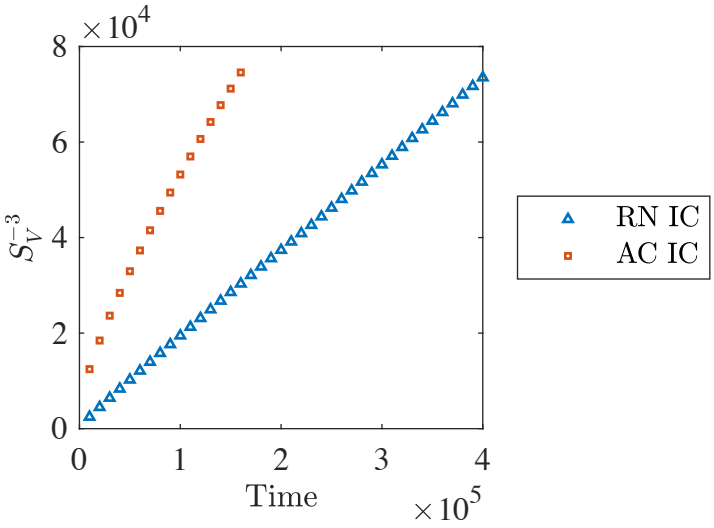

Figure 8.4: Plot of S_V^{-3} vs. time for coarsening of the RN IC (blue triangles) and AC IC (red squares) structures via bulk diffusion.

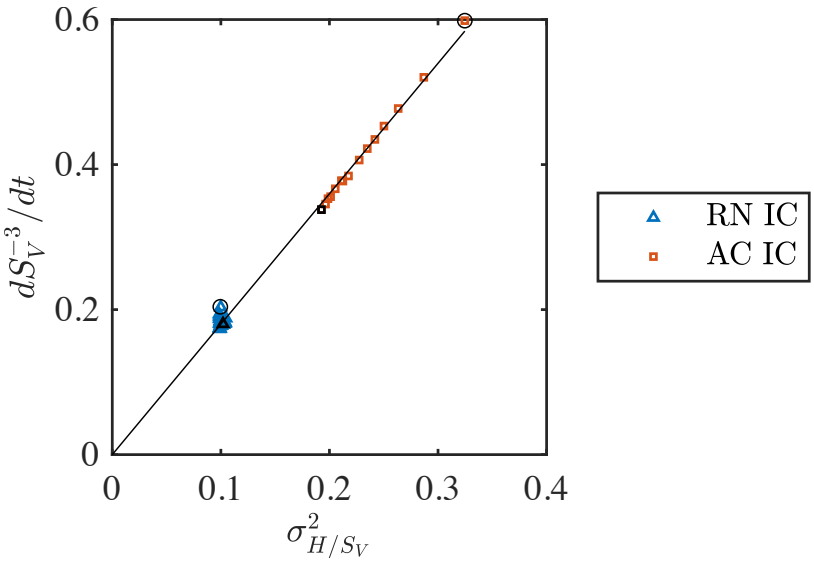

Figure 8.5: Plot of dS_V^{-3}/dt, the instantaneous coarsening rate, vs. the variance of scaled mean curvature, σ^2_{H/S_V}, for the RN IC (blue triangles) and AC IC (red squares) structures. A fit of Eq. 4.8 to both data sets is indicated by a solid black line with slope 1.80. The earliest data points are circled, and the final data points are noted by black symbols.

8.2 Inhibiting topological singularities

This section describes an effort to inhibit topological singularities in the coarsening of complex microstructures, with the goal of understanding the role those events play in the coarsening process. Topological singularities occur in particulate systems when a particle disappears; the particle's radius decreases below a critical value, and it dissolves into the matrix phase. In bicontinuous systems, which have high genus and no independent particles, a topological singularity occurs when a neck connecting regions of the same phase pinches off, reducing the genus of the structure by one and leaving behind two 'caps' [120, 121]. In both particulate and bicontinuous structures, topological singularities involve features with high curvature relative to the rest of the structure, and therefore we expect that inhibiting topological singularities will reduce coarsening rate. The role of topological singularities in bicontinuous structures is complicated by the fact that the interface is completely connected, which may cause an interdependence between singularities. If there is some necessary ordering for the pinching-off events, for example, then halting the pinching-off events would allow us to stop the coarsening process.

Therefore, we examined how to inhibit the pinching-off of necks in bicontinuous structures. Two possible approaches were considered: imposing a thermodynamic constraint (i.e., a Lagrange multiplier) and freezing the kinetics. The thermodynamic approach has been considered previously for vesicle dynamics (Willmore flow) [180, 181], but adaptation of the technique for coarsening represents a significant mathematical and numerical challenge. We therefore took the kinetic approach, and found a simple method that was highly effective at inhibiting topological singularities. A phase field model was formulated with a mobility that varied continuously in space and discontinuously in time. Our code swept through the simulation domain and used criteria based on the order parameter and its gradient to identify points at the center of necks that were about to pinch off. The code would then decrease ('freeze') mobility in a spherical region around the point, preventing transport of material from the neck and inhibiting it from pinching off. With appropriate pinching criteria and freezing parameters, this method was able to successfully prevent most

topological singularities during coarsening simulations.

8.2.1 Methods

This technique employs the Cahn-Hilliard model, Eq. 3.4, with a spatially and temporally dependent mobility $M(\vec{x},t)$. Periodic boundary conditions were employed, and the model parameters are as described in Chapter 3. Simulations were initialized with random noise at $\langle\phi\rangle = 0.50$ and coarsened with constant mobility until a set time, at which the inhibited-pinching model was activated.

Pinching locations were identified by taking advantage of the symmetry at the necking point. The ranges of values of ϕ in the bulk and $|\nabla\phi|$ in the interface are known. Due to the cylindrical symmetry of the interfaces about the necking point, we expect $|\nabla\phi|$ to be small even as ϕ takes a non-bulk value. In the bulk, ϕ must satisfy $f''(\phi) > 0$ to be thermodynamically stable or metastable, which for our choice of $f(\phi)$ equates to a requirement that $\phi > 0.789$ or $\phi < 0.211$. For a planar interface, $|\nabla\phi|$ is equal to $\frac{1}{\varepsilon}\sqrt{2f(\phi)}$, which results in $|\nabla\phi| = 0.16$ at $\phi = 0.8$, for example. The specific criteria used for simulations were fine-tuned by trial and error.

Once a point $\vec{x}_0$ was identified, mobility was reduced around it by multiplying the mobility field $M(\vec{x},t)$ by a hyperbolic tangent function that is very small near $\vec{x}_0$ and equal to one far from $\vec{x}_0$,

$$M(\vec{x},t_n) = M(\vec{x},t_{n-1})\frac{1}{2}\left(1+\tanh\left[\frac{1}{2}\left(|\vec{x}-\vec{x}_0|-R\right)\right]\right), \tag{8.4}$$

where R is the radius of the diffuse sphere in which mobility is reduced. To prevent multiple mobility reduction events in the same location, an additional criterion $M(\vec{x},t) > M_c$ was used. The mobility criterion M_c and pinching radius R could be changed to inhibit topological singularities in different ways.

8.2.2 Results

The first setup that was implemented employed a small pinching radius, $R = 6$, and a low mobility cutoff, $M_c = 10^{-4}$, and criteria $|\nabla\phi| < 0.08$ and $0.3 < \phi < 0.7$ for detecting pinching events. The

low mobility cutoff allowed multiple freezing events in close proximity, but the small size of the radius meant that all of the freezing was highly localized around the neck. Figure 8.6 illustrates a typical example of this setup, with (a) showing the initial structure, a Cahn-Hilliard simulation at $t = 5 \times 10^4$, (b) shows the continuation of that simulation to $t = 8 \times 10^4$ as a baseline, and (c) shows the inhibited-pinching structure at $t = 8 \times 10^4$. The entire domain size, $L_x = L_y = L_z = 128$, is shown. Nine pinching-off events occurred in the baseline case ($g = 19$ from $g = 28$ in the initial structure), while none occurred in the inhibited-pinching case. In the inhibited-pinching case, Fig. 8.6c, topological singularities were successfully inhibited by the formation of long, kinetically frozen necks, one of which is circled. However, this set of parameters does not seem to substantially affect evolution; the interfaces around the neck seem to evolve as if it had in fact pinched off.

Therefore, a second setup was explored, in which a much larger region around the neck was frozen. In this setup, the radius of freezing was set approximately equal to the characteristic length, and a higher mobility cutoff, $M_c = 0.5$, was used, which allowed only one freezing event per detected pinching event. The detection criteria for this setup were $0.25 < \phi < 0.75$ and $|\nabla\phi| < 0.085$. A small-scale ($L_x = L_y = L_z = 128$) simulation with these parameters is shown in Fig. 8.7. The inhibited-pinching model was activated after $t = 5 \times 10^4$, the condition shown in Fig. 8.7a, and the freezing radius was $R = S_V^{-1} = 22$. In Fig. 8.7b, the structure is shown at $t = 10^5$, after some coarsening with the inhibited-pinching model. There are none of the elongated necks observed in the previous setup (Fig. 8.6c), but there are several narrow necks that appear to blend in with the structure. These are more apparent at $t = 4 \times 10^5$ (Fig. 8.7c), when the interface has begun to change shape around the frozen zone. As in the previous setup, the genus remained constant at $g = 28$, indicating that topological singularities were inhibited.

To assess how inhibiting topological singularities quantitatively affect evolution, larger simulations ($L_x = L_y = L_z = 512$) were conducted using the second setup. Starting from the same constant-mobility simulation, two inhibited-pinching simulations were conducted, one starting at $t = 5 \times 10^4$ with $R = S_V^{-1} = 22$ and the other starting at $t = 10^5$ with $R = S_V^{-1} = 27$. The constant-

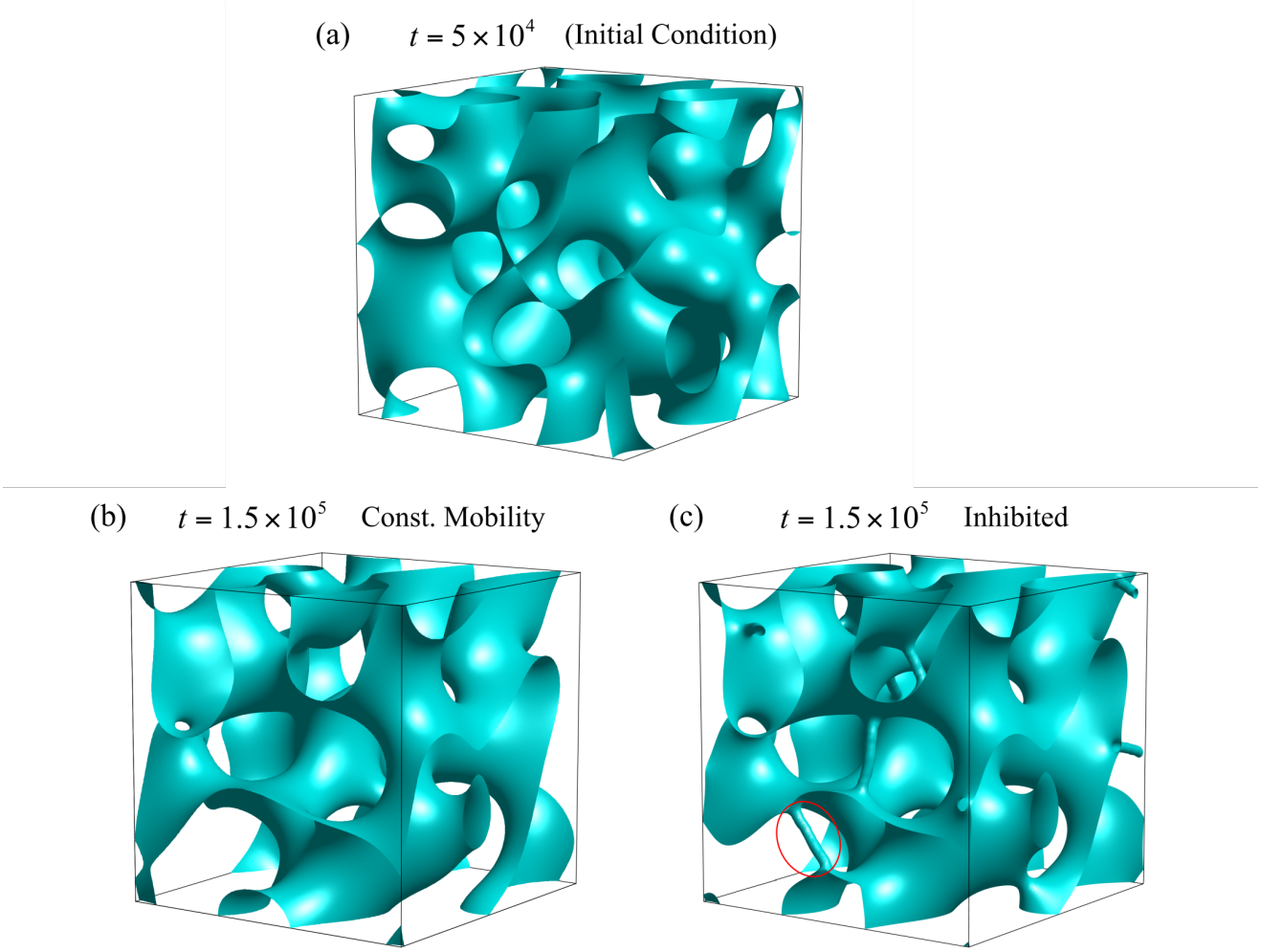

Figure 8.6: Small-scale ($L_x = L_y = L_z = 128$) inhibited-pinching simulation with a small freezing radius, $R = 6$. The structures shown are (a) the initial Cahn-Hilliard structure ($t = 5 \times 10^4$, $g = 28$), (b) the Cahn-Hilliard structure at later time ($t = 8 \times 10^4$, $g = 19$), and (c) the inhibited-pinching structure at a later time ($t = 8 \times 10^4$, $g = 28$). Topological singularities have been prevented in (c) by the kinetic freezing of the necks, one of which is circled in red.

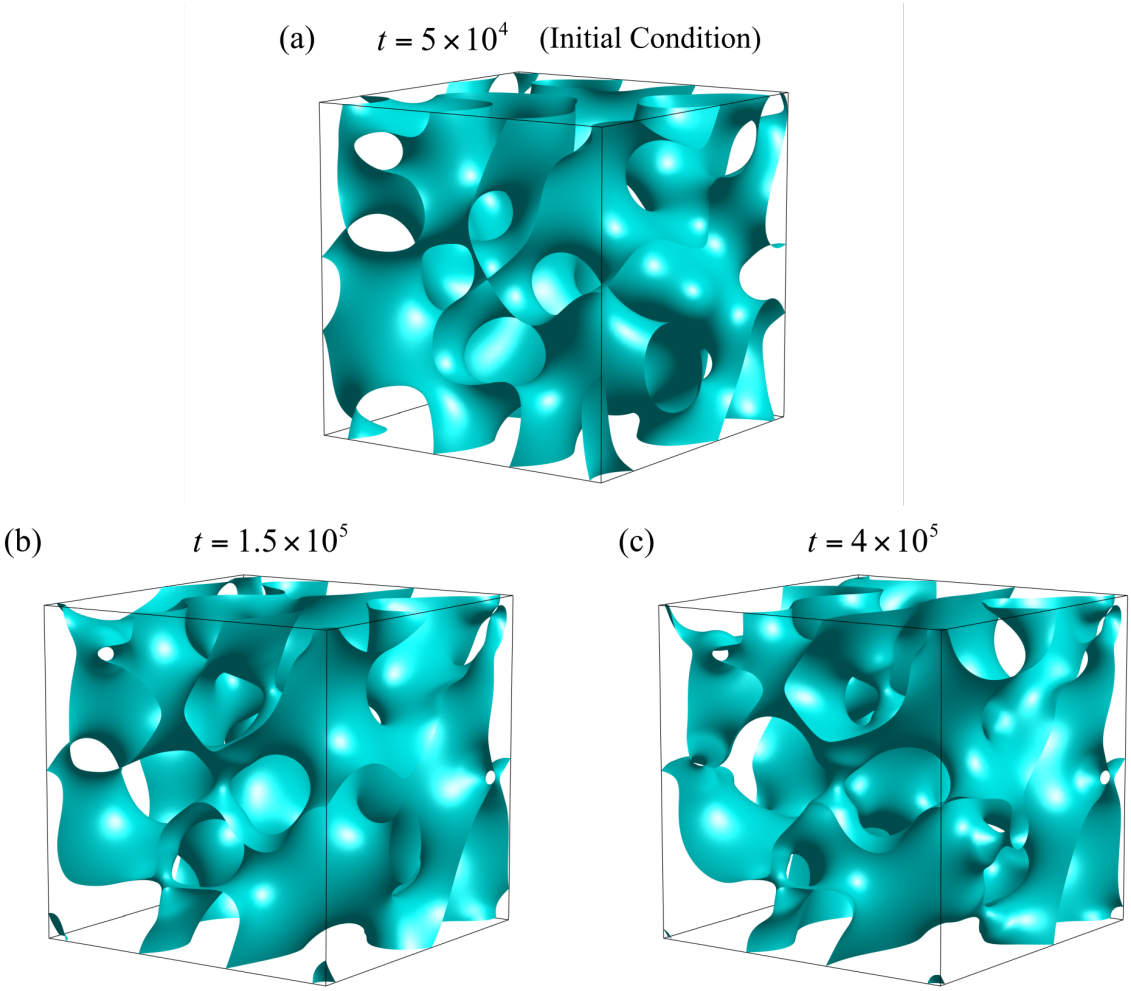

Figure 8.7: Small-scale ($L_x = L_y = L_z = 128$) inhibited-pinching simulation with a large freezing radius, $R = 22$. The structures shown are (a) the initial Cahn-Hilliard structure ($t = 5 \times 10^4$), (b) the inhibited-pinching structure after some initial evolution ($t = 10^5$), and (c) the inhibited-pinching structure at a much later time ($t = 4 \times 10^5$). In (c) the locations of the frozen necks are apparent from the motion of the interface around the frozen zone.

mobility simulation and inhibited-pinching simulations were continued until $t = 4 \times 10^5$. The coarsening kinetics (i.e., S_V^{-3} vs. time), evolution of genus g, and evolution of volume-averaged mobility $\langle M(x) \rangle$ of these simulations are shown in Fig. 8.8. Inhibiting pinching reduces the rate of coarsening apparent in Fig. 8.8a, although not to zero. In Fig. 8.8b, the difference in genus between the control and the inhibited-pinching simulations $R = 22$ and $R = 27$ indicates that most topological singularities are being inhibited. Average mobility (Fig. 8.8c) decreases rapidly at early times, but continues to decrease over the course of the simulations, indicating that freezing events are still occurring (i.e., pinching-off sites are still being detected).

The change in coarsening rate with inhibited pinching highlights the importance of topological singularities to the coarsening process. This is not surprising as, based on results in Chapters 4 and 5, we know that necks are some of the highest-curvature features in bicontinuous structures. The fact that coarsening continues and pinching-off sites continue to be detected suggests that topological singularities are not strongly dependent upon each other. The exact correlation or lack of correlation between topological singularities could be determined by a more extensive investigation of their role in non-inhibited simulations. This provides an interesting topic for future work. LSW theory achieves part of its simplicity by neglecting correlations between topological features (i.e., particles). If evolving necks are uncorrelated from each other in bicontinuous structures, then perhaps an LSW-like theory can be developed to describe their evolution.

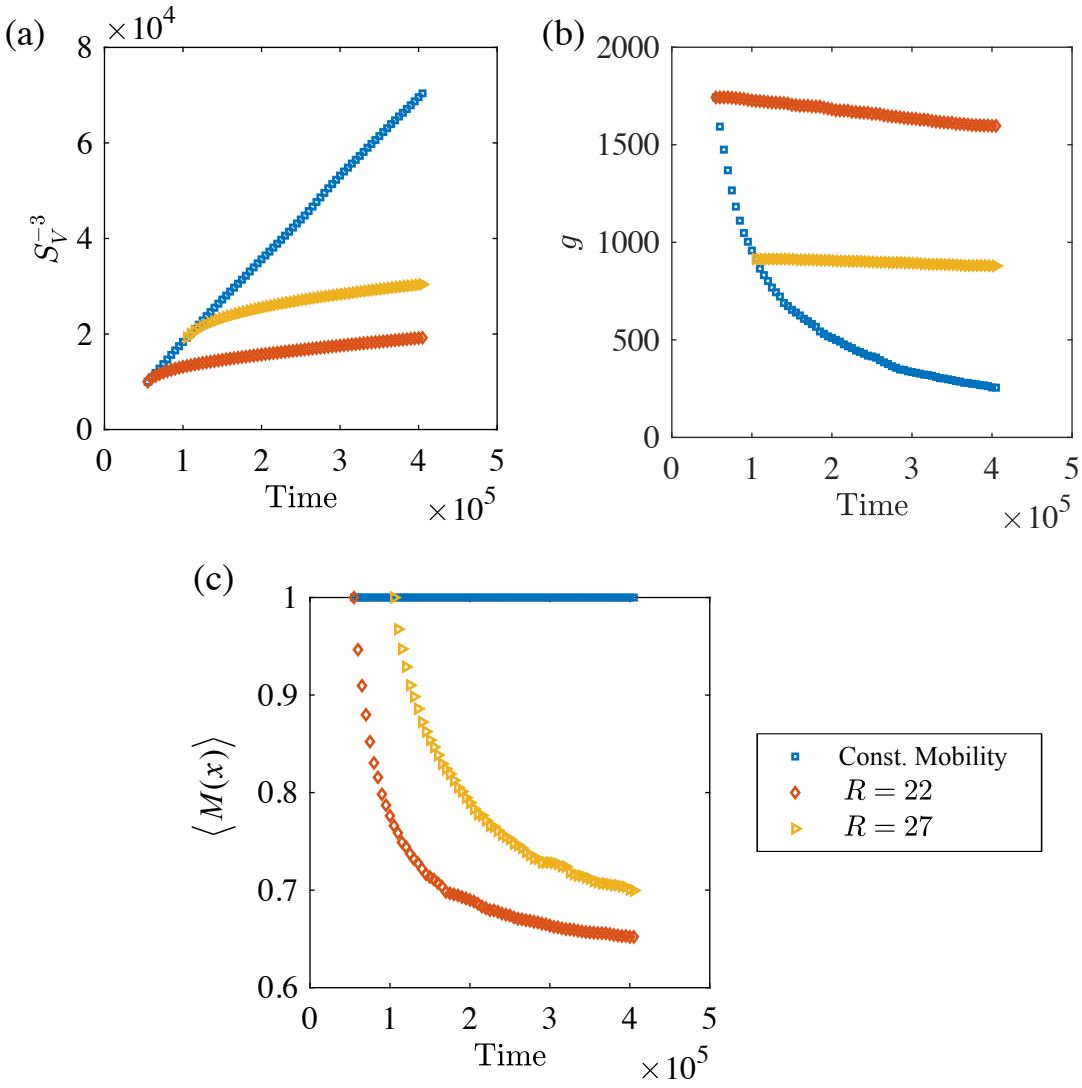

Figure 8.8: Evolution of the constant-mobility structure (blue squares), freezing radius $R = 22$ inhibited-structure (red diamonds), and freezing radius $R = 27$ inhibited-pinching structure (yellow triangles). (a) depicts coarsening kinetics, S_V^{-3} vs. time, (b) shows the time evolution of genus g, and (c) shows the time evolution of the volume average of the mobility, $\langle M(x) \rangle$.

Chapter 9

Summary, applications, and future work

9.1 Summary

The overall objective of this dissertation was to build a foundation for a theory of coarsening of complex microstructures. To make progress toward this objective, simulation studies were conducted under idealized conditions using the phase field method. These studies build upon previous work (Refs. [51, 53, 54, 55]) by examining conditions that are commonly found in experimental systems, such as coarsening of phases having dissimilar bulk mobilities and coarsening via surface diffusion. The differences and similarities between conditions will help future authors develop and test hypotheses about the dynamics of coarsening in complex microstructures, leading eventually to a comprehensive theory. Already, this dissertation has presented evidence for the validity of two hypotheses that have immediate practical relevance. We have found a relationship between coarsening kinetics and global morphology predicted by DeHoff's geometrically general theory of coarsening, and we demonstrated how inactive length scales can cause coarsening kinetics to follow the $t^{1/3}$ power law even in the absence of self-similarity. In this section, we summarize our findings, and in the following sections, we discuss applications and future work.

In Chapter 4, coarsening of a two-phase system in which the phases had dissimilar mobilities was studied at $50/50$ (50%) volume fraction. A morphological transition during coarsening was identified in two dimensions when the mobility was dissimilar, which was not observed when the mobility was constant. This morphological transition in the dissimilar-mobility structure resulted

in a decrease of its coarsening rate constant over time, while the kinetics of the constant-mobility case agreed with the $t^{1/3}$ power law after an initial transient stage. The 3-D simulations with dissimilar mobilities resulted in bicontinuous morphologies that evolved self-similarly. The self-similar morphology for the dissimilar-mobility cases has greater variance in scaled mean curvature than the constant-mobility morphology, as well as a slight asymmetry between areas corresponding to high- and low-mobility necks. The coarsening kinetics of the 3-D cases agreed well with the theoretical $t^{1/3}$ power law after initial transient stages. The transient kinetics of the 3-D cases were observed to follow the theoretical relationship between variance in scaled mean curvature, σ^2_{H/S_V}, and instantaneous coarsening rate constant, $k = dS_V^{-3}/dt$. Based on theory and simulations, the primary difference in the kinetics of coarsening between the dissimilar-mobility and constant mobility systems were determined to be a factor of two smaller kinetic coefficient in the dissimilar-mobility case due to the lack of diffusion in one of the phases.

In Chapter 5, 3-D simulations of coarsening via surface diffusion were performed using the model proposed by Rätz et al. [136]. At nominal volume fractions of $36/74$ (i.e., 36%) and 50%, the resulting structures were bicontinuous, and self-similar coarsening via surface diffusion was observed. Self-similarity of the structures was evident from scaling of the morphology and topology. Furthermore, coarsening kinetics followed the predicted $t^{1/4}$ power law. Differences in morphology and topology between structures coarsened with bulk and surface diffusion were quantified, and the structures were found to be very similar at 50% volume fraction. Coarsening at 32% volume fraction via both mechanisms resulted in structures that contained both a single well-connected domain (typical of bicontinuous structures) and a number of independent particles. Substantial transient evolution of the scaled morphology and topology was observed in both structures; self-similarity was not observed in the surface diffusion case and could not be verified conclusively in the bulk diffusion case. In the surface diffusion structure, the number of particles increased over time, since particles were unable to interact with the rest of the structure after breaking away. The sensitivity of the structures to volume fraction was confirmed by examining coarsening via bulk diffusion at 30%, in which the initial structure was observed to break up

rapidly into particles. Finally, coarsening was examined via alternative model, which employed the concentration-dependent mobility of the surface-diffusion model but retained the thermodynamics of the bulk-diffusion model, permitting solubility in the bulk. While this solubility-permitting model was shown to have similar coarsening kinetics to the surface diffusion model, the morphologies observed indicated that it does not effectively simulate surface diffusion.

Chapter 6 examined a phase field method for evolution via bulk diffusion when strong anisotropy is present. The model included an energy term proportional to the square of the Laplacian of the order parameter to regularize the strong anisotropy, and we studied the effect of this regularization term on dynamics. A planar interface at equilibrium was examined initially; the interfacial energy was found to be affected by the regularization, and a Cahn-Hoffman ξ-vector was derived for the modified interfacial energy. Then, the phase field model was related to sharp interface dynamics by an asymptotic analysis. The correct Gibbs-Thomson condition was obtained for the modified ξ-vector, and it was determined that the regularization had no effects on dynamics (other than the modification to the interfacial energy) up to second order in the interfacial width. Equilibrium shapes simulated with the phase field model were compared to predictions for the modified ξ-vector, and excellent agreement was obtained away from the regularized corner. The corner shape itself was found to agree with predictions for the curvature-squared regularization. The analysis in Chapter 7 will enable future simulations of coarsening that employ the strongly anisotropic Cahn-Hilliard equation with the Laplacian-squared regularization.

In Chapter 7, the concept of a self-similar length scale was explored. A 2-D simulation was initialized with populations of large and small particles. Coarsening in this system followed the $t^{1/3}$ power law for self-similar coarsening, despite the lack of self-similarity of the overall structure. We found, however, that the small particles coarsen self-similarly, and they controlled the kinetic behavior because they underwent more evolution than the large particles. The large particles were larger than the self-similar length scale of the small particle distribution, causing them to be less active relative to the overall structure.

Chapter 8 contained additional testing of the relationship between variance of scaled mean

curvature and coarsening rate first applied in Chapter 4 and a study of the role of topological singularities in the evolution of bicontinuous structures. The relationship between variance of scaled mean curvature and coarsening rate constant was found to hold in constant-mobility simulations at average volume fractions of 34%, 36%, and 50%. Dynamics at 32% deviated slightly from the trend at higher volume fractions. Constant-mobility simulations at 50% with different initial morphologies were also tested, and again the relationship was found to hold. Across all bicontinuous cases (i.e., excluding 32%), the scaled diffusional interaction distances were the same, $\hat{\lambda} = 0.44$. To examine the role of topological singularities in the evolution of bicontinuous structures, an algorithm was developed to detect the locations of necks that were in the process of pinching-off. By freezing the necks (i.e., setting mobility to near zero), it was possible to prevent most topological singularities from occurring. The resulting evolution was slower, highlighting the importance of topological singularities to coarsening kinetics. However, further investigation is required to fully understand their role in the coarsening process.

9.2 Applications

As noted in the Introduction, there are two types of applications of the results in this dissertation, direct comparison to experiments and testing hypotheses about the dynamics of coarsening in complex microstructures. Comparison to experiments is already ongoing for the surface-diffusion results. Collaborators [20, 128] have provided nanoporous gold structural data near 32% volume fraction. The corresponding surface diffusion structure (introduced in Section 5.4) had increasing scaled particle density over time. In the simulations, particles detach due to the pinching-off of the necks of material that connect them to the main structure. The particles can only move or evolve via surface diffusion, so they remain in place until the main structure comes into contact with them again. In the experimental system, a particle that breaks away from the structure cannot remain independent; it will immediately fall under its own weight, and may re-attach itself to the structure where it lands. It is not yet clear what effect this difference in particle behavior will have on the

comparison. If a successful comparison is made, or if in the disagreement some new phenomena is elucidated, this work would contribute substantially to the rapidly emerging research area of nanoporous materials

We have also applied our simulation results to test hypotheses about coarsening dynamics. We were able to demonstrate how features larger than a self-similar length scale can be kinetically inactive, leading to $t^{1/3}$ evolution without self-similarity. We were also able to demonstrate the relationship between variance of scaled mean curvature and instantaneous coarsening rate in several bicontinuous structures. This amounts to a validation of the assumption of DeHoff [52] that the mean curvature at a point, the mean curvature of its connected neighbor point, and the diffusional interaction distance between the two are all uncorrelated. Other relationships may follow from this assumption. For example, DeHoff also provides an equation for evolution of average mean curvature, which was not tested here. However, it remains to be seen whether the relationship between variance of scaled mean curvature and instantaneous coarsening rate is present in experimental systems. If it is not, then we have identified an important difference between our idealized systems and real-world microstructures. If it is, then we have identified a powerful tool for predicting microstructural evolution.

9.3 Future work

From the perspective of theoretical development, the most important item of future work is to determine why the morphological differences observed between conditions occur. One possibility, raised in Chapters 4 and 5, is that the kinetics of topological singularities (i.e., the pinching-off of necks) plays a key role in determining morphology. In structures with dissimilar mobilities (Chapter 4), the difference in kinetics between necks containing low- and high-mobility phase is thought to determine their prevalence in the structure. In structures coarsening via surface diffusion (Chapter 5) it is the relative rates of pinching-off of necks and flattening of the resulting caps that is hypothesized to be the difference between surface and bulk diffusion cases. The pinching-

off of necks and flattening of caps are evolution processes that can be modeled analytically. A good first step would be to determine the self-similar shape and dynamics for pinching-off with constant mobility, which would complement existing results for surface diffusion [138, 139] and highly dissimilar mobilities [120, 121]. Examining the effect of a mean field chemical potential on the pinching-off process might also provide insight into coarsening via bulk diffusion at non-$50/50$ volume fractions. This would be especially useful near the limiting volume fraction for bicontinuity (i.e., between $30/70$ and $32/68$), where multiple types of topological singularity are present; pinching-off of necks, disappearance of particles, and coalescence.

The fact that the local geometry is known during topological singularities (at least for pinching-off of necks and disappearance of particles) presents an intriguing opportunity for modeling. Perhaps a model can be created to tie the local evolution of necks and caps to that of the larger structure. This idea originates from particulate models such as LSW theory, which track a single topological feature (a particle) and determine its evolution based on a mean field independently of any other individual particle. Ideally, applying an analogous approach to complex microstructures (e.g., by using the channel size distribution of each phase [182] in place of the particle size distribution) would result in a predictive capability like that of LSW theory. To justify such a model, we need additional information about how topological singularities interact with each other or other features during coarsening. In Chapter 8, we presented an algorithm for detecting topological singularities during a coarsening simulation. While we used this algorithm to prevent topological singularities, it can also be modified to record them. Sites of topological singularities in the simulation could then be examined for correspondence to theory, as in Refs. [120, 121], or aggregated to statistically describe all topological singularities that occur under a given condition. This data could be used to calculate the correlations of different types of topological singularity in space and time. which would inform the assumptions of a coarsening theory based on topological evolution.

It is also important to extend our understanding of coarsening to different materials systems. In this dissertation, a phase field model was determined to be suitable for simulating coarsening with strongly anisotropic interfacial energy via bulk diffusion, and a model for the surface-diffusion case

exists in literature [135, 136, 144]. The space of possible morphologies resulting from anisotropic coarsening is beginning to be mapped [165], but the effect of anisotropy on coarsening dynamics (e.g., pinching-off of necks) has yet to be determined.

Bibliography

[1] W. Ostwald, Über die vermeintliche isomerie des roten und gelben quecksilberoxyds und die oberflächenspannung fester körper, Zeitschrift für physikalische Chemie 34 (1) (1900) 495–503.

[2] S. C. Hardy, P. W. Voorhees, Ostwald ripening in a system with a high volume fraction of coarsening phase, Metallurgical Transactions A 19 (11) (1988) 2713–2721. doi:10.1007/BF02645806.
URL https://doi.org/10.1007/BF02645806

[3] W. D. Callister, Materials Science and Engineering-An Introduction, John Wiley & Sons, 2007.

[4] D. Chang, D. Krueger, R. Sprague, Superalloy powder processing, properties and turbine disk applications, in: Superalloys 1984, Proceedings of the Fifth International Symposium on Superalloys, 1984, pp. 245–273.

[5] A. Baldan, Review Progress in Ostwald ripening theories and their applications to the γ'-precipitates in nickel-base superalloys Part II Nickel-base superalloys, Journal of materials science 37 (12) (2002) 2379–2405.

[6] J. S. Langer, A. J. Schwartz, Kinetics of nucleation in near-critical fluids, Phys. Rev. A 21 (1980) 948–958. doi:10.1103/PhysRevA.21.948.
URL https://link.aps.org/doi/10.1103/PhysRevA.21.948

[7] J. G. Kaufman, E. L. Rooy, Aluminum alloy castings: properties, processes, and applications, ASM International, 2004.

[8] A. Lasalmonie, J. L. Strudel, Influence of grain size on the mechanical behaviour of some high strength materials, Journal of Materials Science 21 (6) (1986) 1837–1852. doi:10.1007/BF00547918.
URL https://doi.org/10.1007/BF00547918

[9] W. R. Osorio, P. R. Goulart, A. Garcia, G. A. Santos, C. M. Neto, Effect of dendritic arm spacing on mechanical properties and corrosion resistance of al 9 wt pct si and zn 27 wt pct al alloys, Metallurgical and Materials Transactions A 37 (8) (2006) 2525–2538. doi:10.1007/BF02586225.
URL https://doi.org/10.1007/BF02586225

[10] Y. Sun, Spatio-temporal analysis of coarsening in complex microstructures using two-point statistics, Ph.D. thesis, Northwestern University (2018).

[11] I. McCue, E. Benn, B. Gaskey, J. Erlebacher, Dealloying and dealloyed materials, Annual review of materials research 46 (2016) 263–286.

[12] K. Sieradzki, R. Newman, Stress-corrosion cracking, Journal of Physics and Chemistry of Solids 48 (11) (1987) 1101 – 1113. doi:https://doi.org/10.1016/0022-3697(87)90120-X.
URL http://www.sciencedirect.com/science/article/pii/002236978790120X

[13] J. Erlebacher, M. J. Aziz, A. Karma, N. Dimitrov, K. Sieradzki, Evolution of nanoporosity in dealloying, Nature 410 (6827) (2001) 450. doi:10.1038/35068529.

[14] Y. Ding, Y.-J. Kim, J. Erlebacher, Nanoporous gold leaf:"ancient technology"/advanced material, Advanced Materials 16 (21) (2004) 1897–1900.

[15] C. Xu, J. Su, X. Xu, P. Liu, H. Zhao, F. Tian, Y. Ding, Low temperature co oxidation over unsupported nanoporous gold, Journal of the American Chemical Society 129 (1) (2007) 42–43. doi:10.1021/ja0675503.

[16] L. H. Qian, M. W. Chen, Ultrafine nanoporous gold by low-temperature dealloying and kinetics of nanopore formation, Applied Physics Letters 91 (8) (2007) 083105. doi:10.1063/1.2773757.
URL https://doi.org/10.1063/1.2773757

[17] X. Lang, A. Hirata, T. Fujita, M. Chen, Nanoporous metal/oxide hybrid electrodes for electrochemical supercapacitors, Nature nanotechnology 6 (4) (2011) 232.

[18] A. Wittstock, V. Zielasek, J. Biener, C. M. Friend, M. Bäumer, Nanoporous gold catalysts for selective gas-phase oxidative coupling of methanol at low temperature, Science 327 (5963) (2010) 319–322. arXiv:http://science.sciencemag.org/content/327/5963/319.full.pdf, doi:10.1126/science.1183591.
URL http://science.sciencemag.org/content/327/5963/319

[19] J. Weissmüller, R. C. Newman, H.-J. Jin, A. M. Hodge, J. W. Kysar, Nanoporous metals by alloy corrosion: Formation and mechanical properties, MRS Bulletin 34 (8) (2009) 577–586. doi:10.1557/mrs2009.157.

[20] K. Hu, M. Ziehmer, K. Wang, E. T. Lilleodden, Nanoporous gold: 3d structural analyses of representative volumes and their implications on scaling relations of mechanical behaviour, Philosophical Magazine 96 (32-34) (2016) 3322–3335.

[21] H. Jeon, N.-R. Kang, E.-J. Gwak, J. il Jang, H. N. Han, J. Y. Hwang, S. Lee, J.-Y. Kim, Self-similarity in the structure of coarsened nanoporous gold, Scripta Materialia 137 (2017) 46 – 49. doi:https://doi.org/10.1016/j.scriptamat.2017.05.009.
URL http://www.sciencedirect.com/science/article/pii/S1359646217302415

[22] Y. chen Karen Chen-Wiegart, S. Wang, Y. S. Chu, W. Liu, I. McNulty, P. W. Voorhees, D. C. Dunand, Structural evolution of nanoporous gold during thermal coarsening, Acta Materialia 60 (12) (2012) 4972 – 4981. doi:https://doi.org/10.1016/j.actamat.2012.05.012.
URL http://www.sciencedirect.com/science/article/pii/S1359645412003229

[23] I. M. Lifshitz, V. V. Slyozov, The kinetics of precipitation from supersaturated solid solutions, Journal of Physics and Chemistry of Solids 19 (1) (1961) 35–50. doi:10.1016/0022-3697(61)90054-3.
URL http://dx.doi.org/10.1016/0022-3697(61)90054-3

[24] C. Wagner, Theory of aging by precipitation coarsening, Z. Elektrochem 65 (1961) 581.

[25] A. D. Brailsford, P. Wynblatt, The dependence of ostwald ripening kinetics on particle volume fraction, Acta Metallurgica 27 (3) (1979) 489–497. doi:10.1016/0001-6160(79)90041-5.

[26] J. A. Marqusee, J. Ross, Kinetics of phase transitions: Theory of ostwald ripening, J. Chem. Phys. 79 (1) (1983) 373. doi:10.1063/1.445532.
URL http://scitation.aip.org/content/aip/journal/jcp/79/1/10.1063/1.445532

[27] P. t. Voorhees, M. Glicksman, Solution to the multi-particle diffusion problem with applications to ostwald ripening—i. theory, Acta metallurgica 32 (11) (1984) 2001–2011.

[28] P. W. Voorhees, The theory of ostwald ripening, Journal of Statistical Physics 38 (1-2) (1985) 231–252. doi:10.1007/BF01017860.
URL http://dx.doi.org/10.1007/BF01017860

[29] P. W. Voorhees, Ostwald ripening of two-phase mixtures, Annual Review of Materials Science 22 (1) (1992) 197–215.

[30] J. H. Yao, K. R. Elder, H. Guo, M. Grant, Theory and simulation of ostwald ripening, Phys. Rev. B 47 (21) (1993) 14110–14125. doi:10.1103/PhysRevB.47.14110.
URL http://link.aps.org/doi/10.1103/PhysRevB.47.14110

[31] L. Ratke, P. W. Voorhees, Growth and coarsening: Ostwald ripening in material processing, Springer-Verlag, 2002.

[32] A. Baldan, Review Progress in Ostwald ripening theories and their applications to nickel-base superalloys Part I: Ostwald ripening theories, Journal of Materials Science 37 (11) (2002) 2171–2202. doi:10.1023/A:1015388912729.
URL https://doi.org/10.1023/A:1015388912729

[33] A. J. Bray, Theory of phase-ordering kinetics, Advances in Physics 51 (2) (2002) 481–587. doi:10.1080/00018730110117433.
URL http://dx.doi.org/10.1080/00018730110117433

[34] A. J. Ardell, R. B. Nicholson, The coarsening of γ' in Ni-Al alloys, Journal of Physics and Chemistry of Solids 27 (11) (1966) 1793–1794. doi:https://doi.org/10.1016/0022-3697(66)90110-7.
URL http://www.sciencedirect.com/science/article/pii/0022369766901107

[35] J. Alkemper, V. Snyder, N. Akaiwa, P. Voorhees, Dynamics of late-stage phase separation: A test of theory, Physical review letters 82 (13) (1999) 2725.

[36] R. Kampmann, R. Wagner, Kinetics of precipitation in metastable binary alloys - theory and application to cu-1.9 at % ti and ni-14 at % al, in: P. Haasen, V. Gerold, R. Wagner, M. Ashby (Eds.), Decomposition of Alloys: the Early Stages, Pergamon, 1984, pp. 91 – 103. doi:https://doi.org/10.1016/B978-0-08-031651-2.50018-5.
URL http://www.sciencedirect.com/science/article/pii/B9780080316512500185

[37] Thermo-Calc Software AB, TC–PRISMA User's Guide and Examples, accessed December 6, 2018.
URL https://www.thermocalc.com/media/6045/tc-prisma_user-guide-and-examples.pdf

[38] Q. Chen, K. Wu, G. Sterner, P. Mason, Modeling precipitation kinetics during heat treatment with calphad-based tools, Journal of Materials Engineering and Performance 23 (12) (2014) 4193–4196. doi:10.1007/s11665-014-1255-6.
URL https://doi.org/10.1007/s11665-014-1255-6

[39] National Research Council, Integrated Computational Materials Engineering: A Transformational Discipline for Improved Competitiveness and National Security, The National Academies Press, Washington, DC, 2008. doi:10.17226/12199.
URL https://www.nap.edu/catalog/12199/integrated-computational-materials-engineerir

[40] S. P. Marsh, M. E. Glicksman, Overview of geometric effects on coarsening of mushy zones, Metallurgical and Materials Transactions A 27 (3) (1996) 557–567. doi:10.1007/BF02648946.
URL http://dx.doi.org/10.1007/BF02648946

[41] R. Mendoza, J. Alkemper, P. W. Voorhees, The morphological evolution of dendritic microstructures during coarsening, Metallurgical and Materials Transactions A 34 (3) (2003) 481–489. doi:10.1007/s11661-003-0084-2.
URL http://dx.doi.org/10.1007/s11661-003-0084-2

[42] R. Mendoza, I. Savin, K. Thornton, P. W. Voorhees, Topological complexity and the dynamics of coarsening, Nature Materials 3 (6) (2004) 385–388. doi:10.1038/nmat1138.
URL http://www.ncbi.nlm.nih.gov/pubmed/15156200

[43] D. Kammer, V. P. W., The morphological evolution of dendritic microstructures during coarsening, Acta Materialia 54 (6) (2006) 1549–1558. doi:10.1016/j.actamat.2005.11.031.

[44] J. L. Fife, P. W. Voorhees, The morphological evolution of equiaxed dendritic microstructures during coarsening, Acta Materialia 57 (8) (2009) 2418–2428. doi:10.1016/j.actamat.2009.01.036.
URL http://dx.doi.org/10.1016/j.actamat.2009.01.036

[45] J. L. Fife, J. W. Gibbs, E. B. Gulsoy, C.-L. Park, K. Thornton, P. W. Voorhees, The dynamics of interfaces during coarsening in solid–liquid systems, Acta Materialia 70 (2014) 66–78. doi:10.1016/j.actamat.2014.01.024.
URL http://dx.doi.org/10.1016/j.actamat.2014.01.024

[46] A. J. Shahani, E. B. Gulsoy, V. J. Roussochatzakis, J. W. Gibbs, J. L. Fife, P. W. Voorhees, The dynamics of coarsening in highly anisotropic systems: Si particles in al–si liquids, Acta Materialia 97 (2015) 325–337. doi:10.1016/j.actamat.2015.06.064.
URL http://dx.doi.org/10.1016/j.actamat.2015.06.064

[47] H. Jinnai, Y. Nishikawa, H. Morimoto, T. Koga, T. Hashimoto, Geometrical properties and interface dynamics: time evolution of spinodal interface in a binary polymer mixture at the critical composition, Langmuir 16 (9) (2000) 4380–4393. doi:10.1021/la991024q.

[48] H. Jinnai, H. Watashiba, T. Kajihara, M. Takahashi, Connectivity and topology of a phase-separating bicontinuous structure in a polymer mixture: Direct measurements of coordination number, inter-junction distances and euler characteristic, The Journal of Chemical Physics 119 (14) (2003) 7554–7559. doi:10.1063/1.1607912.
URL https://doi.org/10.1063/1.1607912

[49] E. Scholten, L. M. Sagis, E. van der Linden, Coarsening rates of bicontinuous structures in polymer mixtures, Macromolecules 38 (8) (2005) 3515–3518.

[50] D. A. Drew, Evolution of geometric statistics, SIAM Journal on Applied Mathematics 50 (3) (1990) 649–666. doi:10.1137/0150038.

[51] C.-L. Park, J. Gibbs, P. Voorhees, K. Thornton, Coarsening of complex microstructures following spinodal decomposition, Acta Materialia 132 (2017) 13 – 24. doi:https://doi.org/10.1016/j.actamat.2017.03.020.
URL http://www.sciencedirect.com/science/article/pii/S1359645417302112

[52] R. T. DeHoff, A geometrically general theory of diffusion controlled coarsening, Acta Metallurgica et Materialia 39 (10) (1991) 2349–2360. doi:10.1016/0956-7151(91)90016-T.
URL http://dx.doi.org/10.1016/0956-7151(91)90016-T

[53] Y. Kwon, K. Thornton, P. W. Voorhees, Coarsening of bicontinuous structures via nonconserved and conserved dynamics, Phys. Rev. E 75 (2007) 021120. doi:10.1103/PhysRevE.75.021120.
URL https://link.aps.org/doi/10.1103/PhysRevE.75.021120

[54] Y. Kwon, K. Thornton, P. W. Voorhees, The topology and morphology of bicontinuous interfaces during coarsening, EPL (Europhysics Letters) 86 (4) (2009) 46005.
URL http://stacks.iop.org/0295-5075/86/i=4/a=46005

[55] Y. Kwon, K. Thornton, P. Voorhees, Morphology and topology in coarsening of domains via non-conserved and conserved dynamics, Philosophical Magazine 90 (1-4) (2010) 317–335. doi:10.1080/14786430903260701.
URL https://doi.org/10.1080/14786430903260701

[56] E. Kreyszig, Differential Geometry, 1991, reprint. Originally published: Toronto, Toronto University Press, 1959.

[57] G. Huisken, Flow by mean curvature of convex surfaces into spheres, J. Differential Geom. 20 (1) (1984) 237–266. doi:10.4310/jdg/1214438998.
URL https://doi.org/10.4310/jdg/1214438998

[58] E. W. Weisstein, Shape operator. From MathWorld—A Wolfram Web Resource, last visited on 01/02/2019.
URL http://mathworld.wolfram.com/ShapeOperator.html

[59] B. J. Spencer, Asymptotic solutions for the equilibrium crystal shape with small corner energy regularization, Phys. Rev. E 69 (2004) 011603. doi:10.1103/PhysRevE.69.011603.
URL https://link.aps.org/doi/10.1103/PhysRevE.69.011603

[60] M. E. Gurtin, J. M. E., Interface Evolution in Three Dimensions with Curvature-Dependent Energy and Surface Diffusion: Interface-Controlled Evolution, Phase Transitions, Epitaxial Growth of Elastic Films, Archive for Rational Mechanics and Analysis 163 (3) (2002) 171–208. doi:10.1007/s002050200193.
URL http://dx.doi.org/10.1007/s002050200193

[61] L. Ratke, P. W. Voorhees, Introduction to Metallurgical Thermodynamics, 2nd Edition, Taylor & Francis, 1981.

[62] L. D. Landau, E. M. Lifshitz, Statistical Physics, 3rd Edition, Elsevier Butterworth-Heinemann, Oxford, 1980.

[63] P. C. Hohenberg, B. I. Halperin, Theory of dynamic critical phenomena, Rev. Mod. Phys. 49 (1977) 435–479. doi:10.1103/RevModPhys.49.435.
URL https://link.aps.org/doi/10.1103/RevModPhys.49.435

[64] J. W. Cahn, J. E. Hilliard, Free energy of a nonuniform system. i. interfacial free energy, The Journal of Chemical Physics 28 (2) (1958) 258–267. doi:10.1063/1.1744102.
URL http://dx.doi.org/10.1063/1.1744102

[65] P. Voorhees, Coarsening in binary solid-liquid mixtures, Metallurgical Transactions A 21 (1) (1990) 27–37.

[66] C. Herring, Surface tension as a motivation for sintering, in: W. E. Kingston (Ed.), The Physics of Powder Metallurgy, McGraw-Hill, New York, 1951, p. 143.

[67] J. W. Gibbs, On the equilibrium of heterogeneous substances, Trans. Conn. Acad. 3 (1878) 343–524.

[68] T. Young, Iii. an essay on the cohesion of fluids, Philosophical transactions of the royal society of London 95 (1805) 65–87.

[69] P. Laplace, Treatise on capillary action, Mechanique Celeste, Supplement to Book 10.

[70] L. D. Landau, E. M. Lifshitz, Fluid Mechanics, 2nd Edition, Elsevier Science & Technology, 1987.

[71] P. Lenz, R. Lipowsky, Stability of droplets and channels on homogeneous and structured surfaces, The European Physical Journal E 1 (2) (2000) 249–262. doi:10.1007/s101890050027.
URL https://doi.org/10.1007/s101890050027

[72] R. Shuttleworth, The surface tension of solids, Proceedings of the Physical Society. Section A 63 (5) (1950) 444.

[73] L. Onsager, Reciprocal relations in irreversible processes. i., Phys. Rev. 37 (1931) 405–426. doi:10.1103/PhysRev.37.405.
URL https://link.aps.org/doi/10.1103/PhysRev.37.405

[74] L. Onsager, Reciprocal relations in irreversible processes. ii., Phys. Rev. 38 (1931) 2265–2279. doi:10.1103/PhysRev.38.2265.
URL https://link.aps.org/doi/10.1103/PhysRev.38.2265

[75] W. W. Mullins, S. R. F., Morphological stability of a particle growing by diffusion or heat flow, Journal of Applied Physics 34 (2) (1963) 323–329. doi:10.1063/1.1702607.

[76] R. L. Pego, Front migration in the nonlinear cahn-hilliard equation, Proceedings of the Royal Society of London A: Mathematical, Physical and Engineering Sciences 422 (1863) (1989) 261–278. doi:10.1098/rspa.1989.0027.

[77] J. K. Wolterink, G. T. Barkema, S. Puri, Spinodal decomposition via surface diffusion in polymer mixtures, Phys. Rev. E 74 (2006) 011804. doi:10.1103/PhysRevE.74.011804.
URL https://link.aps.org/doi/10.1103/PhysRevE.74.011804

[78] J. Erlebacher, Mechanism of coarsening and bubble formation in high-genus nanoporous metals, Phys. Rev. Lett. 106 (2011) 225504. doi:10.1103/PhysRevLett.106.225504.
URL https://link.aps.org/doi/10.1103/PhysRevLett.106.225504

[79] W. W. Mullins, Theory of thermal grooving, Journal of Applied Physics 28 (3) (1957) 333–339. doi:10.1063/1.1722742.
URL https://doi.org/10.1063/1.1722742

[80] C. Herring, Effect of change of scale on sintering phenomena, Journal of Applied Physics 21 (4) (1950) 301–303. doi:10.1063/1.1699658.
URL https://doi.org/10.1063/1.1699658

[81] S. Dai, Q. Du, Motion of interfaces governed by the cahn–hilliard equation with highly disparate diffusion mobility, SIAM Journal on Applied Mathematics 72 (6) (2012) 1818–1841. doi:10.1137/120862582.
URL http://dx.doi.org/10.1137/120862582

[82] R. V. Kohn, F. Otto, Upper bounds on coarsening rates, Communications in Mathematical Physics 229 (3) (2002) 375–395. doi:10.1007/s00220-002-0693-4.
URL https://doi.org/10.1007/s00220-002-0693-4

[83] W. W. Mullins, Flattening of a nearly plane solid surface due to capillarity, Journal of Applied Physics 30 (1) (1959) 77–83. doi:10.1063/1.1734979.
URL https://doi.org/10.1063/1.1734979

[84] T. Z. Kattamis, Influence of coarsening on dendrite arm spacing of aluminum-copper alloys, Transaction of the Metallurgical Society of AIME 239 (1967) 1504–1511.

[85] N. Limodin, L. Salvo, E. Boller, M. Suéry, M. Felberbaum, S. Gaillièguе, K. Madi, In situ and real-time 3-d microtomography investigation of dendritic solidification in an al–10 wt.% cu alloy, Acta Materialia 57 (7) (2009) 2300–2310.

[86] L.-Q. Chen, Phase-field models for microstructure evolution, Annual Review of Materials Research 32 (1) (2002) 113–140. doi:10.1146/annurev.matsci.32.112001.132041.
URL https://doi.org/10.1146/annurev.matsci.32.112001.132041

[87] H. Emmerich, Advances of and by phase-field modelling in condensed-matter physics, Advances in Physics 57 (1) (2008) 1–87. doi:10.1080/00018730701822522.
URL https://doi.org/10.1080/00018730701822522

[88] N. Provatas, K. Elder, Phase-field methods in materials science and engineering, John Wiley & Sons, 2011.

[89] J. D. van der Waals, The thermodynamic theory of capillarity under the hypothesis of a continuous variation of density, Journal of Statistical Physics 20 (2) (1979) 200–244. doi:10.1007/BF01011514.
URL https://doi.org/10.1007/BF01011514

[90] J. S. Rowlinson, Translation of j. d. van der waals' "the thermodynamik theory of capillarity under the hypothesis of a continuous variation of density", Journal of Statistical Physics 20 (2) (1979) 197–200. doi:10.1007/BF01011513.
URL https://doi.org/10.1007/BF01011513

[91] J. Langer, Theory of spinodal decomposition in alloys, Annals of Physics 65 (1) (1971) 53 – 86. doi:https://doi.org/10.1016/0003-4916(71)90162-X.
URL http://www.sciencedirect.com/science/article/pii/000349167190162X

[92] J. S. Langer, M. Bar-on, H. D. Miller, New computational method in the theory of spinodal decomposition, Phys. Rev. A 11 (1975) 1417–1429. doi:10.1103/PhysRevA.11.1417.
URL https://link.aps.org/doi/10.1103/PhysRevA.11.1417

[93] J. W. Cahn, On spinodal decomposition, Acta Metallurgica 9 (9) (1961) 795–801. doi:http://dx.doi.org/10.1016/0001-6160(61)90182-1.
URL http://www.sciencedirect.com/science/article/pii/0001616061901821

[94] T. M. Rogers, K. R. Elder, R. C. Desai, Numerical study of the late stages of spinodal decomposition, Phys. Rev. B 37 (16) (1988) 9638–9649. doi:10.1103/PhysRevB.37.9638.
URL http://link.aps.org/doi/10.1103/PhysRevB.37.9638

[95] T. M. Rogers, R. C. Desai, Numerical study of late-stage coarsening for off-critical quenches in the cahn-hilliard equation of phase separation, Physical Review B 39 (16) (1989) 11956–11964. doi:10.1103/PhysRevB.39.11956.

[96] G. Caginalp, The dynamics of a conserved phase field system: Stefan-like, hele-shaw, and cahn-hilliard models as asymptotic limits, IMA Journal of Applied Mathematics 44 (1) (1990) 77–94. doi:10.1093/imamat/44.1.77.
URL http://dx.doi.org/10.1093/imamat/44.1.77

[97] K. Kitahara, M. Imada, On the kinetic equations for binary mixtures, Progress of Theoretical Physics Supplement 64 (1978) 65–73. doi:10.1143/PTPS.64.65.
URL http://dx.doi.org/10.1143/PTPS.64.65

[98] R. J. LeVeque, Finite difference methods for ordinary and partial differential equations: steady-state and time-dependent problems, Vol. 98, Siam, 2007.

[99] D. Sappelt, J. Jäckle, Computer simulation study of phase separation in a binary mixture with a glass-forming component, Physica A: Statistical Mechanics and its Applications 240 (3-4) (1997) 453–479. doi:10.1016/S0378-4371(97)00048-4.
URL http://www.sciencedirect.com/science/article/pii/S0378437197000484

[100] S. Dai, Q. Du, Computational studies of coarsening rates for the cahn–hilliard equation with phase-dependent diffusion mobility, Journal of Computational Physics 310 (2016) 85 – 108. doi:https://doi.org/10.1016/j.jcp.2016.01.018.
URL http://www.sciencedirect.com/science/article/pii/S002199911600019X

[101] C.-L. Park, P. W. Voorhees, K. Thornton, Application of the level-set method to the analysis of an evolving microstructure, Computational Materials Science 85 (2014) 46–58. doi:10.1016/j.commatsci.2013.12.022.
URL http://dx.doi.org/10.1016/j.commatsci.2013.12.022

[102] E. W. Weisstein, Genus. From MathWorld—A Wolfram Web Resource, last visited on 01/02/2019.
URL http://mathworld.wolfram.com/Genus.html

[103] A. Odgaard, H. Gundersen, Quantification of connectivity in cancellous bone, with special emphasis on 3-d reconstructions, Bone 14 (2) (1993) 173 – 182. doi:https://doi.org/10.1016/8756-3282(93)90245-6.
URL http://www.sciencedirect.com/science/article/pii/8756328293902456

[104] E. W. Weisstein, Euler characteristic. From MathWorld—A Wolfram Web Resource, last visited on 11/21/2018.
URL http://mathworld.wolfram.com/EulerCharacteristic.html

[105] A. M. Lacasta, A. Hernández-Machado, J. M. Sancho, R. Toral, Domain growth in binary mixtures at low temperatures, Phys. Rev. B 45 (1992) 5276–5281. doi:10.1103/PhysRevB.45.5276.
URL https://link.aps.org/doi/10.1103/PhysRevB.45.5276

[106] J. Zhu, L.-Q. Chen, J. Shen, V. Tikare, Coarsening kinetics from a variable-mobility cahn-hilliard equation: Application of a semi-implicit fourier spectral method, Phys. Rev. E 60 (1999) 3564–3572. doi:10.1103/PhysRevE.60.3564.
URL https://link.aps.org/doi/10.1103/PhysRevE.60.3564

[107] D. Sappelt, J. Jäckle, Spinodal decomposition with formation of a glassy phase, Europhysics Letters (EPL) 37 (1997) 13–18. doi:10.1209/epl/i1997-00110-7.
URL http://iopscience.iop.org/0295-5075/37/1/013

[108] R. Ahluwalia, Phase separation in a simple model with dynamical asymmetry, Phys. Rev. E 59 (1999) 263–268. doi:10.1103/PhysRevE.59.263.
URL https://link.aps.org/doi/10.1103/PhysRevE.59.263

[109] G. Sheng, T. Wang, Q. Du, K. G. Wang, Z. K. Liu, L. Q. Chen, Coarsening kinetics of a two phase mixture with highly disparate diffusion mobility, Communications in Computational Physics 8 (2) (2010) 249–264. doi:10.4208/cicp.160709.041109a.

[110] L. Ju, J. Zhang, Q. Du, Fast and accurate algorithms for simulating coarsening dynamics of cahn–hilliard equations, Computational Materials Science 108 (2015) 272 – 282, selected Articles from Phase-field Method 2014 International Seminar. doi:https://doi.org/10.1016/j.commatsci.2015.04.046.
URL http://www.sciencedirect.com/science/article/pii/S092702561500292X

[111] J. Zhang, C. Zhou, Y. Wang, L. Ju, Q. Du, X. Chi, D. Xu, D. Chen, Y. Liu, Z. Liu, Extreme-scale phase field simulations of coarsening dynamics on the sunway taihulight supercomputer, in: Proceedings of the International Conference for High Performance Computing, Networking, Storage and Analysis, SC '16, IEEE Press, Piscataway, NJ, USA, 2016, pp. 4:1–4:12.
URL http://dl.acm.org/citation.cfm?id=3014904.3014910

[112] H. Jinnai, Y. Nishikawa, R. J. Spontak, S. D. Smith, D. A. Agard, T. Hashimoto, Direct measurement of interfacial curvature distributions in a bicontinuous block copolymer morphology, Phys. Rev. Lett. 84 (2000) 518–521. doi:10.1103/PhysRevLett.84.518.
URL https://link.aps.org/doi/10.1103/PhysRevLett.84.518

[113] J. A. Warren, W. J. Boettinger, Prediction of dendritic growth and microsegregation patterns in a binary alloy using the phase-field method, Acta Metallurgica et Materialia 43 (2) (1995) 689 – 703. doi:https://doi.org/10.1016/0956-7151(94)00285-P.
URL http://www.sciencedirect.com/science/article/pii/095671519400285P

[114] A. Karma, Phase-field formulation for quantitative modeling of alloy solidification, Phys. Rev. Lett. 87 (2001) 115701. doi:10.1103/PhysRevLett.87.115701.
URL https://link.aps.org/doi/10.1103/PhysRevLett.87.115701

[115] A. J. Bray, C. L. Emmott, Lifshitz-slyozov scaling for late-stage coarsening with an order-parameter-dependent mobility, Physical Review B 52 (2) (1995) 685–688. doi:10.1103/PhysRevB.52.R685.

[116] S. Dai, Q. Du, Coarsening mechanism for systems governed by the cahn–hilliard equation with degenerate diffusion mobility, Multiscale Modeling & Simulation 12 (4) (2014) 1870–1889. doi:10.1137/140952387.
URL https://doi.org/10.1137/140952387

[117] A. A. Lee, A. Münch, E. Süli, Degenerate mobilities in phase field models are insufficient to capture surface diffusion, Applied Physics Letters 107 (8) (2015) 081603. doi:10.1063/1.4929696.
URL https://doi.org/10.1063/1.4929696

[118] A. Lee, A. Münch, E. Süli, Sharp-interface limits of the cahn–hilliard equation with degenerate mobility, SIAM Journal on Applied Mathematics 76 (2) (2016) 433–456. doi:10.1137/140960189.
URL https://doi.org/10.1137/140960189

[119] H. Garcke, B. Niethammer, M. Rumpf, U. Weikard, Transient coarsening behaviour in the cahn–hilliard model, Acta Materialia 51 (10) (2003) 2823–2830. doi:https://doi.org/10.1016/S1359-6454(03)00087-9.
URL http://www.sciencedirect.com/science/article/pii/S1359645403000879

[120] L. K. Aagesen, A. E. Johnson, J. L. Fife, P. W. Voorhees, M. J. Miksis, S. O. Poulsen, E. M. Lauridsen, F. Marone, M. Stampanoni, Universality and self-similarity in pinch-off of rods by bulk diffusion, Nature Physics 6 (10) (2010) 796. doi:10.1038/nphys1737.
URL https://doi.org/10.1023/B:JOSS.0000033251.81126.af

[121] L. Aagesen, A. Johnson, J. Fife, P. Voorhees, M. Miksis, S. Poulsen, E. Lauridsen, F. Marone, M. Stampanoni, Pinch-off of rods by bulk diffusion, Acta Materialia 59 (12) (2011) 4922 – 4932. doi:https://doi.org/10.1016/j.actamat.2011.04.036.
URL http://www.sciencedirect.com/science/article/pii/S1359645411002783

[122] R. Li, K. Sieradzki, Ductile-brittle transition in random porous au, Physical Review Letters 68 (8) (1992) 1168.

[123] K. Mangipudi, E. Epler, C. Volkert, Topology-dependent scaling laws for the stiffness and strength of nanoporous gold, Acta Materialia 119 (2016) 115–122.

[124] J. Biener, A. Wittstock, L. Zepeda-Ruiz, M. Biener, V. Zielasek, D. Kramer, R. Viswanath, J. Weissmüller, M. Bäumer, A. Hamza, Surface-chemistry-driven actuation in nanoporous gold, Nature materials 8 (1) (2009) 47.

[125] L. Sun, C.-L. Chien, P. C. Searson, Fabrication of nanoporous nickel by electrochemical dealloying, Chemistry of materials 16 (16) (2004) 3125–3129.

[126] J. Thorp, K. Sieradzki, L. Tang, P. Crozier, A. Misra, M. Nastasi, D. Mitlin, S. Picraux, Formation of nanoporous noble metal thin films by electrochemical dealloying of Pt_xSi_{1-x}, Applied Physics Letters 88 (3) (2006) 033110.

[127] Q. Zhang, Z. Zhang, On the electrochemical dealloying of Al-based alloys in a NaCl aqueous solution, Physical Chemistry Chemical Physics 12 (7) (2010) 1453–1472.

[128] M. Ziehmer, K. Hu, K. Wang, E. T. Lilleodden, A principle curvatures analysis of the isothermal evolution of nanoporous gold: Quantifying the characteristic length-scales, Acta Materialia 120 (2016) 24–31.

[129] S. Puri, A. J. Bray, J. L. Lebowitz, Phase-separation kinetics in a model with order-parameter-dependent mobility, Phys. Rev. E 56 (1997) 758–765. doi:10.1103/PhysRevE.56.758.
URL https://link.aps.org/doi/10.1103/PhysRevE.56.758

[130] S. van Gemmert, G. T. Barkema, S. Puri, Phase separation driven by surface diffusion: A monte carlo study, Phys. Rev. E 72 (2005) 046131. doi:10.1103/PhysRevE.72.046131.
URL https://link.aps.org/doi/10.1103/PhysRevE.72.046131

[131] J. Cahn, J. Taylor, Overview no. 113 surface motion by surface diffusion, Acta Metallurgica et Materialia 42 (4) (1994) 1045 – 1063. doi:https://doi.org/10.1016/0956-7151(94)90123-6.
URL http://www.sciencedirect.com/science/article/pii/0956715194901236

[132] J. W. Cahn, C. M. Elliott, A. Novick-Cohen, The cahn–hilliard equation with a concentration dependent mobility: motion by minus the laplacian of the mean curvature, European Journal of Applied Mathematics 7 (3) (1996) 287–301. doi:10.1017/S0956792500002369.

[133] C. Elliott, H. Garcke, On the cahn–hilliard equation with degenerate mobility, SIAM Journal on Mathematical Analysis 27 (2) (1996) 404–423. doi:10.1137/S0036141094267662.
URL https://doi.org/10.1137/S0036141094267662

[134] S. Wise, J. Kim, J. Lowengrub, Solving the regularized, strongly anisotropic cahn-hilliard equation by an adaptive nonlinear multigrid method, Journal of Computational Physics 226 (1) (2007) 414–446. doi:10.1016/j.jcp.2007.04.020.

[135] S. Torabi, J. Lowengrub, A. Voigt, S. Wise, A new phase-field model for strongly anisotropic systems, Proceedings of the Royal Society of London A: Mathematical, Physical and Engineering Sciencesdoi:10.1098/rspa.2008.0385.
URL http://rspa.royalsocietypublishing.org/content/early/2009/02/08/rspa.2008.0385

[136] A. Rätz, R. Angel, V. Axel, Surface evolution of elastically stressed films under deposition by a diffuse interface model, Journal of Computational Physics 214 (1) (2006) 187–208. doi:10.1016/j.jcp.2005.09.013.
URL http://dx.doi.org/10.1016/j.jcp.2005.09.013

[137] C. Gugenberger, R. Spatschek, K. Kassner, Comparison of phase-field models for surface diffusion, Phys. Rev. E 78 (2008) 016703. doi:10.1103/PhysRevE.78.016703.
URL https://link.aps.org/doi/10.1103/PhysRevE.78.016703

[138] M. S. McCallum, P. W. Voorhees, M. J. Miksis, S. H. Davis, H. Wong, Capillary instabilities in solid thin films: Lines, Journal of Applied Physics 79 (10) (1996) 7604–7611. doi:10.1063/1.362343.
URL https://doi.org/10.1063/1.362343

[139] A. J. Bernoff, A. L. Bertozzi, T. P. Witelski, Axisymmetric surface diffusion: Dynamics and stability of self-similar pinchoff, Journal of Statistical Physics 93 (3) (1998) 725–776. doi:10.1023/B:JOSS.0000033251.81126.af.
URL https://doi.org/10.1023/B:JOSS.0000033251.81126.af

[140] R. Kobayashi, Modeling and numerical simulations of dendritic crystal growth, Physica D: Nonlinear Phenomena 63 (3) (1993) 410 – 423. doi:https://doi.org/10.1016/0167-2789(93)90120-P.
URL http://www.sciencedirect.com/science/article/pii/016727899390120P

[141] G. B. McFadden, A. A. Wheeler, R. J. Braun, S. R. Coriell, R. F. Sekerka, Phase-field models for anisotropic interfaces, Phys. Rev. E 48 (1993) 2016–2024. doi:10.1103/PhysRevE.48.2016.
URL https://link.aps.org/doi/10.1103/PhysRevE.48.2016

[142] J. Eggleston, G. McFadden, P. Voorhees, A phase-field model for highly anisotropic interfacial energy, Physica D: Nonlinear Phenomena 150 (1) (2001) 91 – 103. doi:https://doi.org/10.1016/S0167-2789(00)00222-0.
URL http://www.sciencedirect.com/science/article/pii/S0167278900002220

[143] S. M. Wise, J. S. Lowengrub, J. S. Kim, K. Thornton, P. W. Voorhees, W. C. Johnson, Quantum dot formation on a strain-patterned epitaxial thin film, Applied Physics Letters 87 (13) (2005) 133102. doi:10.1063/1.2061852.
URL https://doi.org/10.1063/1.2061852

[144] M. Salvalaglio, R. Backofen, R. Bergamaschini, F. Montalenti, A. Voigt, Faceting of equilibrium and metastable nanostructures: A phase-field model of surface diffusion tackling realistic shapes, Crystal Growth & Design 15 (6) (2015) 2787–2794. doi:10.1021/acs.cgd.5b00165.
URL https://doi.org/10.1021/acs.cgd.5b00165

[145] F. Abdeljawad, D. L. Medlin, J. A. Zimmerman, K. Hattar, S. M. Foiles, A diffuse interface model of grain boundary faceting, Journal of Applied Physics 119 (23) (2016) 235306. doi:10.1063/1.4954066.
URL https://doi.org/10.1063/1.4954066

[146] G. Wulff, Xxv. zur frage der geschwindigkeit des wachsthums und der auflösung der krystallflächen, Zeitschrift für Kristallographie-Crystalline Materials 34 (1-6) (1901) 449–530.

[147] A. Wheeler, Phase-field theory of edges in an anisotropic crystal, Proceedings of the Royal Society of London A: Mathematical, Physical and Engineering Sciences 462 (2075) (2006) 3363–3384. doi:10.1098/rspa.2006.1721.
URL http://rspa.royalsocietypublishing.org/content/462/2075/3363

[148] C. Herring, Some Theorems on the Free Energies of Crystal Surfaces, Phys. Rev. 82 (1951) 87–93. doi:10.1103/PhysRev.82.87.
URL https://link.aps.org/doi/10.1103/PhysRev.82.87

[149] S. Angenent, M. E. Gurtin, Multiphase thermomechanics with interfacial structure 2. evolution of an isothermal interface, Archive for Rational Mechanics and Analysis 108 (3) (1989) 323–391.

[150] J. E. Taylor, J. W. Cahn, Diffuse interfaces with sharp corners and facets: Phase field models with strongly anisotropic surfaces, Physica D: Nonlinear Phenomena 112 (3) (1998) 381 – 411. doi:https://doi.org/10.1016/S0167-2789(97)00177-2.
URL http://www.sciencedirect.com/science/article/pii/S0167278997001772

[151] N. Cabrera, The equilibrium of crystal surfaces, Surface Science 2 (1964) 320 – 345. doi:https://doi.org/10.1016/0039-6028(64)90073-1.
URL http://www.sciencedirect.com/science/article/pii/0039602864900731

[152] N. Gjostein, Adsorption and surface energy (ii): Thermal faceting from minimization of surface energy, Acta Metallurgica 11 (8) (1963) 969 – 978. doi:https://doi.org/10.1016/0001-6160(63)90066-X.
URL http://www.sciencedirect.com/science/article/pii/000161606390066X

[153] Y. Kim, M. H. Jo, T. C. Kim, C. W. Yang, J. W. Kim, J. S. Hwang, D. Y. Noh, N. D. Kim, J. W. Chung, Coarsening Kinetics of a Spinodally Decomposed Vicinal Si(111) Surface, Phys. Rev. Lett. 102 (2009) 156103. doi:10.1103/PhysRevLett.102.156103.
URL https://link.aps.org/doi/10.1103/PhysRevLett.102.156103

[154] J. Stewart, N. Goldenfeld, Spinodal decomposition of a crystal surface, Physical Review A 46 (10) (1992) 6505.

[155] F. Liu, H. Metiu, Dynamics of phase separation of crystal surfaces, Physical Review B 48 (9) (1993) 5808.

[156] A. Di Carlo, M. E. Gurtin, P. Podio-Guidugli, A regularized equation for anisotropic motion-by-curvature, SIAM Journal on Applied Mathematics 52 (4) (1992) 1111–1119.

[157] M. A. Pinsky, Partial differential equations and boundary-value problems with applications, Vol. 15, American Mathematical Soc., 2011.

[158] D. Alpay, L. Peng, L. D. Marks, Are Nanoparticle Corners Round?, The Journal of Physical Chemistry C 119 (36) (2015) 21018–21023. doi:10.1021/acs.jpcc.5b07021.
URL https://doi.org/10.1021/acs.jpcc.5b07021

[159] D. W. Hoffman, J. W. Cahn, A vector thermodynamics for anisotropic surfaces: I. Fundamentals and application to plane surface junctions, Surface Science 31 (1972) 368 – 388. doi:https://doi.org/10.1016/0039-6028(72)90268-3.
URL http://www.sciencedirect.com/science/article/pii/0039602872902683

[160] J. Cahn, D. Hoffman, A vector thermodynamics for anisotropic surfaces—II. Curved and faceted surfaces, Acta Metallurgica 22 (10) (1974) 1205 – 1214. doi:https://doi.org/10.1016/0001-6160(74)90134-5.
URL http://www.sciencedirect.com/science/article/pii/0001616074901345

[161] R. F. Sekerka, Analytical criteria for missing orientations on three-dimensional equilibrium shapes, Journal of Crystal Growth 275 (1) (2005) 77 – 82, proceedings of the 14th International Conference on Crystal Growth and the 12th International Conference on Vapor Growth and Epitaxy. doi:https://doi.org/10.1016/j.jcrysgro.2004.10.069.
URL http://www.sciencedirect.com/science/article/pii/S0022024804013843

[162] T. A. Abinandanan, F. Haider, An extended Cahn-Hilliard model for interfaces with cubic anisotropy, Philosophical Magazine A 81 (10) (2001) 2457–2479. doi:10.1080/01418610110038420.
URL https://doi.org/10.1080/01418610110038420

[163] E. Nani, M. Gururajan, On the incorporation of cubic and hexagonal interfacial energy anisotropy in phase field models using higher order tensor terms, Philosophical Magazine 94 (29) (2014) 3331–3352.

[164] G. Caginalp, P. Fife, Higher-order phase field models and detailed anisotropy, Physical review B 34 (7) (1986) 4940.

[165] A. Vidyasagar, S. Krödel, D. M. Kochmann, Microstructural patterns with tunable mechanical anisotropy obtained by simulating anisotropic spinodal decomposition, Proceedings of the Royal Society A: Mathematical, Physical and Engineering Sciences 474 (2218) (2018) 20180535. arXiv:https://royalsocietypublishing.org/doi/pdf/10.1098/rspa.2018.0535, doi:10.1098/rspa.2018.0535.
URL https://royalsocietypublishing.org/doi/abs/10.1098/rspa.2018.0535

[166] J. W. Barrett, H. Garcke, R. Nürnberg, On stable parametric finite element methods for the Stefan problem and the Mullins–Sekerka problem with applications to dendritic growth, Journal of Computational Physics 229 (18) (2010) 6270 – 6299. doi:https://doi.org/10.1016/j.jcp.2010.04.039.
URL http://www.sciencedirect.com/science/article/pii/S0021999110002263

[167] E. De Giorgi, Some remarks on Γ-convergence and least squares method, in: Composite media and homogenization theory, Springer, 1991, pp. 135–142.

[168] S. Torabi, J. Lowengrub, Simulating interfacial anisotropy in thin-film growth using an extended Cahn-Hilliard model, Phys. Rev. E 85 (2012) 041603. doi:10.1103/PhysRevE.85.041603.
URL https://link.aps.org/doi/10.1103/PhysRevE.85.041603

[169] J. Mathews, R. L. Walker, Mathematical methods of physics, Vol. 501, WA Benjamin New York, 1970.

[170] G. Caginalp, An analysis of a phase field model of a free boundary, Archive for Rational Mechanics and Analysis 92 (3) (1986) 205–245.

[171] G. Caginalp, W. Xie, Phase-field and sharp-interface alloy models, Physical Review E 48 (3) (1993) 1897.

[172] P. C. Fife, Dynamics of internal layers and diffusive interfaces, Vol. 53, SIAM, 1988.

[173] R. F. Almgren, Second-order phase field asymptotics for unequal conductivities, SIAM Journal on Applied Mathematics 59 (6) (1999) 2086–2107.

[174] C. M. Bender, S. A. Orszag, Advanced mathematical methods for scientists and engineers I: Asymptotic methods and perturbation theory, Springer Science & Business Media, 2013.

[175] A. A. Wheeler, G. B. McFadden, A ξ-vector formulation of anisotropic phase-field models: 3d asymptotics, European Journal of Applied Mathematics 7 (4) (1996) 367–381. doi:10.1017/S0956792500002424.

[176] A. A. Wheeler, G. B. McFadden, On the notion of a ξ–vector and a stress tensor for a general class of anisotropic diffuse interface models, Proceedings of the Royal Society of London A: Mathematical, Physical and Engineering Sciences 453 (1963) (1997) 1611–1630. doi:10.1098/rspa.1997.0086.
URL http://rspa.royalsocietypublishing.org/content/453/1963/1611

[177] J. Rubinstein, P. Sternberg, J. B. Keller, Fast reaction, slow diffusion, and curve shortening, SIAM Journal on Applied Mathematics 49 (1) (1989) 116–133.

[178] A. Kumar, Isotropic finite-differences, Journal of Computational Physics 201 (1) (2004) 109 – 118. doi:https://doi.org/10.1016/j.jcp.2004.05.005.
URL http://www.sciencedirect.com/science/article/pii/S0021999104002037

[179] S. M. Allen, J. W. Cahn, A microscopic theory for antiphase boundary motion and its application to antiphase domain coarsening, Acta Metallurgica 27 (6) (1979) 1085 – 1095. doi:https://doi.org/10.1016/0001-6160(79)90196-2.
URL http://www.sciencedirect.com/science/article/pii/0001616079901962

[180] P. W. Dondl, A. Lemenant, S. Wojtowytsch, Phase field models for thin elastic structures with topological constraint, Archive for Rational Mechanics and Analysis 223 (2) (2017) 693–736. doi:10.1007/s00205-016-1043-6.
URL https://doi.org/10.1007/s00205-016-1043-6

[181] S. Wojtowytsch, Phase-field models and connectedness [abstract], in: Proceedings of the 2018 SIAM Conference on Mathematical Aspects of Materials Science , 2018, p. 227.

[182] V. Chan, K. Thornton, Channel size distribution of complex three-dimensional microstructures calculated from the topological characterization of isodistance structures, Acta Materialia 60 (6) (2012) 2509 – 2517. doi:https://doi.org/10.1016/j.actamat.2011.12.042.
URL http://www.sciencedirect.com/science/article/pii/S1359645411009049